UNIVERSITÄT AUGSBURG
Experimentalphysik I

Gallium nitride based thin films for photon and particle radiation dosimetry

Dissertation zur Erlangung des Doktorgrades Dr. rer. nat.
der Mathematisch-Naturwissenschaftlichen Fakultät
der Universität Augsburg
im Jahr 2012 von

Markus Hofstetter

HelmholtzZentrum münchen
Deutsches Forschungszentrum für Gesundheit und Umwelt

1. Korrektor: PD Dr. Stefan Thalhammer

2. Korrektor: Prof. Dr. Wolfgang Brütting

Tag der mündlichen Prüfung: 23.07.2012

Zusammenfassung

Ionisationskammern zur Messung ionisierender Strahlung werden bereits seit Beginn des 20.ten Jahrhunderts verwendet und stellen immer noch den „Gold-Standard“ in der Dosimetrie dar. Da die Empfindlichkeit allerding proportional zum Detektionsvolumen ist, finden Ionisationskammern nahezu keine Anwendung in der medizinischen Bildgebung. Dort werden ortsaufgelöste Dosisinformationen, neben Filmsystemen, in der Regel mit Szintillationskristallen und Photomultipliern erfasst, was aber wiederum ein recht aufwendiges und komplexes Verfahren darstellt. Aus diesem Grund wurde in den letzten Jahren viel Aufwand in die Erforschung neuartiger Detektionssysteme gesteckt. Beispiele hierfür wären Germanium- oder Silizium-Halbleiterdetektoren, MOSFET-Detektoren oder PIN-Dioden. Obwohl diese Techniken eine Miniaturisierung und somit eine ortsaufgelöste Detektion ermöglichen, verhindern Nachteile wie beispielsweise eine begrenzte Messstabilität, Materialdegradation oder ein eingeschränkter Messbereich einen routinemäßig verbreiteten Einsatz. In dieser Arbeit werden dünne Galliumnitrid (GaN) Schichten sowie Heterostrukturen basierend auf Galliumnitrid bezüglich der Detektion von Röntgenstrahlung im medizinisch relevanten Bereich untersucht. Weiterhin werden der Einfluss von Partikelstrahlung und die daraus resultierenden Effekte erforscht. Obwohl frühere Publikationen bereits zeigten, dass die Energieabsorption von Röntgenstrahlung in Galliumnitrid relativ gering ist, ist es möglich, durch eine geeignete Sensorkonfiguration sehr hohe Verstärkungsfaktoren im Material zu verwirklichen und somit die geringe Absorption zu kompensieren. Dabei wird das Galliumnitrid als Photoleiter mit ohmschen Kontakten eingesetzt. Unter Röntgenstrahlung ändert sich das leitfähige Volumen des Detektorelements, was durch Anlegen einer Vorspannung zu einem verstärkten Messsignal führt. Experimente haben gezeigt, dass sich in einem Dosisratenbereich zwischen 1 µGy/s und 20 mGy/s eine deutliche Änderung des Messsignals ergibt, das wiederum mit der Dosisrate abgeglichen werden kann. Dabei wurden die Sensoren in einem Energiebereich von 10 – 200 keV getestet. Obwohl das Messvolumen der GaN-Sensoren etwa um den Faktor 10^5 kleiner ist als das von Ionisationskammern, konnten teilweise vergleichbare Messergebnisse erzielt werden. Durch das Ausnutzen eines zweidimensionalen Elektronengases einer AlGaN/GaN Heterostruktur, konnten noch höhere Verstärkungsfaktoren der Sensoren erzielt werden, was eine Messung von Photonenflüssen im Bereich von > 10^3 Teilchen/s ermöglicht. Da diese Heterostrukturen auch für Messungen physiologischer Parameter wie beispielsweise den pH-Wert eingesetzt werden, wurde weiterhin die Kombination von Oberflächenpotentialmessungen mit der Röntgendosimetrie untersucht. Es konnte gezeigt werden, dass nicht nur die Messung von physiologischen Größen während Bestrahlungsexperimenten möglich ist, sondern sogar kombinierte Messungen von pH und Strahlung realisierbar sind, wobei die Oberflächensensitivität von 57 mV/pH erhalten bleibt. Untersuchungen bezüglich der Biokompatibilität und Biofunktionalität von Galliumnitrid haben gezeigt, dass keine messbaren Veränderungen in zellulären Systemen auftreten, die durch das Material verursacht werden. Zusammenfassend wird in dieser Arbeit gezeigt, dass Detektoren basierend auf Galliumnitrid ein neuartiges System zur Strahlendetektion darstellt, das Eigenschaften besitzt, womit eventuell Probleme bisheriger Technologien überwunden werden können. Weiterhin lassen sich mit einer GaN-Heterostruktur Biosensoren verwirklichen, die unter Röntgenstrahlung arbeiten und Messungen mehrerer Parameter ermöglichen.

Abstract

Ionization chambers have been used since the beginning of the 20th century for measuring ionizing radiation and still represent the “gold standard” in dosimetry. However, since the sensitivity of the devices is proportional to the detection volume, ionization chambers are not common in numerous medical applications, such as imaging. In these fields, spatially resolved dose information is, beside film-systems, usually measured with scintillators and photo-multipliers, which is a relatively complex and expensive technique. For thus much effort has been focused on the development of novel detection systems in the last decades and especially in the last few years. Examples include germanium or silicon photoconductive detectors, MOSFETs, and PIN-diodes. Although for these systems, miniaturization for spatially resolved detection is possible, they suffer from a range of disadvantages. Characteristics such as poor measurement stability, material degradation, and/or a limited measurement range prevent routine application of these techniques in medical diagnostic devices. This work presents the development and evaluation of gallium nitride (GaN) thin films and heterostructures to validate their application in x-ray detection in the medical regime. Furthermore, the impact of particle radiation on device response was investigated. Although previous publications revealed relatively low energy absorption of GaN, it is possible to achieve very high signal amplification factors inside the material due to an appropriate sensor configuration, which, in turn, compensates the low energy absorption. Thus, gallium nitride can be used as a photo-conductor with ohmic contacts. The conductive volume of the sensor changes in the presence of external radiation, which results in an amplified measurement signal after applying a bias voltage to the device. Experiments revealed a sensitivity of the device between air kerma rates of 1 µGy/s and 20 mGy/s. In this range, the measured signals can be calibrated against the corresponding dose rate. The sensors were tested in an x-ray energy regime of 10 – 200 keV. Although the active sensor volume of the GaN devices is about 10^5 times smaller than ionization chambers, it was possible to produce partially comparable measurement results. By utilizing a two-dimensional electron gas, which is produced inside an AlGaN/GaN heterostructure, a further increase of the amplification factors of the devices was achievable. Therefore, measurement of photon intensities in the range of > 10^3 photons/s is possible. Since these structures are also used for the measurement of physiological parameters like the pH value, combined measurements of surface potentials and x-ray dosimetry were investigated. It could be shown that not only a measurement of physiological parameters during an irradiation is possible but also combined simultaneous measurements of radiation and the surface pH, while keeping a sensitivity of 57 mV/pH. Therefore the GaN sensors could be used as biosensing tools in radiation biophysics, in addition to their application as pure dosimeters. Biocompatibility and biofunctionality evaluations of gallium nitride show that no alterations of cellular systems in direct contact with the material are measureable. In summary, this work demonstrates a novel system for radiation detection based on gallium nitride, which possesses characteristics that could overcome difficulties of other technologies, such as these mentioned above. Furthermore, by utilizing a heterostructure, the devices could be used as biosensors, which work during external radiation exposure and allow multi-parameter measurements.

Contents

1 Introduction

1.1 Radiation

In 1895, Wilhelm Conrad Röntgen performed experiments with cathode rays from gas discharge tubes and observed the fluorescence of coated papers, even with material shielding. He investigated these effects and discovered a novel kind of radiation which is able to penetrate dense material, the originally called "X-Strahlen" [Rön1898]. In 1901, W. C. Röntgen was awarded with the first Nobel Prize in physics for the discovery of x-ray radiation. Henri Becquerel's work on phosphorescence of uranium salts in 1896 lead to the accidental discovery of radioactivity, which is the spontaneous decay of radionuclides. Marie Curie investigated the decay of uranium compounds and established the term "radioactive". In 1903, she shared the Nobel Prize in physics with H. Becquerel and her husband Pierre Curie. These scientific findings, discovered over 100 years ago, are the basis for modern clinical high tech applications in the field of medical diagnosis and therapy.

There are two different kinds of radiation, ionizing and non-ionizing radiation. Non-ionizing radiation consists of electromagnetic waves that have less energy (< 3 eV) than is usually necessary for ionizing an atom. Examples are infrared-light or visible light. Ionizing radiation, in turn, can be separated into different kinds of radiation. Particle radiation, like α-radiation, β-radiation, or neutron radiation, consists of matter while radiation like UV-light, x-rays or γ-radiation are electromagnetic waves. The focus in this work is on detection of x-rays. An important fact hereby is that irradiation of material with x-rays is always accompanied with the production of secondary electrons, the β-radiation.

Three effects describe the interaction of x-rays with matter: the photo-effect, the Compton effect and pair production. The photo effect produces secondary electrons by ionization of atoms with photons. This is the dominating effect at x-ray energies below 500 keV. The Compton effect is the elastic collision of photons on free electrons which is accompanied with an energy transfer from the photon to the electron. Pair production describes the production of an electron-positron pair. Therefore a minimum photon energy of $2m_ec^2$ = 1.022 MeV is necessary, while m_e is the mass of an electron/positron. How deep x-rays penetrate a material strongly depends on the mass attenuation coefficient μ/ρ which is a material related constant and shows a dependence on the photon energy E = hν (Planck constant h = $6.6261 \cdot 10^{-34}$ Js, ν = photon frequency) and the atomic number Z of the material. Following approximations to the Z and E dependence of the mass attenuation coefficients are valid near the 100 keV regime [Rus2007, Pod2006].

$$\left(\frac{\mu}{\rho}\right)_{photo} \propto \frac{Z^3}{(h\nu)^3}; \quad \left(\frac{\mu}{\rho}\right)_{Compton} \propto \frac{1}{h\nu} \tag{1.1}$$

The linear attenuation coefficient μ could be derived by multiplying the mass attenuation coefficient with material density ρ. The relative transmitted intensity I/I_0 through a material with thickness d is then described by an exponential decay.

$$\frac{I}{I_0} = \exp^{-\mu d} \tag{1.2}$$

The dose D is defined as energy E absorbed per mass m. The unit is the joule per kilogram (J kg^{-1}) and named gray (Gy). The dose rate R is the dose D per unit time t.

$$D = \frac{E}{m} \left(\frac{J}{kg} = Gy\right) \tag{1.3}$$

$$R = \dot{D} = \frac{\partial D}{\partial t} \left(\frac{Gy}{s}\right) \tag{1.4}$$

The unit gray only defines a physical effect, the interaction of radiation with matter, but provides no information about possible biological effects. Different types of radiation have different biological effects on living tissue. To take this into account, radiation weighting factors q are introduced which describe the relative biological effectiveness. For example the factor is 1 for x-rays and β-particles, 5-20 for neutrons according to their energy and 20 for α-particles [ICRP1990]. The equivalent dose H is the product of absorbed dose D and weighting factor. The unit is also joule per kilogram (J kg^{-1}) but is given the special name sievert (Sv).

$$H = q \cdot D \ (Sv) \tag{1.5}$$

The question of what unit dosemeters, for example ionization chambers, measure is, in many cases, misleading. Sometimes the term “absorbed dose to air” or “air dose” is used but in reality not the energy absorbed by air is measured but the energy transferred to charged particles, resulting from the ionization. Therefore the term “air kerma” is introduced. Kerma is an acronym for “kinetic energy released in matter”. The unit is Gy. Since at high energies photons and particles are able to leave the detection volume, the air kerma is higher than the absorbed dose. However, for photon energies used in this work both units are almost equivalent.

1.2 X-ray detection and dosimetry

It is important to carefully differentiate between the two terms “detection” and “dosimetry”. For example, x-ray detectors such as Geiger-Müller counters yield no information about the x-ray dose and only produce a signal which is proportional to the intensity. These devices are able to detect x-rays but do not provide dose dependent signal readings. However, dosimetry is defined as the measurement of radiation doses in order to estimate possible health risks. Therefore it is necessary to obtain information about the absorbed dose, which is dependent on the energy of the radiation as well as the atomic number Z and the density ρ of the absorbing material.

The mass energy attenuation coefficient μ/ρ_{en} multiplied by the photon energy fluence, gives the quantity kerma. When the processes are not dominated by energy loss due to scattering, the attenuation coefficient is equal to the absorption coefficient [Boh2007]. The mass energy attenuation coefficient μ/ρ_{en} for gallium, compared to that of dry air at sea level, is shown in figure 1.1. The absorption of the material is changing with the x-ray energy. At an x-ray energy of 10.3671 keV, the absorption edge of the K shell is observable, while three absorption edges of the L shell occur at energies between 1.1 and 1.3 keV [Hub2004]. For making kerma measurements, the change in absorption needs to be compensated to a "standard". Usually, the air kerma is of interest, but changes with the x-ray energy. A difficulty is that typically, and especially in medical diagnostics, the x-ray beam has not a single energy but is composed of an energy spectrum. Therefore, a detector material which shows a similar mass attenuation coefficient than air would be ideal, but this requirement is usually not easy to achieve. Different methods are possible for calibrating the absorption of the detector material against the absorption of air. For some types of detectors the material itself can be enhanced, for example by using a different compound. Another method is to use filters which modulate the energy dependent absorption in such a way that the absorption in the detector becomes similar to that of air. For active devices, it could also be possible to tune the radiation response according to different energies.

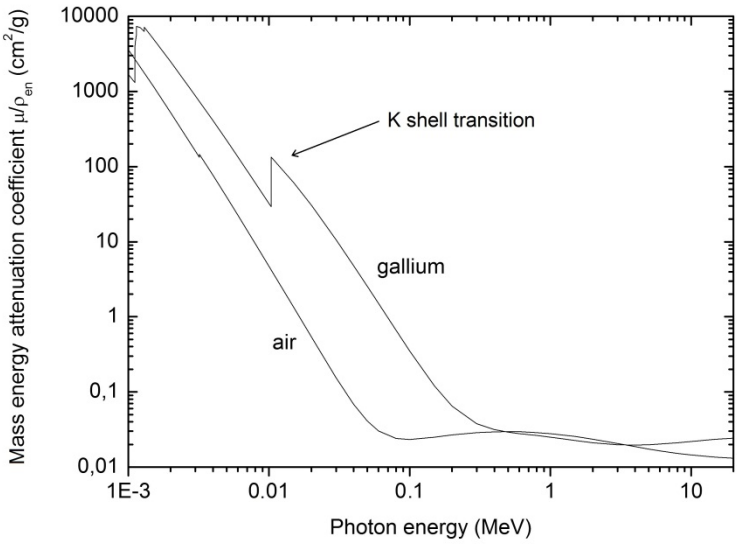

Figure 1.1: Mass energy attenuation coefficient μ/ρ_{en} for air at sea level and gallium. The data is obtained from the NIST online database [Hub2004]. http://physics.nist.gov/xaamdi (last update 2004)

It is important to emphasize that the air kerma is a universal quantity to be measured but gives no information about the absorbed dose in an irradiated sample. Therefore, another conversion of the measured value is necessary; the compensation of the energy related x-ray attenuation in air to that of the sample. Since this conversion is independent of the detector material, it can be carried out in a retrospective way. Many libraries are available for the conversion of air kerma to the kerma of common materials. Another way of dosimetry is using

detectors and filters that are not calibrated to air but directly calibrated to the absorbing sample, for example human tissue. The additional calibration to air becomes needless and the detector reading yields direct information about the absorbed dose in the irradiated sample. A disadvantage of this method is that the dosimeter is only valuable for measuring samples with the same material and density, while in reality, compounds are often irradiated. For example, the attenuation coefficient in human bone is 5.36 times higher than in human tissue at an x-ray energy of 50 keV but only 1.16 times higher at an energy of 150 keV [Hub2004].

The “gold standard” for measuring the air kerma of ionizing radiation is the ionization chamber. An electric field is applied between two electrodes. Radiation ionizes a gas between the electrodes and the field collects the produced free electrons. Used gas types are for example air, oxygen, nitrogen, or hydrogen. The amount of produced charge carriers is proportional to the released energy in air, which is measured by electric data acquisition. Ionization chambers are very reliable and have a high sensitivity, combined with a good stability. However, this technique of measuring the air kerma has a significant disadvantage: the sensitivity is proportional to the detection volume [Ley2003] and they thus have a poor spatial resolution. Further development of radiation-related technical and clinical procedures requires detectors that have high sensitivity, stability, and resolution. In recent years, several devices, including MOSFETs, Schottky diodes, silicon detectors, and scintillation dosimeters have been developed which have higher spatial resolutions than ionization chambers [Bed2007, Ehr2005, Sel2003, Vat1993, Ros2006, Pee1999]. Nevertheless, these detectors also possess a number of disadvantages, such as limited energy detection ranges, an x-ray energy dependent response, and/or a limited device lifetime. Besides new detector development, new materials have also been introduced for possible radiation detection purposes. Some examples are GaAs [Lau1996], SiC [Ber2003], and bulk diamond [Bet2010]. The high quality of these materials has been historically lacking and defect-related photo-dynamics have dominated device responses in a largely irreproducible manner. However, recent advances in crystal growth have led to improved film qualities at reduced costs, thus making the development of devices based on wide bandgap materials for such applications a worthwhile endeavor.

For particle detection, scintillators in combination with a photo-multiplier tube (PMT) or a photo-diode are also commonly used. Examples for scintillators are organic materials such as polymers and plastics or inorganic materials such as sodium iodide (NaI) and zinc sulfide (ZnS). A particle excites the scintillator material, which results in a de-excitation accompanied by luminescence. The produced photons are recorded, amplified and transferred into an electrical signal in a PMT or a diode. Nevertheless, recent novel developments were introduced in the area of particle detection and also detectors with a very high spatial resolution were developed. Silicon strip detectors [Bel1983] consist of n-type bulk silicon with implanted p-type silicon strips. After applying an electrical field between an aluminum backplane and insulated aluminum strips on the p-type silicon, produced charge carriers excited by particles can be collected with a high spatial resolution. In recent developments these kinds of detectors were also tested for possible photon detection in computer tomography (CT) applications [Bor2010].

1.3 Gallium nitride semiconductors and heterostructures

Gallium nitride (GaN) is a group III-IV semiconductor with a wide bandgap of 3.4 eV when grown in the hexagonal wurtzite structure. It is also possible to grow GaN in a zincblende structure but due to electrostatic interactions the wurtzite structure is more stable. GaN crystals are usually grown by metal organic vapor phase epitaxy (MOVPE). Hydrogen chloride in gas phase reacts with hot liquid gallium to gallium chloride. At temperatures > 1000°C the gallium chloride reacts with ammonia at crystal nuclei to form a solid gallium nitride crystal with the release of hydrogen chloride. Equation 1.6 shows the chemical reaction.

$$(CH_3)_3Ga + NH_3 \rightarrow GaN + 3(CH_4) \tag{1.6}$$

The main problem in GaN growth is the production of large single crystals. Therefore, sapphire substrates are often used for the growth of GaN thin films. Due to a lattice mismatch of the substrate and complications in the growth process itself, various kinds of structural defects in the GaN layer arise: threading dislocations, stacking faults, nanopipes, inversion domain boundaries, and misfit dislocations, generated at the heterointerface [Hon2008]. These defects have a direct influence on electron mobility and therefore alter the characteristics of a GaN device. The quality of single crystals has improved substantially in recent years and this is a major reason why the developments of GaN radiation detectors, presented in this work, became possible.

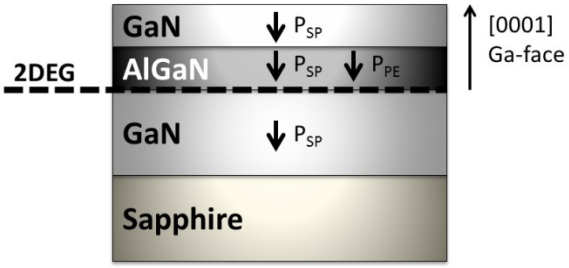

Figure 1.2: Schematic layout of a high electron mobility structure. Spontaneous polarization P_{SP} arise due to an intrinsic asymmetry of the bonding in the equilibrium wurtzite crystal structure and the piezoelectric polarization P_{PE} due to strains at material interfaces. The growth direction of Ga-face GaN is [0001] and indicated with the arrow.

GaN films have a polarity because of a missing center of symmetry of the wurtzite structure. Cations and anions form bilayers what give rise to polar surfaces. Epitaxial growth is typically carried out along the polar axis in the [0001] direction for Ga-face polarity [Dim2000, Bau2011]. The bracketed numbers are Miller indices for trigonal and hexagonal crystal structures and the brackets define a directional vector. The structure is called N- or Ga-face, depending on whether the top layer consists of a gallium layer or a nitrogen layer of atoms. It is necessary to emphasize that due to different processing and reconstruction techniques of GaN, this statement illustrates a simplified picture. Due to different growth techniques, it is

possible to produce GaN wafers in both polarizations. MOVPE growth, as well as the integration of an AlN nucleation layer for molecular beam epitaxy (MBE) results in Ga-face polarity, structures which are used exclusively for this work. The polarity has a strong influence on the spontaneous polarization P_{SP} and the piezoelectric polarization P_{PE} of the GaN films and its alloys and also defines the surface chemistry.

The heterointerface

For AlGaN the spontaneous polarization is higher than for GaN and the lattice constants are different. The strain at an AlGaN/GaN heterointerface results in an additional piezoelectric polarization. Therefore, the total polarization without an external field is the sum of the spontaneous polarization at zero strain and the piezoelectric polarization induced by strain [Hon2008, Lin2004, Amb1999], as illustrated in figure 1.2.

$$P_{SP}(Al_xGa_{1-x}N) = [-0.090x - 0.034(1-x) + 0{,}0021x(1-x)]Cm^{-2} \quad (1.7)$$

$$P_{PE} = 2\varepsilon_s\left(e_{31} - e_{33}\frac{C_{13}}{C_{33}}\right);\ \varepsilon_s = \frac{a-a_0}{a_0} \quad (1.8)$$

C_{ij} are components of the elastic tensor and e_{ij} are components of the piezoelectric tensor. ε_s is the strain deviation of the lattice constant ($a - a_0$) normalized to the unstrained lattice a_0. The following relation can be found between the alloy composition x and the piezoelectric polarization by interpolating the constants e_{31}, e_{33}, C_{13}, and C_{33} , which are published elsewhere [Lin2004, Wri1997, Zor2001, Ber1997, Deg1998, Tsu1981].

$$P_{PE}(Al_xGa_{1-x}N) = [-0.0525x + 0.0282(1-x)]Cm^{-2} \quad (1.9)$$

The result of these polarizations are surface and interface charges which are compensated by free charge carriers, provided by dopants or defects. The polarizations and the resulting internal electric fields cause a bending of the conduction band below the Fermi level [Ste2008], as shown schematically in figure 1.3.

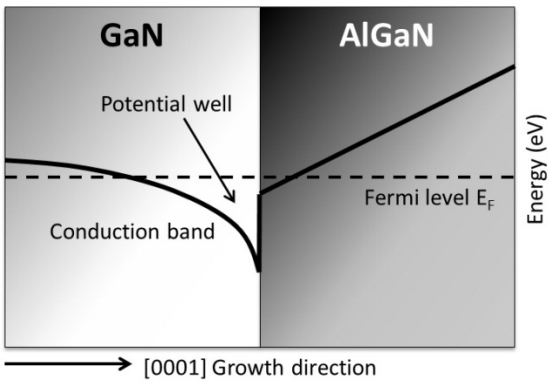

Figure 1.3: Schematic illustration of the band bending of the conduction band (CB) at the GaN/AlGaN material interface. The CB is bend below the Fermi level E_F, resulting in an accumulation of free electrons in the potential well.

Exact calculations of band edges can be done by a self-consistent solution of the Schrödinger and Poisson equations. The band bending results in a charge carrier density of free electrons, localized and confined only within a few nm parallel to the heterointerface – the two-dimensional electron gas (2DEG) [Amb2000].

The surface/electrolyte interface

Not only the potential distribution inside the heterostructure, but also the electric conditions at the surface of the device, especially when exposed to fluid, plays an important role for the formation of charge carrier densities. Potential characteristics at the semiconductor/liquid interface are usually described by the Gouy-Chapman-Stern model, which is a combination of the Gouy-Chapman theory and the Helmholtz model for double layers. Ions, which are H^+ and OH^- for oxidic surfaces, adsorb to the semiconductor surface due to chemical interactions and form a charged layer [Bau2011]. The second layer is formed by ions attracted by the Coulomb force due to the presence of the first layer. This double layer causes a potential drop ϕ_{GCS} at the electrolyte relative to the surface potential of the semiconductor ϕ_S. The relation of the external voltage V_G and the internal potential is given by the following equation and a schematic potential distribution at the surface is given in figure 1.4 [Ste2008].

$$eV_G = E_{bulk} - e\phi_{SC} + e\phi_{GCS} - e\phi_{RE} \tag{1.10}$$

E_{bulk} is the energy difference between the conduction band and the Fermi level ($E_C - E_F$), ϕ_{SC} the barrier height due to band bending in the semiconductor, and ϕ_{RE} the electrochemical potential of the reference electrode. The term ($E_{bulk} - e\phi_{SC}$) represents the increased surface potential ϕ_S relative to the Fermi level, due to band bending at the material interface.

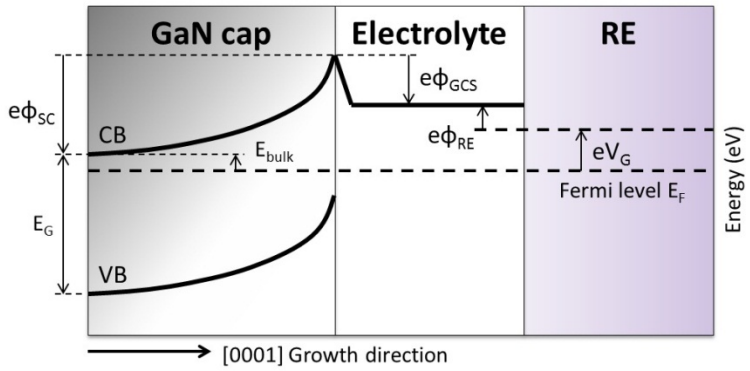

Figure 1.4: Qualitative illustration of the band characteristics at the GaN/electrolyte interface and the interface of the electrolyte and an immersed reference electrode (RE). E_{bulk} is the energy difference of the Fermi level and the conduction band of the bulk material, ϕ_{SC} the barrier height of the semiconductor at the surface, ϕ_{GCS} the potential drop caused by the Helmholtz double layer in the electrolyte, ϕ_{RE} the electrochemical potential of the RE, E_G the bandgap, and V_G the gate potential.

At the GaN surface there is an oxide termination that forms hydroxyl groups in wet environments. Depending on the proton concentration in the fluid, the metal oxides are left

negatively charged (Ga-O^-), neutral (Ga-OH), or positively charged (Ga-OH_2^+), [Bau2011]. Therefore a pH sensitivity of the heterostructure [Ste2003a] can be explained by the affinity of the GaN surface to oxygen of water molecules [Bau2011] and the pH has a direct influence on the surface potential ϕ_S of the semiconductor [Ste2008],

$$\phi_S = E_{bulk} - e\phi_{SC} = 2.303(pH_0 - pH)\frac{kT}{e}\left(\frac{\beta}{1+\beta}\right) \tag{1.11}$$

where pH_0 is the pH value at which the surface is not charged and electrically neutral. Equation 1.11 is valid for pH values in the range of pH_0. β is the sensitivity factor for the GaN surface which depends on the Helmholtz double layer capacitance, the density of surface sites and the surface reactivity. For β > 10 the relation approximates a linear Nernstian pH-dependence [Ste2008].

1.4 Gain model of GaN photoconductors

In contrast to conventional photodetectors, which are based on a measurable current due to a separation of electron-hole pairs, GaN detectors show effects that cannot be described only with the simple model of charge carrier generation, as demonstrated in detail in the results section. Muñoz *et al.* proposed a photoconductive gain mechanism in GaN ultraviolet detectors which describes the observed effects: high photoconductor gain, nonlinear response with illuminating power, and an intrinsic non-exponential photo-conductance recovery process which is very slow [Mun1997]. Since the same effects are observed when operating the devices as x-ray detectors, photoconductive gain mechanisms can be explained by the models proposed by Muñoz *et al.* and Garrido *et al.* [Mun1997, Gar1998], as shown in the following section.

The surface charge density Q_{SC} is related to the barrier height ϕ_{SC} caused by band bending at the semiconductor surface,

$$Q_{SC} = \sqrt{2q\varepsilon N_d \phi_{SC}} \tag{1.12}$$

where N_d is the doping level, q the electron charge and ε the permittivity. The width of the space charge region in darkness d_{dark} can be calculated by dividing the surface charge density Q_{SC} by the volume charge density qN_d. The thickness of the space charge layer therefore depends on the barrier height ϕ_{SC}.

$$d_{dark} = \frac{Q_{SC}}{qN_d} = \sqrt{\frac{2\varepsilon}{qN_d}\phi_{SC}} \tag{1.13}$$

The production of charge carriers during illumination results in generation of a photo-voltage V_{ph} and the thickness of the conductive layer is altered to d_{light} [Gar1998]. There is a splitting of the Fermi level to quasi Fermi levels for electrons and holes. The excess photo-generated carriers screen fixed charges, which leads to a reduced band bending (dashed line) of the conduction band, illustrated in figure 1.5.

$$d_{light} = \sqrt{\frac{2\varepsilon}{qN_d}\left(\phi_{SC} - V_{ph}\right)} \tag{1.14}$$

This transverse photovoltaic effect not only occurs at the surface of the device but also at material interfaces, including within a HEMT.

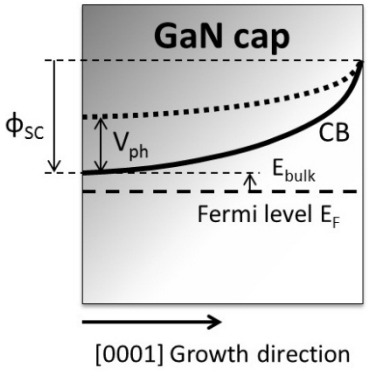

Figure 1.5: Qualitative illustration of the alteration of the conduction band (CB) due to a photo-voltage V_{ph} [Gar1998]. The additional potential is caused by filling of states above the conduction band due to the production of electron-hole pairs by the photo effect. This potential alteration results in a change of the conductive volume of the semiconductor.

Experiments and numerical investigations have shown a much lower device response caused by the increase of charge carriers compared to the biased device response due to an alteration of the conductive cross sectional area ΔA of the semiconductor [Gar1998]. Therefore the total device response ΔI_{SD} can be given by following equation [Gar1998], whereas w is the width and l the length of the active area, μ is the electron mobility, n the charge carrier density and U_{SD} the source drain bias of the device.

$$\Delta I_{SD} = \frac{\Delta A}{l} q\mu n U_{SD} = \frac{\mathrm{w}\left(d_{dark} - d_{light}\right)}{l} q\mu n U_{SD} \tag{1.15}$$

$$\Delta I_{SD} = \frac{w}{l}\left[\left(\frac{2\varepsilon}{qN_d}\phi_{SC}\right)^{1/2} - \left(\frac{2\varepsilon}{qN_d}\left(\phi_{SC} - V_{ph}\right)\right)^{1/2}\right] q\mu n U_{SD} \tag{1.16}$$

As mentioned above, this model was originally developed to describe the photo-response of GaN devices for photon detection in the UV range. However, since the devices show similar

characteristics for exposure to x-rays, it is probable that thus device response could be explained using the same considerations. This assumption is supported by the fact that, while the measurements are performed at a different energy regime of illumination, the detection itself is related to the same basic mechanism: the interaction of photons. Therefore the x-ray measurement with GaN buffer layers, presented in chapter 3, are most probably based on the gain model proposed by Muñoz *et al.* and Garrido *et al.* [Mun1997, Gar1998].

1.5 Biosensors

The basic concept of a biosensor is based on the coupling of a biologically active system, the bioreceptor, with a signal transducer. The immobilized biological sensing element on the device interacts with the analyte, resulting in an alteration of the physical or chemical environment. These alterations are recorded and transferred into an electrical signal by a signal transducer. A biosensor combines two different tasks: the measurement of bio-chemical processes and the processing of physical or chemical signals. A schematic overview is given in figure 1.6.

The bioreceptor alters the local environment due to the presence of an analyte. The primary requirements are a high selectivity and high sensitivity for the analytes of interest, which are predetermined by the used bioreceptor. Examples for bioreceptors are antibodies, DNA, cells or microorganisms. The transducer converts the recognition event of the bioreceptor into a recordable signal which can be amplified and further processed.

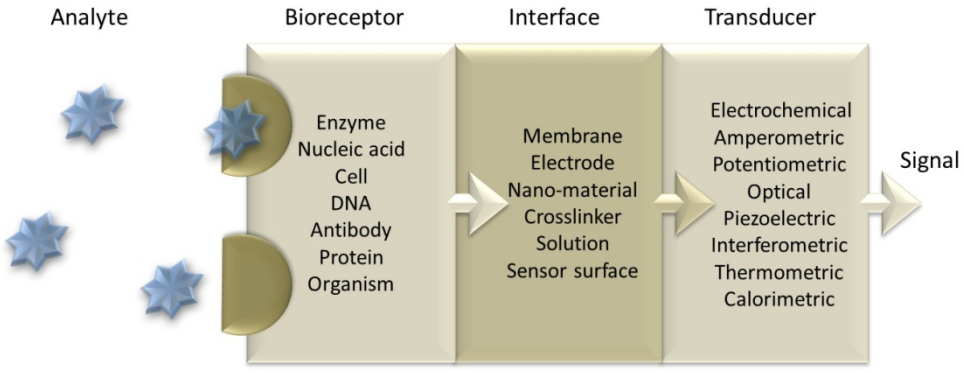

Figure 1.6: Schematic illustration of the basic operation principle of a biosensor. An interaction of the analyte with the bioreceptor causes an alteration of the bio-chemical environment, which is in turn identified and translated into an electrical signal by a transducer.

The first biosensor, a blood glucose sensor, was developed in 1962 by Clark and Lyons [Cla1962]. Glucose oxidase, which oxidizes glucose with a catalytic reaction, was immobilized between membranes. The amount of electrons changes proportional with the oxidation and could be directly measured with electrodes via an electrical current change. Within recent decades, a broad range of different types of biosensors have been developed:

- Mechanical, often piezoelectric, sensors measure the presence of an analyte due to a mass change and the resulting alteration of the oscillation frequency.

- Optical sensors utilize the fluorescence, luminescence or the absorption characteristics of a bioreceptor.

- The change of film thickness of a polymer layer interacting with biomolecules is employed by interferometric sensors.

- Thermometric or calorimetric biosensors measure temperature changes caused by a biochemical reaction.

- Electrochemical sensors can be divided into two parts: amperometric sensors, for example the Clark electrode, and potentiometric sensors. While amperometric sensors measure the electrical current at a constant bias voltage, which is changed by the presence of the analyte, a potentiometric sensor measures the electrical potential caused by the accumulation of charge carriers without a current flow.

In this work, GaN-HEMTs are operated as ion sensitive field effect transistors (ISFETs). The operating principle is that of a potentiometric biosensor. The device itself works as transducer which translates the accumulation of ions at the device surface and inside an electrolyte into an electrical current. GaN based devices have already been introduced into biosensing applications [Yu2007]. For example living cells, which are immobilized on the sensor surface, could be used as bioreceptor. The device detects alterations of surface charges, such as pH changes, in the extracellular environment [Ste2005].

A major requirement for materials used for biosensing purposes is the biocompatibility. It is generally assumed that the more biocompatible the surface, the greater the degree of cell adhesion [Ric1996]. For adherent growing cell cultures, the cell adhesion can be determined by evaluation of the outer shape after attachment. However, rigorous studies of biocompatibility extend beyond measures of the chemical inertness of the material-cell interface. Consequently, biocompatibility has been defined operationally to apply to materials that minimally perturb the *in vivo* environment and that are, likewise, not adversely affected by the *in vivo* environment [Rei2000]. Nevertheless, information about biocompatibility and cytotoxicity of semiconductor materials is often deficient. Thus, negative effects on the host caused by material-cell interactions are frequently neglected when semiconductor devices are used as test systems on a cellular level. Therefore extensive biocompatibility studies, as well as biofunctionality studies, are presented in chapter 6.3 and GaN based materials are evaluated regarding their applicability as biosensors.

1.6 Scope of this work

The annual average exposure to radiation produced by mankind in Germany is about 1.8 mSv [BfS2010]. This value can be misleading because the number is calculated by averaging over the general public. Almost all artificial exposure is caused by clinical procedures. While there is a share of population which is either not at all or much less exposed to man-made radiation, the consequence is that another share of population is exposed to much higher doses. For instance, a computer tomography of the abdomen leads to an effective dose of 10 – 25 mSv, while the limit for job-related exposures is 20 mSv/a according to the German Strahlenschutzverordung (Radiation Protection Regulations) [StrlSchV2011]. For doses in this range, health effects cannot be neglected and therefore, accurate dosimetry is necessary in order to balance the harm with the benefit for patients and to maintain the limits for workers and the population. X-ray radiation plays an important role in medical procedures ranging from diagnostics to therapeutics. Due to the harm such ionizing radiation can cause, it has become common practice to closely monitor the dosages received by patients and workers. To this end, precise online dosimeters have been developed with the dual objectives of monitoring radiation in the region of interest and improving therapeutic methods. Ionization chambers are widely used in medical dosimetry due to their stability and wide range of operation. However, further development of radiation-related clinical procedures requires detectors that have high sensitivity combined with a high spatial resolution. In recent years, several devices, including MOSFETs, bulk diamond, Schottky diodes, and scintillation dosimeters have been developed which provide an increased spatial resolution. Nevertheless, these detectors also possess a number of disadvantages such as a limited energy detection range, an x-ray energy dependent response, and/or a limited device lifetime.

In this work, high electron mobility transistors (HEMTs) based on gallium nitride (GaN) and GaN thin films are evaluated regarding x-ray sensitivity. These devices could overcome a range of the drawbacks related to conventional radiation detectors which possess a high spatial resolution. Although the detection volume is several orders of magnitude smaller than ionization chambers, the measurement characteristics of the device are partially comparable with those of ionization chambers. The aim of this work is the development of sensitive, stable and small radiation detectors that can be introduced in a variety of applications, ranging from patient dosimetry to the monitoring of radioactive waste. It is possible to further enhance this application space by revealing the additional sensitivity of the devices not only to photons but also to charged particle radiation, such as protons.

Radiation biophysics is a field which investigates the influence of ionizing radiation to living organisms, ranging from single cells to whole species. Measuring direct radiation effects in living organisms is a complex endeavor since measurement tools or biosensors are exposed to ionizing radiation, which in turn could induce measurement errors or damage to the sensors. Since GaN-HEMTs have already been introduced for biosensing applications, especially for measuring the pH, it is a logical extension to evaluate the devices for radiation hardness and their capability of measuring physiological parameters, such as pH, during radiation exposure. The aim is to develop a tool which could give new insights into biological behaviors of organisms, not in a retrospective way but in real-time during the exposure to x-rays in irradiation experiments.

2 Material and Methods

2.1 GaN high electron mobility transistors and GaN thin films

The GaN devices were produced using a MOCVD-based growth process by TopGaN Ltd. (Warsaw, Poland) or Lumilog (Vallauris, France) on 330 µm thick sapphire substrates. In this work the terms “HEMT devices” and “thin GaN films or GaN barrier layers” are used to refer to these samples.

The HEMT devices, illustrated in figure 2.1, consist of a multi-layer structure of GaN and AlGaN. At the material interface, a two-dimensional electron gas (2DEG) is produced due to piezoelectric polarization of the materials. Electrons inside the 2DEG have a higher mobility compared to the bulk GaN material because of a separation of free charge carriers from ionized impurity centers. Therefore the conductivity of the 2DEG device is higher.

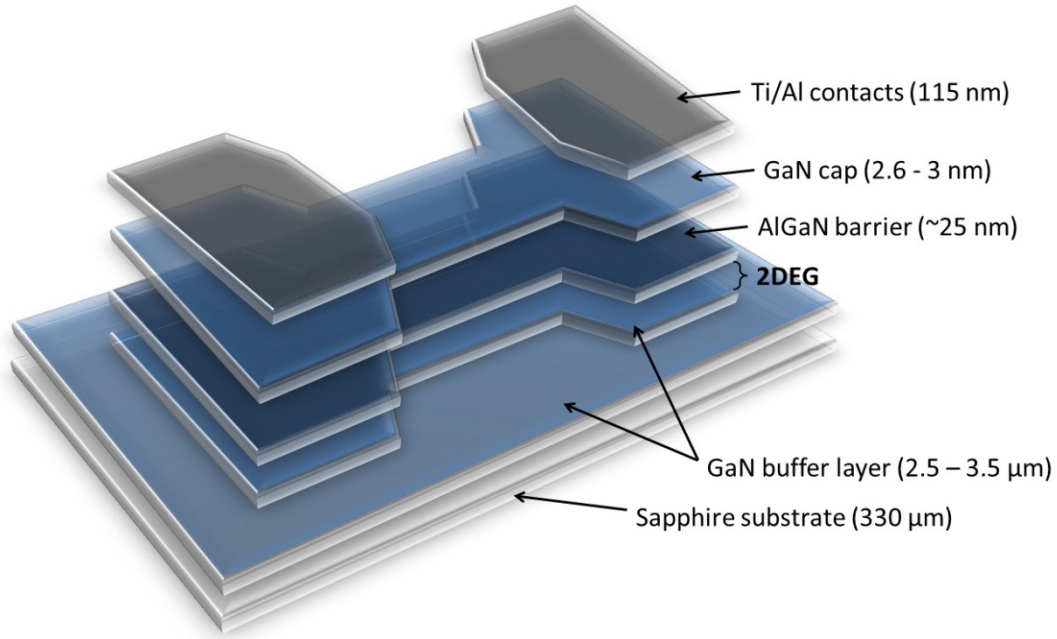

Figure 2.1: Schematic layout of a GaN high electron mobility transistor (HEMT). The GaN/AlGaN/GaN heterostructure is grown on a sapphire substrate. The mesa structure is produced by BCl_3/Cl_2 plasma reactive ion etching from the top until the GaN buffer layer is reached. Ti/Al contacts are produced by thermal evaporation. The two dimensional electron gas (2DEG) is located between the AlGaN barrier and the GaN buffer layer for Ga-face material.

The samples named “thin GaN films” or “GaN buffer layers” only consist of a single GaN material layer without the formation of a 2DEG. These devices could be produced by either contact evaporation on a wafer consisting of a single material layer or by etching the HEMT devices down to the GaN-buffer layer.

The detailed fabrication methods for the HEMT devices are described elsewhere [Mur1999]. The processing of the samples is described in the next chapter. Table 2.1 summarizes the different types of samples used in this work: TG1592, TG1416, TG400 and TG401 are HEMT wafers and 07-535, TG1797, TG18000 and MG01 are single thin film structures.

Wafer name	Substrate (µm)	GaN-buffer (µm)	AlGaN-layer (nm)	Al content (%)	GaN cap (nm)	Compensation species
TG1592	330	2.65	25.6	31.2	3.0	C
TG1416	330	2.5	25.0	23.0	2.6	C
TG400/401	330	2.5	25.0	25.0	3.0	C
07-535	330	3.5	-	-	-	Fe
TG1797	330	3.1	-	-	-	-
TG1800	330	3.4	-	-	-	C
MG01	330	3.5	-	-	10.0 (Mg)	Mg

Table 2.1: Summary of the wafer structures used in this work. The HEMT wafers consist of a AlGaN barrier and a GaN capping layer while other structures consist only of a single GaN layer. The sapphire substrate is equivalent for all samples. For HEMT devices, the compensation species refers to the buffer layer.

Figure 2.1 shows a schematic layout of the HEMT samples. For GaN thin film layer samples without a heterostructure or a 2DEG, the contact pads are located either directly on the GaN buffer layer without an AlGaN barrier or on the HEMT structure but with AlGaN barrier channel etched away.

2.2 Processing of GaN devices

The processing of the samples was accomplished in the semiconductor laboratories at the Walter Schottky Institute of the Technische Universität München (TUM).

As described in chapter 2.1, the single GaN layer structures and the GaN-HEMT structures were purchased in the form of 2 inch wafers. After dicing the wafers in 10 × 10 mm samples, sensors were formed through following processing steps:

1) Sample dicing and cleaning
2) Lithography for HEMT channel definition
3) Reactive ion-etching
4) Lithography for contact electrode definition
5) Contact electrode evaporation
6) Annealing of metal contacts
7) Surface treatment

Steps 2 and 3 are not applicable for processing single layer wafers without a HEMT structure.

1) Sample dicing and cleaning

Before starting with device processing, the wafer samples were cleaned with deionized water, acetone and 96% iso-propanol, for 10 min each in an ultrasonic bath. Next, the samples were treated in 30% ammonia-solution for 3 min to remove surface bound oxygen on the surface. O_2-plasma (5 min) oxidizes the surface again to provide a well-defined surface state for lithography. The oxidization was carried out with a 100-E plasma etcher (PVA TePla, Wettenberg, Germany) at 1.3 mbar and 200 W. All preparation steps were performed at room temperature.

2) Lithography for HEMT channel definition

Lithography is carried out to define the mesa structure of the HEMT channel and/or the contact pads. The wafer surface is covered with a layer of S1818 photoresist (Rohm and Hass, Philadelphia, United States) by spin coating with a rotation speed of 6000 rpm, followed by soft-baking at a temperature of 90°C on a hotplate for 2 min. A shadow mask, which defines the borders of the HEMT mesa structure, is aligned in direct contact with the photoresist using an MJB3 mask-aligner (Suss MicroTec, Garching, Germany). The shadow mask prevents fractions of the photoresist, which will later be defined as HEMT channel, from UV illumination. The illumination breaks photoactive components of the photoresist and UV exposed parts can be removed with Microposit 351 developer (Shipley Company, Marlborough, United States). This lithography processing step results in a wafer sample where

defined structures of photoresists prevent the HEMT channels from the reactive ion etch, as illustrated in figure 2.2.

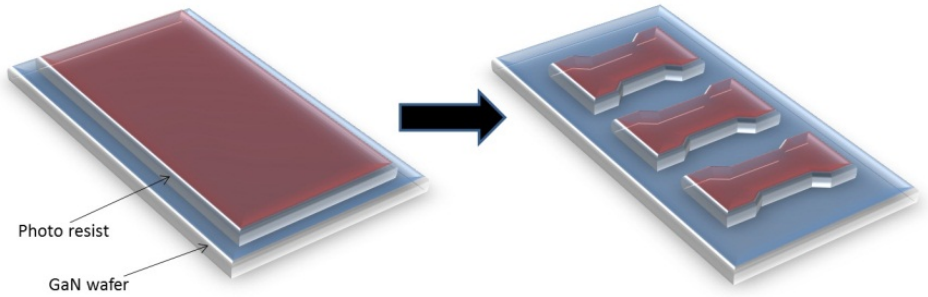

Figure 2.2: Illustration of the lithography process: the GaN/HEMT wafer is covered with a photoresist layer. Illumination with a shadow mask breaks polymers inside the photoresist. A subsequent development of the photoresist ends up with defined structures still covered with the material. This is the preparation step for etching the mesa structures with plasma reactive ion etch.

3) Reactive ion-etching

Active channel regions were defined by BCl_3/Cl_2 plasma reactive ion etching (RIE) of lithographically patterned surfaces (figure 2.3). Approximately 100 nm of material was etched during the RIE process, which was sufficient to remove the AlGaN/GaN heterointerface, and thus the 2DEG, which was located 30 nm below the surface. The remaining polarization-induced 2DEG, confined to within the mesa regions, were characterized by sheet carrier concentrations of ~8×10^{12} cm^{-2} and mobilities of ~1100 cm/Vs.

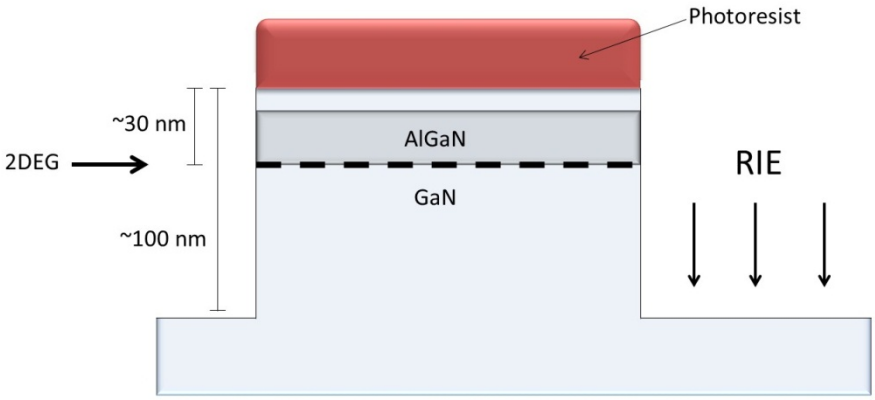

Figure 2.3: The schematic illustration shows the etching process of the mesa structures with the reactive ion etch (RIE). The structures have dimensions in the range from 20 µm to several mm. While areas covered with photoresist remain unaffected, areas without a photoresist layer are etched away until the GaN buffer layer is reached. Therefore, the 2DEG is confined to defined mesa structures.

4) Lithography for contact electrode definition

The lithography step for defining the source, drain and, for the HEMT samples, the gate electrode pad is identical to step 2. However, in this case the area where the contact pads will be located is UV illuminated and developed. Openings in the photoresist are formed, which allow deposition of metal directly on the GaN substrate during the evaporation process.

5) Contact electrode evaporation

Contact pads are produced by thermal evaporation with a Leybold-Heraeus L560 multi source evaporation system (Oerlikon Leybold Vacuum, Cologne, Germany). The metals are heated inside of a thermal evaporator until a sufficient large vapor pressure is obtained at elevated temperature. The vapor is transported to the sample and condenses on the surface (figure 2.4). The contact electrodes consist of either a 20 nm or 35 nm thick Ti layer, capped with an 80 nm thick Al layer. The deposition rate of Ti was ~0.1 nm/s and the deposition rate for Al ~1 nm/s.

Some sensor samples were cleaned in piranha-etch (see step 7) to remove organic contaminations from the substrate and for surface hydroxylation. These devices were primarily those used in experiments with biological material. To protect the aluminum layer from the aggressive solution, an additional Au layer with a thickness of 100 nm was deposited at a rate of ~0.5 nm/s onto the contact pads.

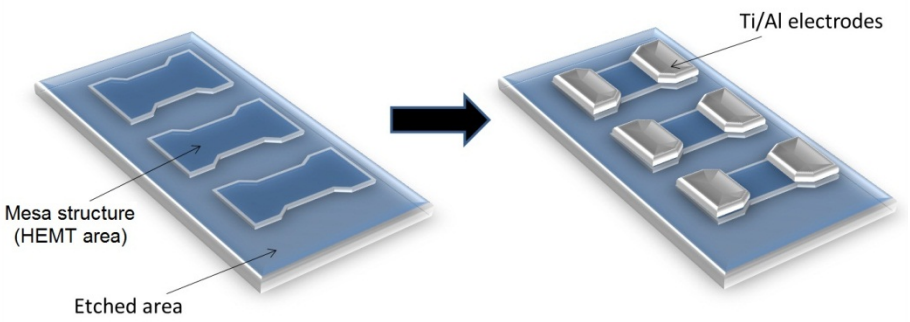

Figure 2.4: Illustration of the Ti/Al contact evaporation process. Contact pad structures are defined with photoresist on the etched mesa structure. Metal contacts were subsequently evaporated on the sample. After liftoff of the remaining material, the contact pads are confined to the defined regions.

6) Annealing of metal contacts

Metal contacts were annealed in vacuum at a temperature of 850 °C for 30 sec, followed by a 90 sec annealing at 750 °C. This procedure produces contact electrodes with ohmic behavior without degradation of 2DEG conduction.

7) Surface treatment

Piranha-etch, which is a 3:1 mixture of sulfuric acid (H_2SO_4) and 30% hydrogen peroxide (H_2O_2), is strongly oxidizing. Devices were immersed for 10 min and rinsed with deionized water for device surface hydroxylation and to remove organic contaminants. This procedure was carried out for devices that came in direct contact with cell cultures but is not necessary for radiation measurements with the GaN buffer layer.

2.3 Radiation sources

Irradiation experiments were carried out at different facilities. Large area x-ray irradiations were performed at the Helmholtz Zentrum München either at the Institute for Radiation Protection with a medical x-ray machine or in the IAEA/WHO Secondary Standard Dosimetry Laboratory with calibrated x-ray sources. Small-area x-ray irradiations were carried out at the BESSY II synchrotron in Berlin, Germany. Particle irradiations were conducted with a tandem accelerator from the Technische Universität München in Garching, Germany.

2.3.1 Large-field x-ray irradiation

Devices were irradiated in a large field using two different x-ray systems. For irradiations at dose rates above 0.2 mGy/s, a Stabilipan TR300f (Siemens AG, Munich, Germany) medical x-ray system with a 4 mm Al filter was used. Reference measurements of air kerma doses were recorded at the tube exit with a Diamentor M4 dose area product meter with a resolution of 0.01 $\mu Gy \cdot m^2$, together with a Diamentor 34015 transmission ion chamber (PTW, Freiburg, Germany) or a Dosimentor DL4 dosimeter (PTW, Freiburg, Germany) together with a free-mounted 1 cm^3 23331 ionization chamber (PTW, Freiburg, Germany). The irradiated samples were vertically positioned under the x-ray tube. Air kerma rates were recorded as a function of the sample/beam exit distance.

Low dose irradiations were performed with a MG 325 technical x-ray system with an MCN 323 tube (Philips Industrial x-rays, Hamburg, Germany) in the IAEA/WHO Secondary Standard Dosimetry Laboratory at the Helmholtz Zentrum München. Samples were irradiated on a calibration bench under TM 786 monitor control with an IQ4 electrometer (both PTW, Freiburg, Germany).

Radiation quality	Tube voltage (kV)	Filters	k_Q
N-30	30	4.0 mm Al	0.966
N-40	40	4.0 mm Al + 0.21 mm Cu	0.921
N-60	60	4.0 mm Al + 0.6 mm Cu	0.919
N-80	80	4.0 mm Al + 2.0 mm Cu	0.949
N-100	100	4.0 mm Al + 5.0 mm Cu	0.955
N-120	120	4.0 mm Al + 5.0 mm Cu + 1.0 mm Sn	0.948
N-150	150	4.0 mm Al + 2.5 mm Sn	0.946
N-200	200	4.0 mm Al + 2.0 mm Cu + 3.0 mm Sn + 1.0 mm Pb	0.940
N-250	250	4.0 mm Al + 2.0 mm Sn + 3.0 mm Pb	0.936
N-300	300	4.0 mm Al + 3.0 mm Sn + 5.0 mm Pb	0.955

Table 2.2: Calibrated radiation qualities for the Philips MG 325 x-ray source and the IQ4 electrometer. Defined filters were placed at the beam exit to provide energetic photon spectra that correspond to the calibration of the ionization chamber.

ISO narrow series radiation qualities were adjusted using filters according to table 2.2. Air kerma (free-in-air) doses were measured with a calibrated 30 cm^3 TM 23361 ionization chamber and an Unidos electrometer (both PTW, Freiburg, Germany) with appropriate corrections for radiation quality, ambient pressure, and temperature, given in equation 2.1 and 2.2.

$$\dot{D} = N_K \cdot k_Q \cdot k_\rho \cdot M \cdot \frac{1}{60s} \tag{2.1}$$

$$k_\rho = \frac{273.15K + T}{293.15K} + \frac{1013.15hPa}{p} \tag{2.2}$$

The signal reading M is proportional to the collected charge from the ionization chamber within an integration time of 60 s. To achieve the corresponding air kerma rate $\dot{D}$, this value is corrected with a calibration factor for the used ionization chamber N_K [Gy/C], a calibration factor for the beam quality k_Q and a calibration factor k_ρ for ambient temperature T and pressure p. Tabulated calibration factors were provided by measurements conducted by the Physikalisch-Technische Bundesanstalt (PTB) in Braunschweig, Germany.

2.3.2 Small field synchrotron irradiation

Experiments with synchrotron radiation are performed at the BESSY II synchrotron source in Berlin, operated by the Helmholtz Zentrum Berlin.

Electrons, produced by an electron beam gun, are accelerated first in a microtron and subsequently in a synchrotron to energies of up to 1.7 GeV. The fast electrons are stored in a storage ring with a perimeter of 240 m after acceleration (see figure 2.5). By modulating the

electron track on a circle with electromagnetic elements, the charge carriers are continuously accelerated, which results in the production of synchrotron radiation.

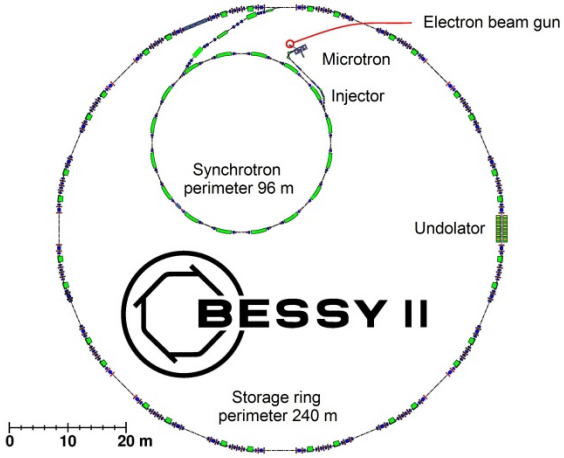

Figure 2.5: Schematic illustration of the BESSY II synchrotron. Electrons are produced by an electron beam gun and injected into the BESSY synchrotron. After acceleration of the electrons the particles are stored in the 240 m storage ring for several hours. The image is adapted from http://www.helmholtz-berlin.de/angebote/arbeiten-lernen/info/beschleunigerphysik-fuer-anfaenger/der-speicherring_de.html

During the experiments the synchrotron was operated in single bunch mode. A single electron bunch in the ring enables the users to measure with a high time resolution. Two electron bunches arrive with a delay of 800 ns, producing synchrotron radiation. Measuring stations are located outside of the storage ring. Usually the injection of electrons is performed at 4 – 5 h intervals. During injection, which takes about 15 min, no measurements are possible and therefore long-term imaging experiments need to be adapted to these time intervals. The beam currents are in the 10 – 20 mA range and show an exponential decay to a few mA during the injection intervals, due to an intensity loss of the electrons.

2.3.3 Proton irradiation

Particle irradiation experiments were carried out at the Garching Tandem Accelerator (Munich, Germany) of the Meier Leibnitz Laboratory of the LMU and TUM.

The acceleration voltage was set to 10 MeV. Therefore, protons with an energy of 20 MeV were used for the experiments since a tandem accelerator utilizes the acceleration voltage twice for energy transfer to the particles. The SNAKE set-up (superconducting nanoprobe for applied nuclear physics experiments) is a specially designed system to focus ion beams with micro-slits and magnetic lenses to a beam diameter in the several 100 nm range. Single ion hits were recorded with a scintillator connected to a photo multiplier tube (PMT).

2.4 Measurement set-up

The basic measurement setup for all irradiations at the different facilities consisted of Keithley 2400 SourceMeters (Keithley Instruments, Inc., Cleveland, Ohio) in combination with a LabView control and data acquisition. The SourceMeter devices provide the possibility to simultaneously bias the devices (U_{SD}) and measure the current (I_{SD}). Cable connections were accomplished with RG174 coaxial cables (Reichelt elektronik, Sande, Germany). The inner conductor was used for signal transmission while the shielding was connected to the LO terminal of the Keithley device. Since there is no internal connection between earth ground and the input/output LO terminal of the SourceMeter, the devices were measured in floating mode. The accuracies of the device for the used source and measurement ranges are summarized in the appendix. For almost all experiments in this work, the 200 mV source range and the 100 µA measurement range were used.

The integration time for a single data reading is specified as the number of power line cycles (NPLC), where 1 PLC for 50 Hz results in 20 ms. The integration time was usually set to NPLC 1, unless otherwise noted. Due to additional time delays for data transfer the total measurement time for single values was longer than the integration time. Measurements were usually performed with a data acquisition frequency in the 10 Hz regime.

For simultaneous measurements of numerous GaN sensors, the devices were connected in parallel to a single Keithley 2400 SourceMeter and were supplied with a 140 mV bias voltage. Signal readout was performed with a NI PCI-6229 multi-channel data acquisition device (DAQ) and a shielded BNC connector block (both National Instruments, Austin TX, United States), by simultaneously measuring the voltages across 300 Ω shunt resistors in series such that the conductance changes of the GaN-sensors directly influenced the voltage drop over the resistors. A total of 616 data points were recorded per second during the simultaneous measurement of four GaN-sensors. The DAQ device had a 16 bit resolution with a minimum sensitivity of 5.2 µV in the 200 mV range.

Control of SourceMeters and DAQs, as well as data acquisition, was performed with programs based on LabView 8.6 code (National Instruments, Austin TX, United States). The devices were connected with a GPIB IEEE-488 bus system (Keithley Instruments, Cleveland, United States) via the PCI interface.

2.4.1 Translation stage

For large-field imaging purposes, a two-dimensional translation stage was set up. The stage is utilized to remotely translate GaN sensors within an x-ray beam. Therefore, a LabView based code for the control of 2 stepper motor interfaces was developed, for X- and Y-movement of the sensor on a horizontal plane. The x-ray photons hit the sensor perpendicular to its surface and a “transmission sample” was fixed between the radiation source and the GaN sensor. The transmission sample is an object which is mapped by a measurement of transmitted x-rays photons penetrating the sample. The movement of the sensor can be programmed by

computer control. For each movement step, a preset number of measurement values were recorded with a Keithley 2400 SourceMeter. The minimum spatial resolution with the translation stage was limited to 100 µm.

For imaging experiments, pairs of lines were typically scanned, as schematically shown in figure 2.6. By performing forward and backward scans in both positive and negative X-directions, it is possible to calculate the average value and reduce errors caused by drift. The spatial resolution of the GaN devices could be increased by using a lower step width ΔX and ΔY than the dimension of the active areas of the sensors. The active area is defined as the entire area encased by the contact pads, including the area of the contact pads itself, since x-rays easily penetrate the metal electrodes.

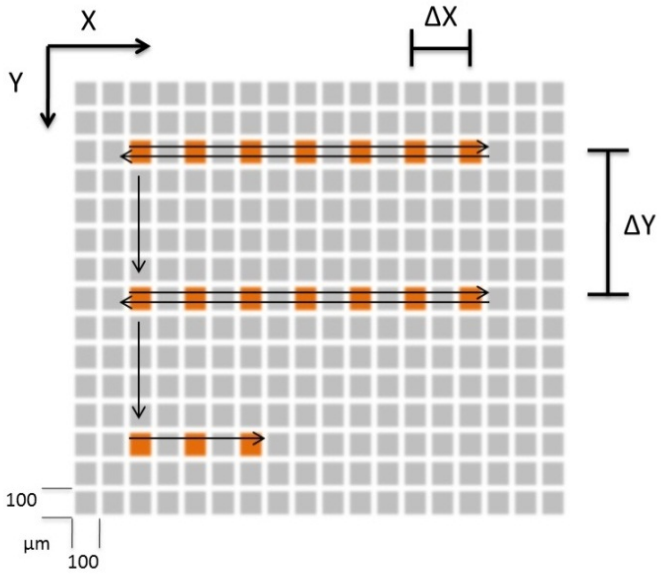

Figure 2.6: Illustration of the translation geometry of the GaN-sensor used for 2-dimensional intensity measurements. The sensor is moved in X- and Y-directions by two stepper motors with minimum step widths of 100 µm. Movement geometries are defined by transitions ΔX in the X-direction and ΔY in the Y-direction, whereas ΔX and ΔY are multiples of the step width. Line geometries are realized when ΔX << ΔY. For some experiments, lines in the X-direction are scanned twice, with a forward and a backward scan.

The translation speed of the stage could be changed either by adjustment of the number of power line cycles (NPLC) of the Keithley SourceMeter, the number of triggered measurements at each position or a programmed pause between translation steps.

2.4.2 Synchrotron irradiation set-up

Synchrotron irradiation experiments were performed with monochromatized 5-20 keV photons which were focused to a spot size of approximately 3 µm in diameter through a fixed

silica capillary. The x-ray intensity is reduced by a factor of 300 by the presence of the capillary. The photon flux was either determined using a 5 cm long FMB Oxford IC Plus Intensity Monitoring ionization chamber with a 10 mm electrode spacing or a calibrated PIN diode. The photons traverse the chamber before they hit the capillary, whereas the PIN diode was located after the capillary.

For intensity modulation, different sets of filters were utilized. A V-slit filter alters the spot size of the photon beam before entering the capillary and a set of Al and Cu filters modulates the beam by absorption. Two translation stages were used, one for the movement of the GaN sensors inside the beam and one for the movement of the transmission samples for imaging experiments. For all measurements, the GaN sensors were adjusted to a point of the x-ray beam where the spot had a diameter of ~3 µm. Therefore, a selective irradiation of the active HEMT channel, the metals contact, and buffer layer regions on a single GaN device was possible.

2.4.3 Proton irradiation set-up

A sample holder was developed for the fixation and proper alignment of the GaN sensors at the beam exit. A schematic of the irradiation geometry is given in figure 2.7 and the construction drawings of the sample holder can be found in the appendix. The sample was aligned using a horizontally mounted microscope (Axiovert, Carl Zeiss, Oberkochen, Germany) and the beam position was determined with a scintillator.

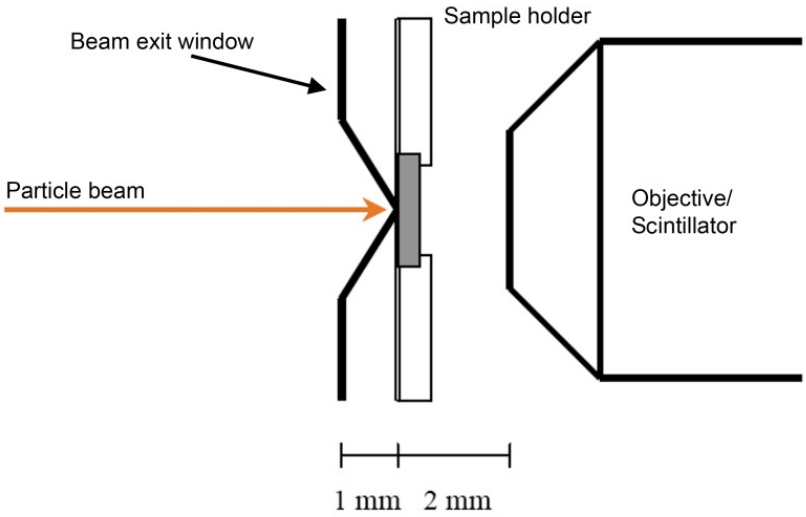

Figure 2.7: Irradiation geometry of the SNAKE set-up at the proton accelerator. The particles penetrate two foils which separate the vacuum inside the accelerator from the surrounding atmosphere and protecting the GaN sensor. The GaN surface is bombarded by protons after passing a 1 mm gap of air at ambient pressure. The particles are recorded with an objective/scintillator combination fixed on a microscope.

Voltage signals, which are proportional to the magnetic field of the magnets for beam deflection in X- and Y-directions, were recorded during the measurements. Therefore, an accurate determination of the beam position was possible. The beam is located parallel to Z-axis in this defined coordinate system. The irradiation geometry is preset with a computer control, as illustrated in figure 2.8 Irradiation centers are defined on a virtual grid while the beam translated in X- and Y-directions. The beam moves to the next irradiation center after the PMT counts a preset number of ions. To irradiate, for example, a line structure, ΔX was set to 1 and ΔY was set to 5 on a virtual grid with 1.05 µm resolution. This results in line irradiations separated by a distance of 5.25 µm but composed of point irradiations with separation distances of 1.05 µm.

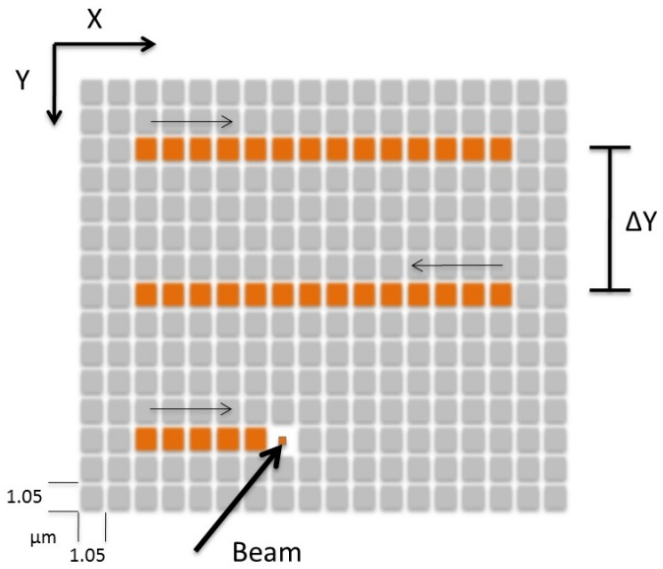

Figure 2.8: Geometry for proton irradiation at the SNAKE set-up. The proton beam could be moved by beam deflection in 1.05 µm steps in the X- and Y-directions. The sample is irradiated in a line structure by moving between neighboring points in the X-direction with a defined number of protons followed by a step ΔY in Y-direction, which is 1.05 µm multiplied with an integer. Point irradiations without a moving beam and multiple line irradiations without movement in the Y-direction were also performed.

The semiconductor samples were fixed in a free-standing configuration without the support of any additional substrate in the proton path. Therefore, the ion beam only penetrates the device (gallium nitride layer on aluminum oxide substrate) and a 6 µm thick protection film, before hitting the PMT. The beam exit of the SNAKE set-up is covered with a 7.5 µm thick Kapton foil. The entire ion transmission path before hitting the PMT is given in table 2.3.

To estimate beam broadening, the Monte Carlo code SRIM-2011 (stopping and range of ions in matter) by James F. Ziegler is used [www.srim.org]. The code calculates the stopping and range in targets consisting of different material layers in gas and solid phase. The simulated ion distribution of 1000 protons, at the Z-position where the active area of the semiconductor

devices is located, is shown in figure 2.9. The mean distance of particles from the center is 1.90 µm. Hence, the mean beam diameter at the sensitive sensor area is 3.80 µm and 97% of all protons are located within a center distance of 5 µm. However, since the calculations estimate a point source, these numbers needs to be enlarged by the real beam diameter, which is in the range of < 1 µm.

Layer Name	Width (µm)	Density (g/cm^3)	H (%)	C (%)	N (%)	O (%)	Ar (%)	Ga (%)	Al (%)
1) Kapton polyamide film	7.5	1.40	25.64	56.41	5.13	12.82	-	-	-
2) PET/Mylar Film	6.0	1.40	36.36	45.45	-	18.18	-	-	-
3) Air, dry	1000	0.0012	-	0.01	75.53	23.18	1.28	-	-
4) Gallium nitride	2.5	6.10	-	-	50.00	-	-	50.00	-
5) Aluminum oxide	330	3.97	-	-	-	60.00	-	-	40.00
6) Air, dry	> 1000	0.0012	-	0.01	75.53	23.18	1.28	-	-

Table 2.3: Composition of the materials which are transited by the proton beam. These data were used to calculate the beam broadening, which is shown in figure 2.7.

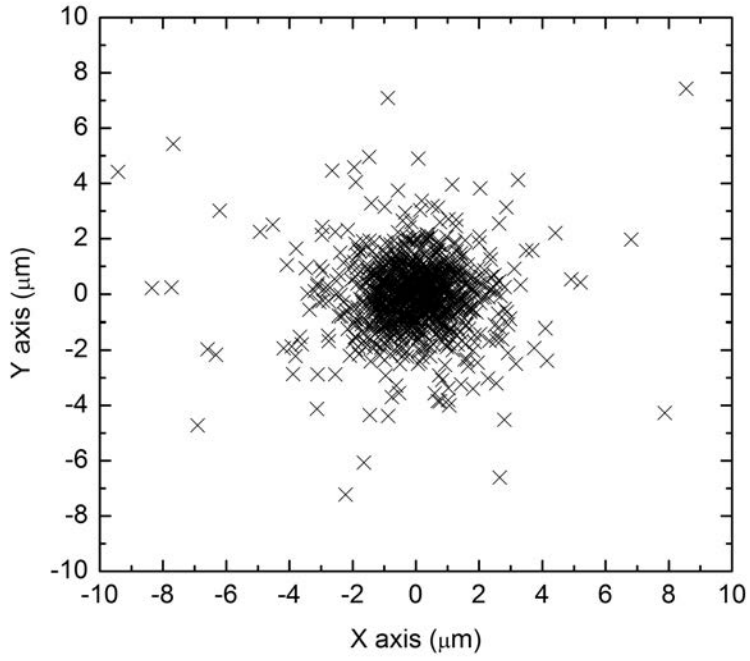

Figure 2.9: Calculated beam broadening due to beam transmission through air and synthetic material. The graph illustrates the proton distribution for 1000 particles hitting the sensor surface (for an estimated point source at the beam exit). This calculation was performed with the SRIM 2011 code and yields a medium beam widening of 3.8 µm.

Calculations have also shown that the beam spreading after a traverse of all material layers is much smaller than the area of the scintillator of the PMT and backscattering of ions is negligible at these energies. In other words: all protons are counted by the PMT after traversing the semiconductor sensors. When estimating an initial proton energy of 20 MeV the mean particle energy is 19.95 MeV when hitting the active sensor area after traversing layer 3.

2.4.4 Measurements in liquids

The sensitivity to surface potentials of the HEMT devices has been previously published [Ste2003a]. It will be discussed in detail in chapter 6.1, where it will be demonstrated that simultaneous measurement of surface potentials and radiation is possible. However, two operational modes of the sensors for measurements in fluids must be differentiated:

1) For a simple measurement of dose rates inside a fluidic volume the sensors are operated identically to measurements in air. A bias voltage in the 100 mV regime is applied and the sensor current is measured. However, the electrical contacts of the devices must be physically and electrically isolated from the solution.

2) For measurements of the surface potentials, the devices are operated as ISFETs (ion sensitive field effect transistor). This mode of operation does not restrict the possibility of radiation measurements.

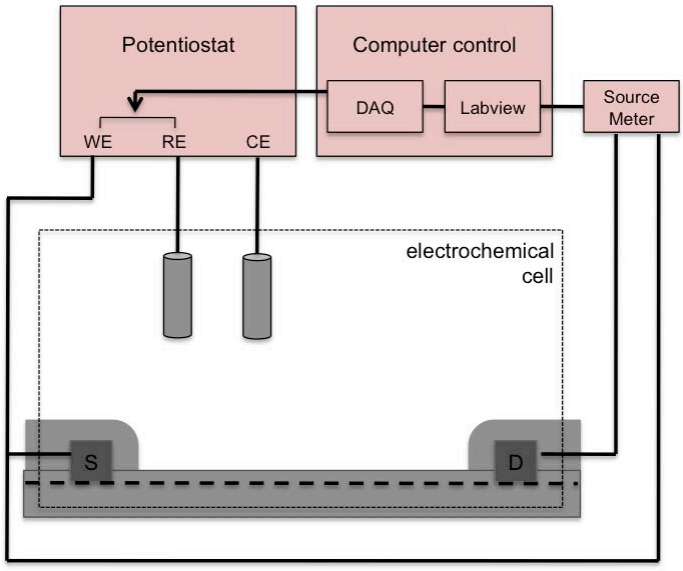

Figure 2.10: Set-up for a HEMT device operated as an ISFET. The HEMT is connected to a potentiostat as a working electrode in a three-electrode set up. The active area of the HEMT is in direct contact with an electrolyte. A gate voltage is applied with computer control as a potential between the 2DEG channel contact and the electrolyte, recorded with a Ag/AgCl reference electrode (RE). An unwanted, but possible, leakage current can flow across a counter electrode (CE).

In the ISFET mode, the semiconductor sensors are operated as working electrodes in a three-electrode set-up with a potentiostat. The reference electrode (RE) is used to define the potential of the solution relative to the working electrode, while a counter electrode (CE) is utilized to record leakage currents and to ensure that no current passes through the RE. In a three-electrode set-up a possible leakage current is flowing across the CE while the potential measurement of the RE is completely current free.

An electrochemical surface potential V_G on the sensor is defined with the potentiostat by applying a voltage on the source contact of the sensor with respect to the RE. The source-drain current I_{SD} of the sensor is set to a constant level by applying an external gate potential V_G with the potentiostat which is necessary to compensate the surface potential changes. The gate potential V_G is continuously updated with a LabView code on an external computer by a closed loop control to maintain a constant source-drain current. The set-up is shown schematically in figure 2.10.

2.5 Imaging techniques

In this work, imaging techniques such as optical imaging, laser scanning imaging, and atomic force microscopy were used. A laser scanning microscope was provided by the Institute for Pathology in Neuherberg, Germany.

2.5.1 Optical imaging

To investigate cell growth on the GaN samples, a top illumination microscope with a 3.5x objective was used (Axiovert 40C, Zeiss, Germany). For cell growth experiments, the backside of the wafer samples was polished to allow the usage of a transmission light microscope. Images were obtained with a Zeiss Observer.Z1 and a digital CCD camera (Rolera-XR, QImaging, Surrey, Canada).

2.5.2 Laser scanning microscopy

For investigating DNA repair dynamics, foci were recorded with an LSM 510 laser scanning microscope (Zeiss, Germany). In this context, “foci” means the agglomeration of fluorescent protein at DNA double strand breaks. Evaluation was performed by counting foci per single cell from Z-stacks composed of 40 picture slices through the entire cell layer with a distance of 0.3 µm between slices. Filter settings and excitation wavelength for the used dyes are given in table 2.4.

Dye	Target	Excitation wavelength (nm)	Filter settings
Alexa Fluor 488	DNA breaks	488	WFT 488/543 NFT 545 LP 530
DiO	Cell membrane	543	HFT 488/543 NFT 545 LP 650
Rhodamine Phalloidine	F-actin	514/543	HFT 488/543/633 NFT 490 BP 505-530
Hoechst	Cell nucleus	764	HFT KP 700/514 BP 435-485

Table 2.4: Filter settings and excitation wavelength for dyes used for laser scanning microscopy of cells. The order of the filter settings represents the light path, beginning at the excitation laser.

2.5.3 AFM measurements

AFM investigations were performed with the NanoWizard I (JPK Instruments, Berlin, Germany) controlled by the software JPK SPM Desktop (JPK Instruments, Berlin, Germany). Measurements of the surfaces were carried out with the cantilever model NSC15/AlBS (MikroMasch, Estonia) with a spring constant of 46 N/m and a resonant frequency of 325 kHz in tapping mode. Simultaneous optical imaging of the sample was accomplished with a DFK31AF03 firewire camera (Imagingsource, Germany) coupled to an Axiovert S 100 inverted optical microscope (Zeiss, Germany) with Epiplan Neofluar 10x/0,33 objective (Zeiss, Germany).

2.6 Tissue culture

L929 mouse fibroblasts were cultivated in RPMI media supplemented with 10% fetal calf serum and 1% antibiotic–antimycotic solution. Cells were incubated at 37 °C in 5% CO_2 atmosphere and 95% humidity and grown to a confluent layer. Before seeding on substrates, cell cultures were trypsinized, centrifuged at 1000 rpm for 3 min and re-suspended with new cell medium to overcome trypsinization effects. For splitting of the cell culture, the old cell medium was removed, confluently grown cells were washed with PBS, and trypsin was incubated for 2 min at 37 °C. After the cells detached, the cell flask was filled with 2 ml RPMI medium and the suspension was split 1:5 – 1:20 into a new cell flask containing 10 ml of fresh RPMI medium. All steps associated with cell cultures were performed in a sterile cabinet and pipettes and other equipment were sterilized with 70% ethanol to avoid contamination.

2.6.1 Cell staining with fluorophores

Immunostaining was performed using anti-53BP1 (dianova, Hamburg, Germany), Alexa Fluor 488 (Invitrogen, Paisley PA4 9RF, UK), and Hoechst 33342 (Invitrogen, Paisley PA4 9RF, UK). After the irradiation procedure and waiting for the desired repair times (30 min – 24 h), cells were washed with PBS three times and fixed for immunofluorescent staining by incubation in glutaraldehyde (2% in PBS) or formaldehyde (2% in PBS) for 15 min, followed by permeabilization with Triton-X (0.15% in PBS) for 15 min at room temperature. Blocking was performed by incubation with BSA (0.1% in PBS) for 30 min. Immunostaining was accomplished with primary antibody 53BP1 (1:100 dilution in PBS) for 1 h at room temperature in a moist chamber, followed by a washing step with PBS (5 min), 0.15% Triton-X (10 min), PBS (5 min), and 0.2% BSA (7 min). Incubation of secondary antibody labeled with Alexa Fluor 488 (1:200 dilution in PBS) for was carried out 1 h at room temperature in the dark. After a further washing step with PBS, cell nuclei were counterstained with Hoechst (1:500 solution in Hank's Balanced Salt Solution, HBSS) for 10 min and mounted in anti-fade solution Vectashield H-1000 (Vector Laboratories, Inc. Burlingame, CA).

Three-color staining of fibroblasts on GaN surfaces was achieved by labeling the cell membrane with DiO, the F-actin with Rhodamine Phalloidin and the cell nuclei with Hoechst 33342. The living cells were incubated with 0.4% DiO dissolved in RPMI medium for 20 min at 37 °C. After the membrane staining, cells were washed with PBS and fixed with glutaraldehyde (2% in PBS) for 15 min, followed by a 1 min washing step with cold PBS. The cell membranes were permeabilized with Triton-X (0.1% in PBS) followed again by a washing step with PBS. For staining the F-actin, 2.5% Rhodamine Phalloidin in PBS was incubated for 20 min at room temperature. After another washing step with PBS, the cell nuclei were stained with Hoechst and the cells were mounted in Vectashield as described above for the immunostaining.

2.6.2 Sample functionalization

Glass and GaN samples were cleaned with 70% ethanol and exposed to UV illumination with a wavelength of ~250 nm for 20 min prior to functionalization and cell seeding. For preparation of the samples with a fibronectin layer, 1.25% of fibronectin stock solution (0.1% solution from bovine plasma, Sigma-Aldrich Biochemie, Germany) solved in HBSS (GIBCO Hank's balanced salt solution 1x, Invitrogen GmbH) was incubated on the surfaces at 37 °C for 20 min and, after removing the supernatant, air dried for 20 min in a sterile cabinet.

Aminopropylsilane (APS) self-assembled monolayers were formed on GaN and glass surfaces from amino-propyldiethoxymethylsilane (APDEMS) in a toluene solution in accordance with protocols published elsewhere [Sch2008, Bau2005]. APDEMS molecules bind to the substrate and NH_2 terminated monolayers were covalently bound the GaN surface, due to its hydroxyl termination, as illustrated in figure 2.11 [Sch2008]. Samples were stored in a light shielded vacuum chamber and used for experiments within 24 h of functionalization. Monolayer quality was assessed prior to use by static water contact angle measurements.

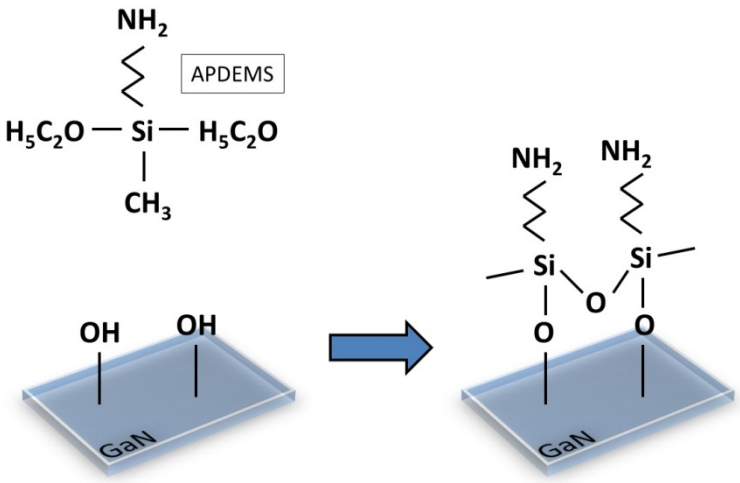

Figure 2.11: Schematic illustration of the binding of an APDEMS molecule to the hydroxyl terminated GaN surface. NH_2 terminated monolayers were covalently bound to the surface.

3 X-ray radiation response of single GaN thin film layers

This chapter shows the radiation response of single GaN thin film layers, operated as photoconductors with ohmic contacts. The device resistance is altered in an external radiation field. In the following sections device characteristics, relevant for dosimetry purposes, such as kerma rate dependence, energy dependence, angular dependence or electrode/2DEG geometry will be discussed.

Some experiments in the following chapter were performed with a 2DEG structure on the GaN layers. Devices with completely etched 2DEG channels, such that only the underlying GaN-layers contribute to conduction, show qualitatively similar x-ray sensing characteristics. **Thus, the x-ray sensitivity is enabled by photoconductivity of the approximately 2.5 µm thick GaN-layer and does not require the presence of an AlGaN/GaN heterointerface.** Due to the light and temperature sensitivities of the devices, all measurements were performed with careful exclusion of stray light and at room temperature. Although GaN layer samples do not have a gate and do not work as transistors, the nomenclature is retained and a current through the device is termed the "source drain current I_{SD}". Figure 3.1 illustrates a direct comparison between the response of a GaN layer sample (a) and a sample with an additional 500 µm wide heterointerface (HEMT) on the surface (b). Although the total current through the sample is increased by the presence of a 2DEG and the relative response scales, the overall sensing characteristics are preserved by the heterostructure. A sample with a heterostructure, but without defined channel etching is shown in figure 3 (c). Since side effects next to the electrical contacts are dominating, a stable measurement is not possible and the device does not saturate with the kerma rate. However, the experimental findings in this section can be more broadly applied to thin films of GaN, regardless of the presence of a 2DEG HEMT structure.

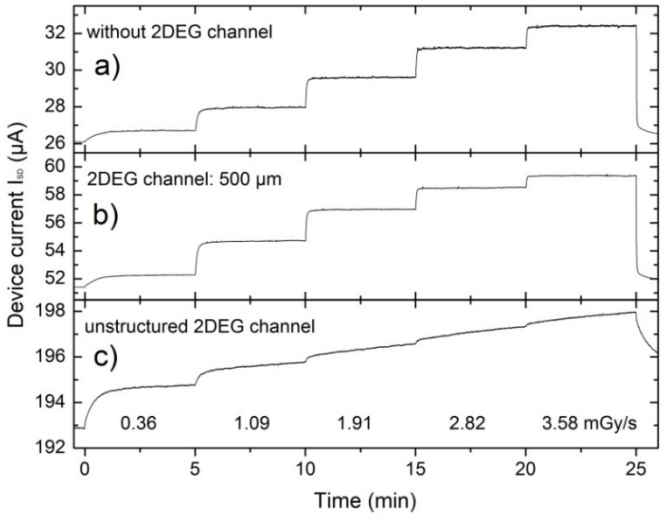

Figure 3.1: Direct comparison of the device response of (**a**) a GaN thin film layer without a 2DEG channel, (**b**) a defined 2DEG channel with a width of 500 µm, and (**c**) a HEMT wafer with a 2DEG but without a defined mesa structure. While the defined HEMT channel just increases the base current, but maintains the qualitative x-ray response compared to the buffer layer structure, the unstructured wafer is dominated by an unstable signal.

By using different GaN samples, it is possible that parameters such as baseline current or relative response are altered but qualitative results presented in this chapter are observed for all GaN buffer layer samples used. A detailed evaluation of the effect of contact geometry and HEMT channel width is given in chapter 3.6.

Typically a Schottky-barrier with a rectifying and high charge transfer resistance is formed at the interface of a metal and a semiconductor. It is possible to achieve ohmic contacts by doping, the right choice of metals and the annealing temperature. By adjusting these parameters, it is possible to form ohmic contacts with a low resistivity and nonrectifying characteristics, in contrast to Schottky contacts. At high temperatures, the metal reacts with the semiconductor material. Annealing of the contact electrodes in a vacuum chamber is necessary to prevent degradation of the 2DEG. The annealing temperature strongly influences the ohmic character of the contacts. Figure 3.2 shows the contact characteristic of a GaN sample annealed at a temperature of 650°C for 10 min and another GaN sample annealed 30 s at 850°C followed by 90 s annealing at 750°C. The linear behavior, as well as the increase of conductivity is clearly observable. All samples used in this work were prepared with the parameters described above for ohmic contact annealing.

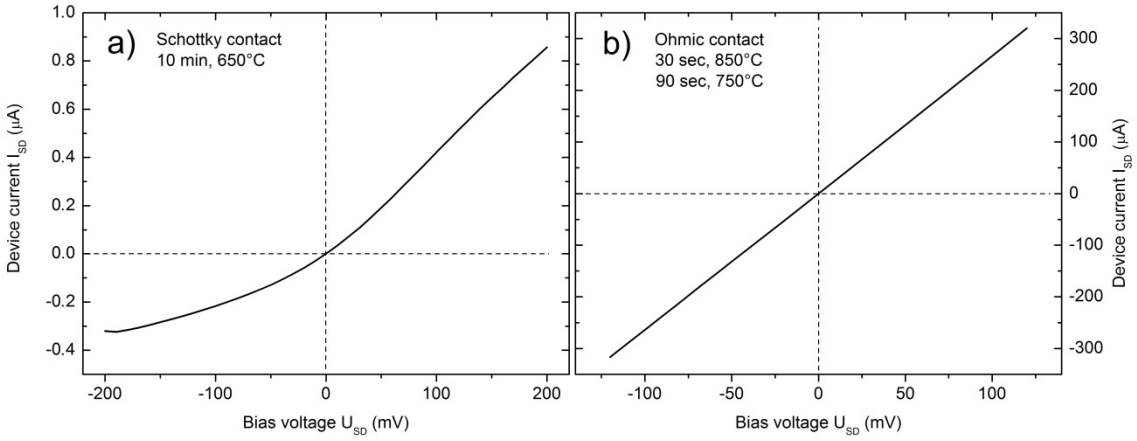

Figure 3.2: Evaluation of contact annealing. (**a**) shows a characteristic device for Ti/Al contacts annealed at a temperature of 650°C while (**b**) shows a characteristic device for contacts annealed at >800°C. The sample in (**a**) exhibits a behavior which is typical for a Schottky barrier: the device current is not linear with the bias voltage and the contacts have a very high resistance. The sample in (**b**) shows a typical ohmic behavior: a linear current with applied bias and a low contact resistance.

In contrast to most established semiconductor x-ray detectors, in which photo-excited electron-hole pairs are separated and collected via an internal space charge region, these devices are operated without intentional formation of a depletion layer. Here, the photo-currents of GaN detectors are monitored with application of a small (<120 mV) dc bias between two ohmic contacts [Hof2010, Hof2011, Fu2011]. Although space charge regions are present due to surface band bending, interfacial band alignment, and extended defects, the measured current primarily passes parallel to, rather than through, such depletion regions.

Illumination leads to non-equilibrium free carrier concentrations which reduce the total volume of the depletion regions and, in turn, increase the effective volume of the material through which carriers can be transported; that is, both the conductivity and the conductance are increased. As a consequence, the photocurrent response is not directly limited by the direct conversion of absorbed energy to free carriers, and the devices can function as x-ray sensitive detectors with significant internal amplification, as described theoretically in section 1.4. Figure 3.3 shows the output characteristic, I_{SD} as a function of U_{SD}, for a TG1592 sample with 500 µm wide contact pads (detailed wafer structure can be found in chapter 2.1). Due to the use of ohmic contacts, the device shows a linear behavior. Although radiation shifts the source-drain current I_{SD}, the linearity is preserved. Therefore, the radiation response scales linearly with the bias voltage of the devices. This fact is also predicted by the gain model discussed in chapter 1.4.

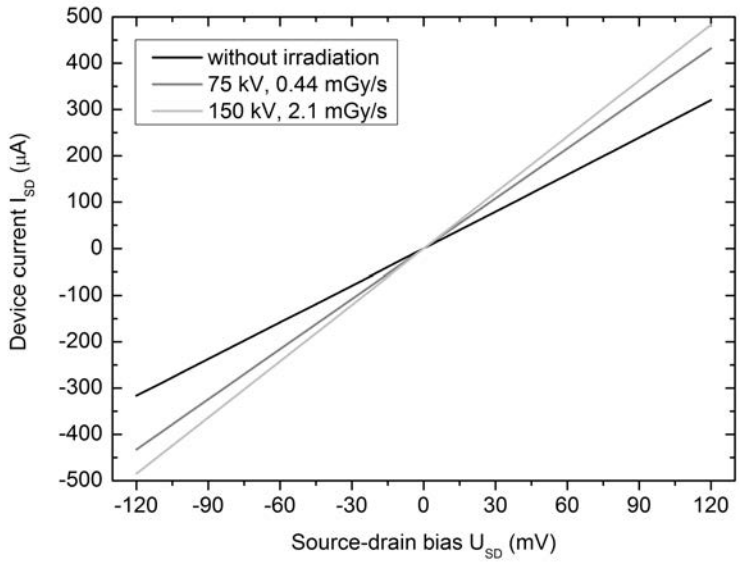

Figure 3.3: Output characteristic of a GaN-HEMT device. The transistor shows a linear behavior in the given bias-regime due to ohmic contacts. The relative device response ΔI_{SD} scales linearly with the magnitude of the applied potential U_{SD}.

3.1 Kerma rate dependence

In order to confirm the stability and reproducibility of device performance during and after x-ray irradiation, multiple series of dose-rate dependent transport measurements were performed. The result of a 150 kV pulsed x-ray irradiation series is shown in figure 3.4. The source-drain current I_{SD} changes with the air kerma rate at a fixed source-drain potential U_{SD} of 120 mV. The sample consists of a GaN buffer layer and a 400 µm wide HEMT channel. As mentioned before, the presented device response is produced in the buffer layer, while the HEMT channel is utilized for another set of experiments and only shifts the base current and/or scales the device response. X-ray intensities were changed by adjusting the acceleration current of the x-ray tube. Irradiation was performed with pulses of 1 min duration at 5 min intervals. A monotonic increase of the source-drain current with x-ray dose-rate due to generation of photo-excited carriers is observed. These measurements were performed without gating and the residual current in darkness is primarily a consequence of conduction through the open HEMT channel. There are very slow transient current decay times observable which are in the range of several hours. Due to this fact, it is difficult to define a baseline current. Nevertheless, one of the features of the devices is that the absolute signal reading directly correlates to the air kerma rate and is independent of relative measurements to the baseline. This fact will be discussed in detail in chapter 3.6.

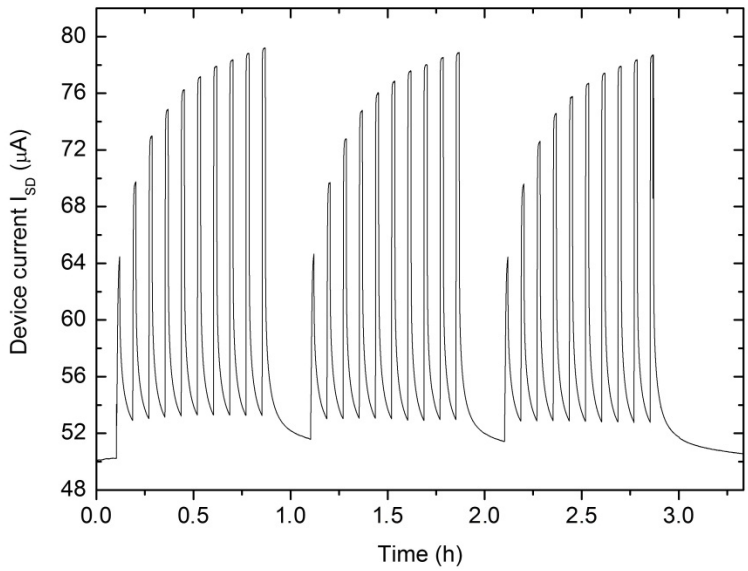

Figure 3.4: Radiation response of a GaN thin film layer, biased with U_{SD} = 120 mV for different air kerma rates between 0.2 mGy/s and 12 mGy/s. The plot shows the temporal progression of the source drain current I_{SD} for 1 min irradiations at 5 min intervals with 150 kV x-rays. The corresponding values for the kerma rates can be found in figure 3.5.

The absolute sensor current after 1 min irradiation plotted versus the air kerma rates is shown in figure 3.5. Due to slow drifts the device is not completely saturated after an irradiation time of 1 min. Therefore the plots in figure 3.5 do not display a general characteristic of the GaN devices, since the device current response values strongly depend on irradiation time. The intention of presenting these plots is to show the reproducibility of the measurements. The relative alteration of the device response due to transients is in the lower percentage regime and the rise times decrease exponentially with the kerma rates. These temporal effects will be discussed in detail in chapter 3.2. Nevertheless, comparison of results from a repetition of the dose series yields excellent reproducibility without any noticeable permanent performance alteration after a total dose of 60 Gy. Small deviations between the plots in figure 3.5 are due to slow temperature drifts of the devices since all measurements are performed at room temperature without temperature control. As evidenced by the dark current in figure 3.4, the sensors have a certain residual signal in the absence of irradiation because the measurements were performed without gating of the transistors. Consequently, each device is in its on-state and conduction through the channel occurs even in the absence of illumination. Nevertheless, the large signal to noise ratio (S/N), which is in the range of 1×10^6 during irradiation under the current experimental conditions and is nearly independent of the air kerma rate, along with the strong photoconductive response, allow effective measurement down to the sub-µG/s regime. Importantly, the stated S/N is not a fundamental limit for the devices since no precautions were taken to minimize outside sources of noise. Detailed evaluation of the noise characteristics of these devices is beyond the scope of the present work and can be found elsewhere [Eas2002, Gar2000]. Although optimization for noise minimization is possible, the results presented in figure 3.4 serve to illustrate that the device sensitivity is high enough that small changes in air kerma rate can be readily observed under typical operational conditions, without shielding or specialized measurement configurations.

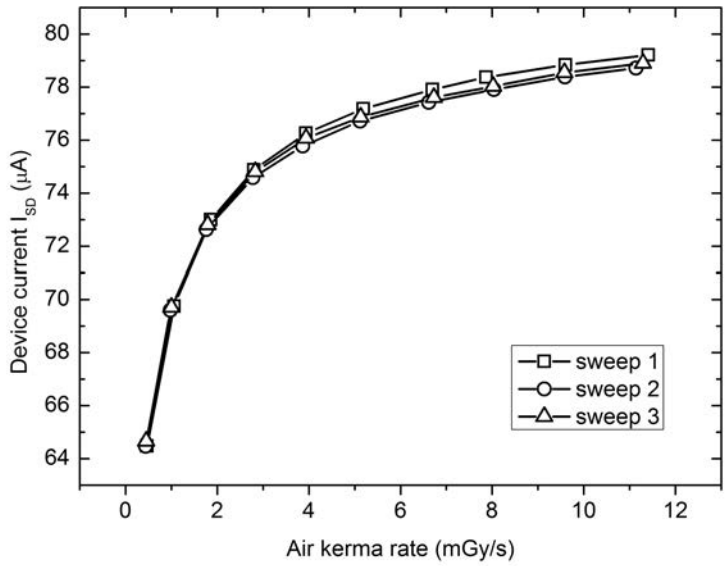

Figure 3.5: Air kerma rate-response curve for the measurement shown in figure 3.4. The curve illustrates the absolute device current after a pre-irradiation of 1 min as a function of the air kerma rate.

Measurements in the low dose regime, at air kerma rates below 0.1 mGy/s, are shown in figure 3.6. For these dose rates, the absolute device current I_{SD} shows a linear behavior and is proportional to the air kerma rate. The detection limit is primarily determined by the slow current transients at these rates. Therefore, absolute signal readings are evaluated after irradiation pulses of 5 min during continuous irradiation with an acceleration voltage of 150 kV.

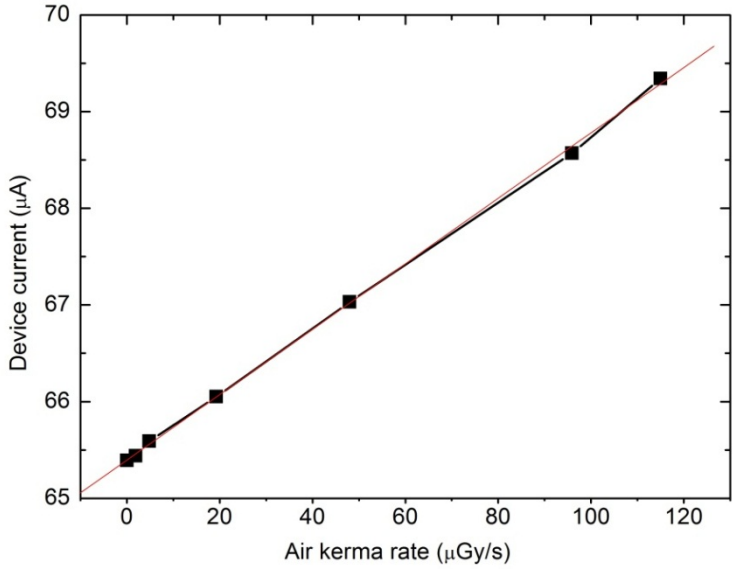

Figure 3.6: Air kerma rate-response curve for exposures to the low kerma rate regime (< 0.2 mGy/s). In contrast to the device response for higher rates, the measurement shows a linear response characteristic. Irradiations were performed with 18 kV x-rays.

In this work, gallium nitride thin films were developed and evaluated in order to act as x-ray radiation detectors. In recent years, gallium nitride based devices have been proposed and tested for x-ray detection, but only limited systematic characterization has, thus far, been performed [Dub2008, Dub2009]. The published results have shown that the absorption of GaN is too low above 20 keV to use it for x-ray detection. In contrast to these publications, the results in this work show that GaN is an excellent candidate for radiation detection purposes and works well, even at energies above 20 keV. This discrepancy has two reasons:

1) Material production for wide-bandgap semiconductors suffered from material defects in the past decades but improved dramatically within recent years. As manufacturing processes for these materials became increasingly sophisticated, materials could be produced with fewer impurity traps and electron mobility could increase. For a photoconductor, the gain is proportional to the electron mobility. This fact will be discussed in detail in chapter 3.6 (see equation 3.4 and 3.5).

2) The operational principle of the GaN devices presented in this work is fundamentally different from most conventional semiconductor x-ray detectors in that the sensor

response is not solely governed by extraction of photo-generated carriers. Rather, the large photoconductive gain arising from modulation of the conductive volume of the device with illumination intensity is exploited to achieve significant amplification. Such a mechanism has been well characterized and modeled to describe the large conductive gains observed for the case of GaN ultraviolet photodetectors [Mun1997, Gar1998], but has not been exploited for x-ray dosimetry. In contrast to most established semiconductor x-ray detectors, in which photo-excited electron-hole pairs are separated and collected via an internal space charge region, these devices are operated without intentional formation of a depletion layer. Here, the photocurrents of GaN detectors are monitored with application of a small (< 120 mV) dc bias between two ohmic contacts. Therefore, the amplification depends strongly on the film thickness, doping, and extended defect concentration, since these parameters define the alteration of the conductive volume under illumination.

An estimation of the photoconductive gain of these devices highlights their extremely large sensitivities compared to those based on direct charge extraction. The ratio of the mass energy-absorption coefficient of gallium, which is the main absorbing material in the detector due to its high Z, to that of air is ~70 for 40 keV x-rays and ~15 for 100 keV x-rays [Hub2004]. The ratio of the mass energy absorption coefficient of nitrogen to that of air is negligible since it is in the range of 0.7 – 1 for the used energies. The sensors exhibit a sensitivity of 0.122 μA/(μGy/s) in the linear regime. Consequently, a total charge of 0.122 C, corresponding to 7.6×10^{17} additional charge carriers, is collected for a 1 Gy (air kerma) irradiation. Estimating that absorption is approximately 50 times greater in the detector material compared to air, and considering the detector volume and the density of gallium nitride of 6.15 g/cm^3, reveals that a dose of 1 Gy to air deposits an energy of 2.15×10^{-6} J into the material. This corresponds to ~18 μeV per charge carrier, compared to the 3.4 eV bandgap of GaN, and demonstrates the huge amplification occurring in the material. The minimum gain, based on this simple calculation, is in the range of 10^5.

3.2 Transient behavior

Transient times play an important role for measurements with GaN buffer layers. Therefore irradiations with different air kerma rates were performed at an acceleration voltage of 150 kV and the off/on characteristics were investigated. Figure 3.7 shows a typical measurement with a C-compensated buffer layer of a HEMT and corresponding values are given in table 3.1, obtained from 10 min irradiations performed at 15 min intervals. The relative response is normalized to the baseline current which was determined before the first irradiation peak. Following initial settling, the devices show very stable signals, with signal drifts of ~1% during 10 min irradiations. The origin of these drifts is not only a device characteristic but also caused by the used x-ray equipment, as illustrated at the end of this chapter in figure 3.9.

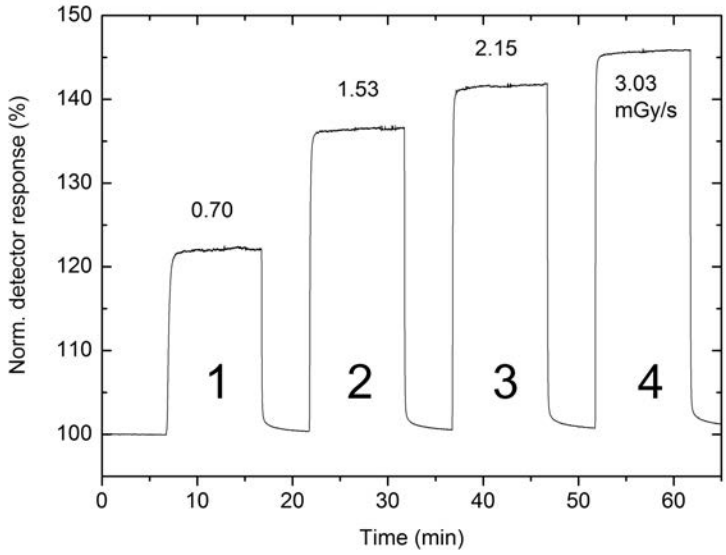

Figure 3.7: Radiation response of a GaN thin film layer to 150 kV x-rays. The measured source-drain current I_{SD} is normalized to the baseline current without radiation. The device is exposed to 10 min irradiation peaks at 15 min intervals.

Pulse	Rate (mGy/s)	Response (%)	Δt_{on} (80%) (s)	Δt_{on} (90%) (s)	Δt_{on} (95%) (s)	Stability (%)
1	0.70	22.0	22.8	33.3	42.6	0.91
2	1.53	36.5	9.7	14.1	20.4	0.82
3	2.15	41.6	6.9	9.7	14.2	0.96
4	3.03	45.6	4.7	7.0	9.9	1.32

Table 3.1: On/off characteristics of the measured devise response shown in figure 3.7. The relative device response is normalized to the baseline without irradiation and Δt_{on} (80%, 90%, 95%) are the times to reach 80%, 90% and 95% of the stable signal level, respectively, following the onset of x-ray irradiation. The stability gives the maximum signal drift during 10 min irradiation following settling.

In-drift times (Δt_{on}) decrease with increasing air kerma rate. Although the 95% off/on settling times are relatively long, the primary response is much faster, as indicated by the 80% and 90% off/on settling times. The correlation between off/on time Δt_{on} and the air kerma rate is shown in figure 3.8. The plots follow an exponential decay with very good agreement ($R^2 > 0.99$). For low dose rates < 0.1 mGy/s, the settling times becomes very long and therefore it is impossible to evaluate off/on characteristics within appropriate irradiation times. Since settling times for low dose rates can be extracted from figure 3.8 by extrapolation, a further characterization of time constants is not necessary. At high dose rates (> 0.2 mGy/s) the off/on times are independent of the x-ray energy since the device response itself is independent of the x-ray energy. This fact will be discussed in detail in chapter 3.4. But for small dose rates, the device responses, and therefore the off/on times, show an energy dependence.

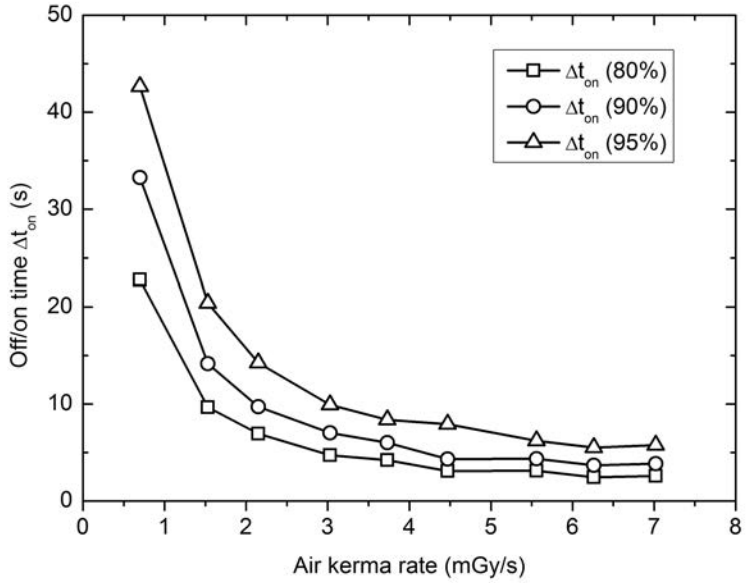

Figure 3.8: Transient times of the sensor signals for 150 kV x-rays at different air kerma rates. The Y-axis represents the time until the sensor signal reaches 80% (90%, 95%) of the saturation level when switching x-rays on. The plots clearly indicate an exponential correlation between kerma rates and drift times of the device.

Evaluating the off/on characteristics focus on the maximum change in dose rate. For many applications, it could be more important how the device tracks small dose rate changes. Once the signal settles, the real-time device response time of the GaN detector is comparable to that of an ionization chamber, as depicted in figure 3.9. The plot shows a comparison of the simultaneous responses of a GaN device and a Dosimentor M4 ionization chamber during a 75 kV irradiation. The GaN signal was directly recorded with a single SourceMeter by applying an 80 mV bias voltage and the signal from the ionization chamber was recorded at the same sampling rate. The strongly correlated responses are indicative of x-ray dose variations over time due to source and environmental fluctuations. While the rise and fall times for the GaN device are somewhat longer than for the ionization chamber, the overall performance is similar. However, it is important to emphasize that the active device volume of the ionization

chamber, which is in the cm^3 regime, is about 1×10^5 times larger than the 7×10^{-6} cm^3 active volume of the GaN device. The small variations in air kerma rate are due to fluctuations in the x-ray tube.

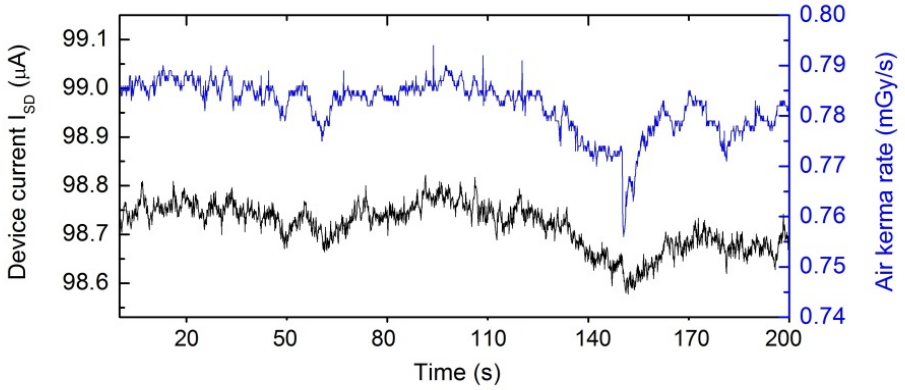

Figure 3.9: Direct comparison of the measurement signal of an ionization chamber (PTW, Dosimentor M4) and the source drain current I_{SD} of a GaN thin layer device. It is clearly observable that both signals have the same progression, although the volume of the GaN sensor is several orders of magnitude smaller than the volume of the ionization chamber.

3.3 Total dose response

In contrast to other dosimeters, like MOSFET detectors or retrospective read-out TLDs, the signal reading of a GaN buffer detector gives direct information about the dose rate and not only the total dose. Since the dose is the integrated dose rate over a time interval t-t_0, it is easy to provide information about the air kerma with the GaN detectors.

$$D = \int_{t_0}^{t} \dot{D} dt \ \ (mGy) \tag{3.1}$$

Since the signal reading I_{SD} of the GaN buffer detectors directly correlates with the dose rate $\dot{D}$ the signal integral R over time directly correlates with the dose D after subtracting the integral of the baseline current I_0.

$$R = \int_{t_0}^{t} I_{SD} dt - \int_{t_0}^{t} I_0 dt \ \ (As) \propto D \ (mGy) \tag{3.2}$$

Figure 3.10 shows the integrated dose for 10 min irradiations. In (a) 18 kV x-rays and low air kerma rates are used while for the irradiations in (b) the detector was exposed to 150 kV x-rays at relatively high rates.

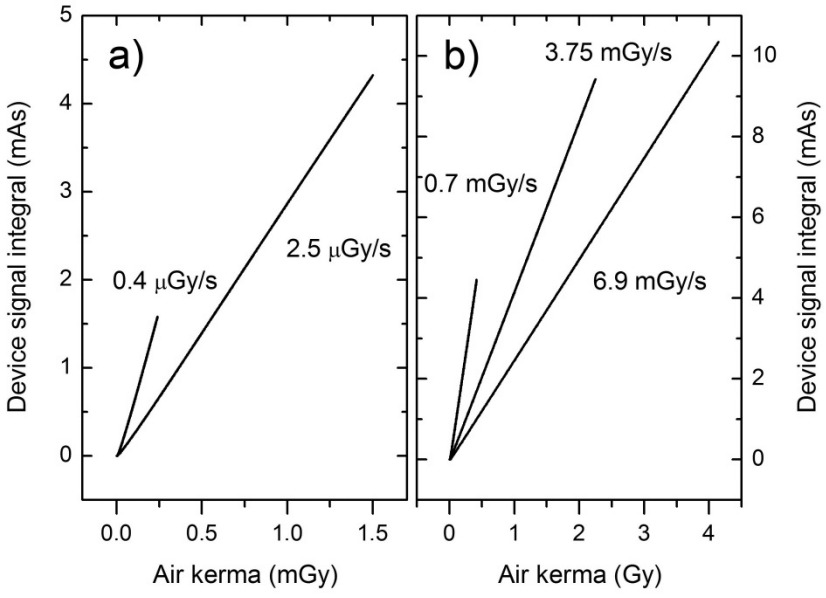

Figure 3.10: Time integral of the transistor signal shows a linear correlation with the total dose in air. The measurements in the low dose range (**a**) were performed with 18 kV x-rays and the high dose measurements (**b**) with 150 kV x-rays. Transistors were irradiated for 10 min at given dose rates.

The unit (As) represents the "electrical charge" which is usually given in the unit Coulomb (C). In contrast to the measurement principle of an ionization chamber where charges are collected in a capacitor, the GaN detectors require a subtraction of the baseline current, which can be done online during the measurement. Nevertheless, in this work the unit (As) is used for the integrated dose of the GaN detectors to avoid misleading analogies with the measurement principle of an ionization chamber.

Above an air kerma rate of about 0.2 mGy/s, the GaN buffer devices show nearly no dependence on the x-ray energy. Therefore, the signal integral directly correlates to the air kerma. At lower dose rates, the measurements must be calibrated to the x-ray energy. For example, the measurements in figure 3.10 (b) would be unvaried by an irradiation with a different x-ray energy at the same dose rate while the plots in figure 3.10 (a) would change their slopes. These effects will be discussed in detail in chapter 3.4.

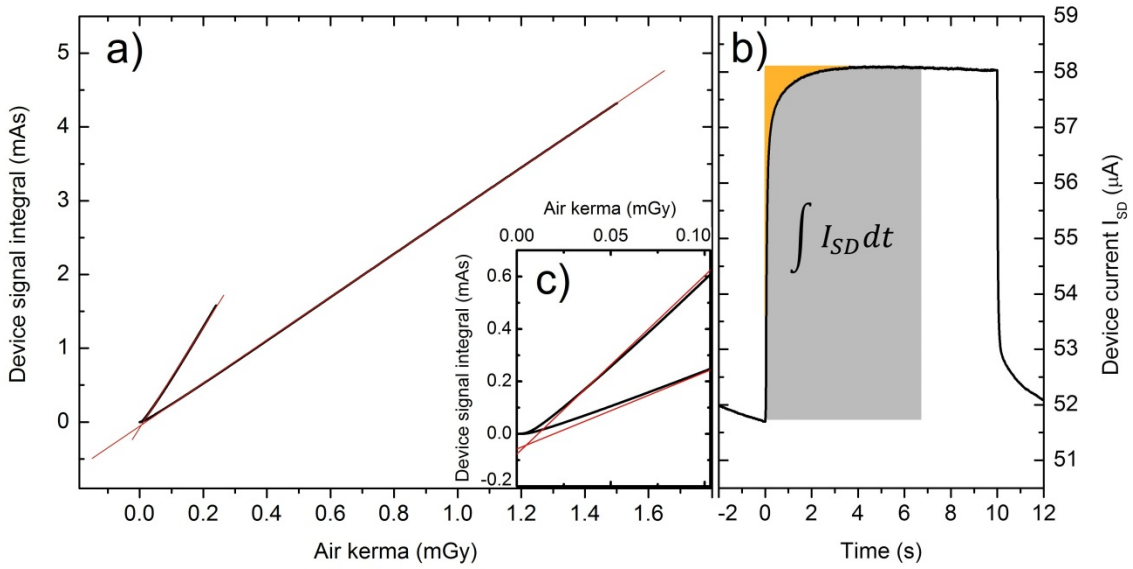

Figure 3.11: (**a**) time integral of the transistor signal given in (**b**). The inset (**c**) shows the in-going drift of the signal at the beginning of the pulse, but linear behavior is observed down to ~10 µGy. The measurements were performed with 18 kV x-rays and transistors were irradiated for 10 min.

Not only the x-ray energy alters the measurement response, but the in-drift times of the devices also affect the total dose calculations. Irradiation of a GaN buffer layer with an 18 kV irradiation pulse at an air kerma rate of 1.6 µGy/s is shown in figure 3.11 (b). As already discussed, the area under the curve correlates with the dose but, due to the in-drift time, a discrepancy arises, which corresponds to the area indicated with orange color. Evaluation of the time integral in figure 3.11 (a) and (c) shows that the indrift discrepancy of the signal causes a non-linearity of the integrals. The y-axis intercept of the linear fits, indicated with red color in figure 3.11 (a) and (c), directly correlates with the orange area in figure 3.11 (b) and represents the error of the measurement caused by the indrifts since the plots need to cross the origin of coordinates. The error of the 0.4 µGy/s irradiation is -0.077 mAs and the error of

the 2.5 µGy/s irradiation is -0.057 mAs. Compared to the whole 10 min irradiation, the relative errors are only 4.88×10^{-4} % (0.4 µGy/s) and 1.32×10^{-4} % (2.5 µGy/s), respectively. At this point, it is important to emphasize that since the detector signal I_{SD} stays at a constant level after the indrift, the relative error decreases with the irradiation time. For short irradiations, the error caused by the drift time becomes significantly higher. For example, a 10 s irradiation with a dose rate of 0.4 µGy/s results in a total dose of 4 µGy. The fit of the 0.4 µGy/s irradiation yields a linear correlation between signal reading and kerma of 0.0068 mAs/µGy. Therefore, a 10 s irradiation should give a value of 0.0272 mAs, while the real measurement yields a value of 0.0023 mAs due to the non-linearity at the start of the measurement. Therefore, the error is over 90% for a 10 s irradiation. This example should demonstrate that the devices are highly sensitive for x-ray dosimetry. Nevertheless, the sensors need to be adapted to the used application.

3.4 Energy dependence

Investigation of the influence of the energy distribution on signal readings is a particularly important aspect of x-ray detection. Dosimeters, such as ion chambers, are calibrated against calorimeters [But2003], whereas absolute dosimetry is a technique that yields information directly about absorbed dose in units of grey (energy absorbed per unit mass). Measurements can be corrupted by detector materials which exhibit strongly energy-dependent responses. Usually the absorbed x-ray energy is transformed into a measurement signal. Since the absorption is an intrinsic material property, there is only the possibility to alter the energy related absorption via external environmental methods, such as the utilization of compensation filters.

3.4.1 Absorption

It was recently reported that GaN should be a poor material for x-ray detection above energies of 20 keV since the absorption in the material becomes very low [Dub2008]. Figure 3.12 shows the calculated absorption of a GaN layer with a thickness of 3.5 µm and a sapphire layer with a thickness of 330 µm, based on the attenuation coefficients of Henke *et al.* [Hen1993]. The absorption of a 3.5 µm thick GaN layer is about 2% for a 40 kV Bremsstrahlung irradiation, which corresponds to an average photon energy in the range of 30 keV. By operating thin films as active devices with a very high gain, this small absorption is enough to utilize the GaN buffer sensors for highly sensitive dosimeters.

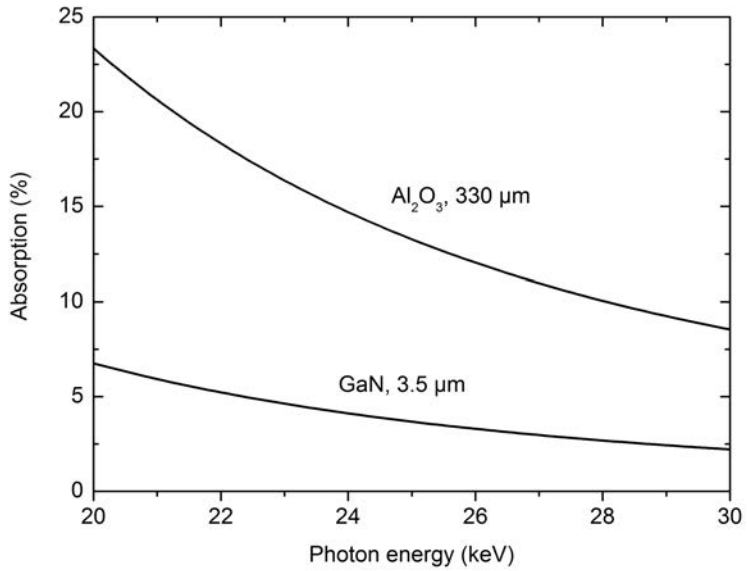

Figure 3.12: Calculation of the percental absorption in a 330 µm thick sapphire film and a 3.5 µm thick GaN film. The calculation is based on the attenuation coefficients of Henke *et al.*

Real absorption measurements show very good agreement with the calculated values. In figure 3.13 the relative absorption of semiconductor samples (see table 3.2) relative to air for a 40 kV and a 150 kV irradiation is illustrated. For these measurements the samples were located between the beam exit and a TM 23361 ionization chamber (PTW, Freiburg, Germany) in such a way that the entire beam was incident on the semiconductor samples. The relation of collected charge from the ionization chamber integrated over 60 s irradiation time with and without the sample gives the relative absorption. The measured charges are translated into 'air kerma' by using appropriate calibration factors and corrections for radiation quality, ambient pressure, and temperature. Filtration for ISO narrow series radiation qualities are given in table 2.2. It has to be taken into account that the ionization chamber is calibrated to specific radiation quality in air, while the absorbing material may alter the energy spectrum of the x-ray beam. Therefore, a systematic error is introduced to the absorption measurements. However, since experiments have shown that absorption is very low for the used samples, the change in radiation quality due to the additional absorber can be considered negligible.

Wafer name	Substrate (µm)	GaN-film (µm)	Compensation species
Sapphire	330	-	-
TG1797	330	3.1	-
TG1800	330	3.4	C

Table 3.2: Thickness and defect compensation of GaN and sapphire wafers used for the absorption measurements.

For 40 kV irradiation, the mean photon energy is in the range of 30 keV. The measured change in absorption of ~8% for the sapphire substrate and ~10% for the substrate with a GaN layer (figure 3.13) fits very well to the calculated values for 30 keV photons given in figure 3.12. While absorption is independent of the air kerma rate, an irradiation with 150 kV x-rays decreases the relative absorption below 2% and discrimination between the wafer samples becomes impossible.

A full absorption spectrum for the TG1800 wafer at different acceleration voltages is shown in figure 3.14. Each measurement was performed with a tube current of 1, 5 and 10 mA. Again, the absorption is independent of the acceleration current and consequently independent of the dose rate. The data show a high gradient for low energies and a saturating character above an acceleration voltage of 80 kV, which leads to the energy dependent device response, which will be discussed in chapter 3.4.2.

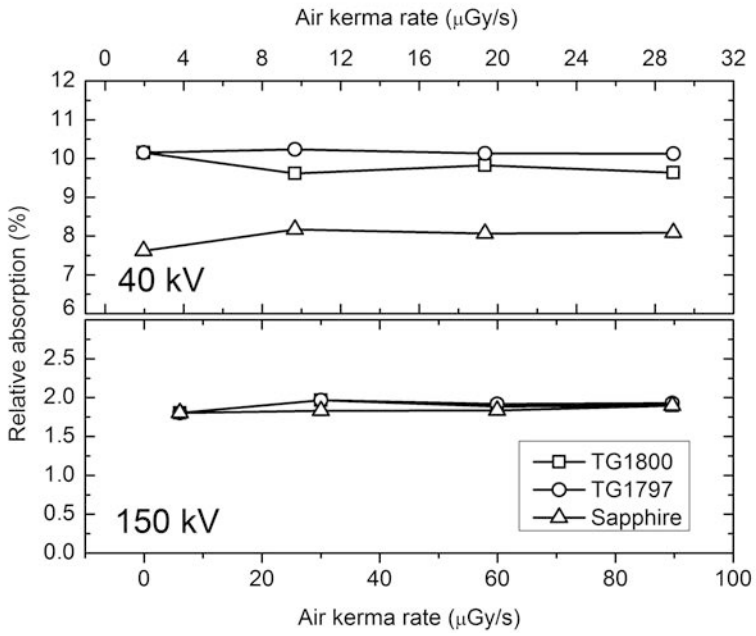

Figure 3.13: Measured relative absorption in GaN/sapphire wafers and a bulk sapphire substrate. The sapphire substrate has a thickness of 330µm. Both GaN wafers consist of a sapphire substrate and a GaN layer with a thickness of 3.4 µm (wafer TG1800) or a thickness of 3.1 µm (wafer TG1797). Relative absorption is calculated by the ratio of the recorded air kerma rate with and without a wafer in the x-ray beam. Energy spectrum shifts of the x-rays due to the absorber material inside the beam are assumed to be negligible for such small values.

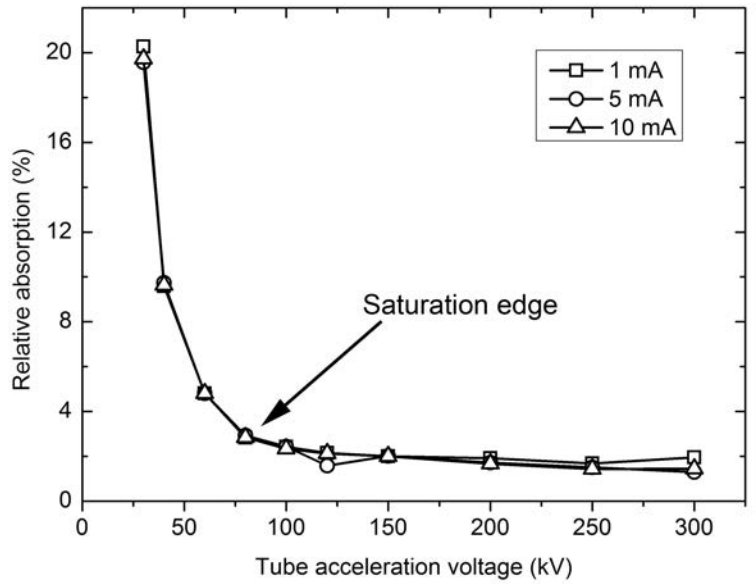

Figure 3.14: Measured relative absorption of the TG1800 wafer as a function of the x-ray acceleration voltage. A change of the tube current, which results in a change of the air kerma rate, does not change the relative absorption.

3.4.2 X-ray energy dependent response

The energy response of GaN thin film devices strongly depends on the air kerma rate to which the structures are exposed. Since the primary device response is not governed by direct extraction of photo-generated charge, but rather by internal photoconductive amplification, a simple correlation between the absorbed energy and the output response does not hold [Gar1998]. Higher dose rates decrease the photoconductive gain due to saturation of photovoltages, but increase the absolute signal. Thus, these competing effects lead to a lower than expected energy dependence in the non-linear response regime above dose rates of ~0.2 mGy/s. Figure 3.15 shows a measurement of 4 GaN devices simultaneously. For multiple sensor measurements the voltage across shunt resistors is measured instead of the source-drain current I_{SD}. Values are recorded by integrating and averaging the signal readings over a period of 16 s after a pre-irradiation of 60 s. The acceleration voltage and current are changed in such a way that the resulting air kerma rate is kept at a constant level of 0.46 mGy/s. Although the NIST database reports a significant change of the energy mass absorption coefficient of gallium in this regime [Hub2004], the observed device response does not change by more than ±2% for all four devices when the acceleration voltage is changed from 50 kV to 75 kV with equal air kerma rates.

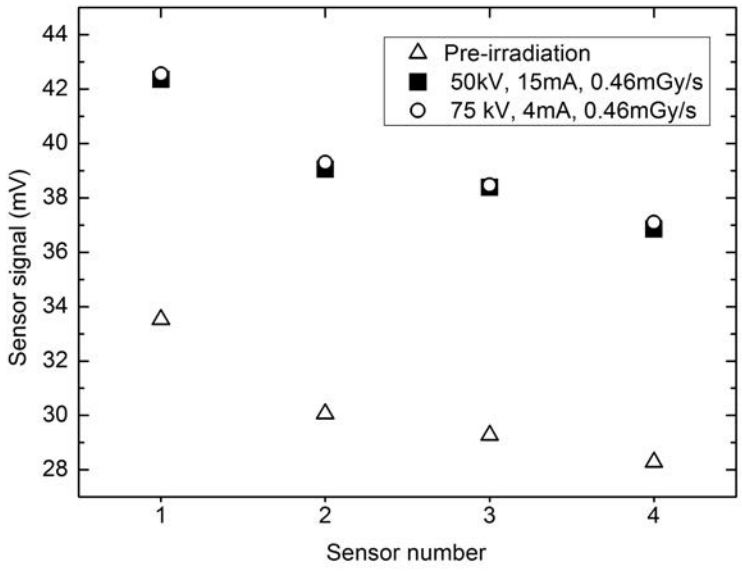

Figure 3.15: Absolute sensor signal of 4 simultaneously irradiated GaN sensors. The unit of the signal is mV since the devices are measured via shunt resistors. This measurement reveals that a change of the x-ray acceleration voltage from 50 kV to 75 kV, which results in an absorption change of a factor of ~2, produce the same signal response. The device works independently of the x-ray energy.

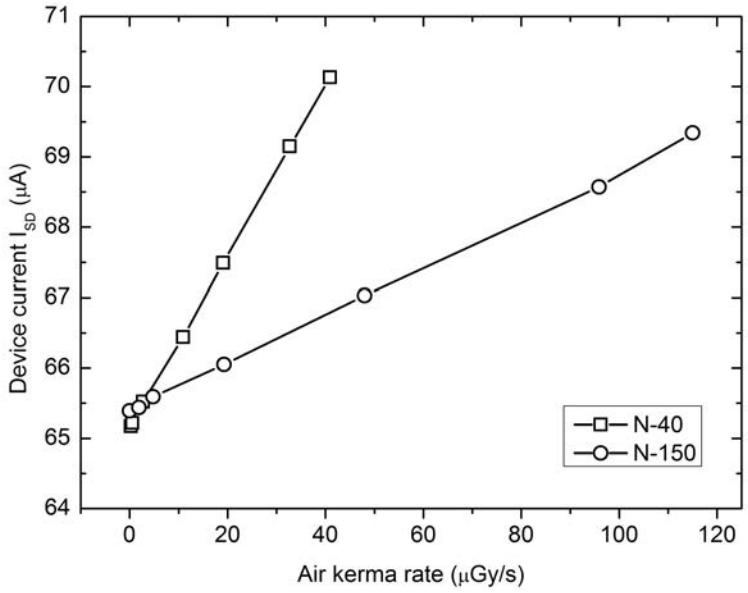

Figure 3.16: Absolute sensor signal for a calibrated 40 kV (N-40) and 150 kV (N-150) irradiation. In contrast to the measurements in the high dose rate regime (> 0.2 mGy/s) the measurement shows a strong dependence on x-ray energy.

For irradiations in the low rate regime below about 0.2 mGy/s absolute dosimetry becomes impossible and the sensors show a higher dependence on x-ray energy. Figure 3.16 illustrates the device response after a pre-irradiation of 5 min for each kerma rate. The response strongly correlates to the photon energy spectrum. The device sensitivity changes from 0.122 μA/(μGy/s) for the 40 kV irradiation to 0.034 μA/(μGy/s) for the 150 kV irradiation due to a change in absorption. In these kerma rate regimes, an energy calibration of the GaN buffer layer devices is required.

A possible explanation for observed effects could be that for low dose rates the photo-voltage at the device surface does not saturate. Therefore the device response reflects the x-ray absorption spectrum.

3.5 Incident angle dependence

In order to determine the angular dependence of the sensor response, which is important for defining the geometric range over which the devices may be operated without need for additional calibration, a standard HEMT device was irradiated with 140 kV x-rays at different photon incidence angles. The x-ray tube was rotated around the device in 15° steps, starting at a photon incidence angle (ρ) of 0° relative to the surface normal, as shown in the inset of figure 3.17. The irradiation was performed with pulses of 3 min duration at 6 min intervals and the x-ray tube was rotated during the irradiation pauses. The distance error caused by rotation of the tube exit in relation to the sample surface was determined to have a maximum value of 2.6%. Figure 3.17 shows two measurement series: with pitch parallel and pitch perpendicular to the long edge of the sensors, as defined in the schematic inset of figure 3.17. For incident angles less than 60°, the measured signal remains constant, with standard deviations of 0.20% for parallel pitch (θ = 0°) and 0.27% for perpendicular pitch (θ = 90°) irradiations. Although the sensors have a thin detection volume and the incident photon flux decreases at higher incidence angles, the path length through the volume increases, as illustrated in figure 3.18. The surface area A_0 and the thickness of the active sensor material d_0 define the sensor volume V, which is penetrated by photons, independently of the photon incidence angle ρ, as described by

$$V(\rho) = A(\rho)d(\rho) = A_0 cos(\rho) \times \frac{d_0}{\cos(\rho)} = A_0 d_0 \tag{3.3}$$

Thus, the volumetric response remains constant and the geometric effects cancel out one another. This is possible since absorption due to the sensor material is negligible for such thin detection volumes.

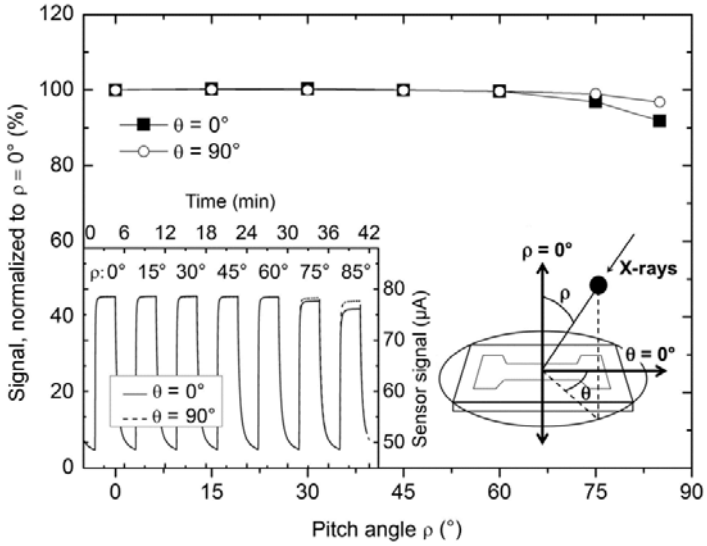

Figure 3.17: Evaluation of relative response as a function of incidence angle for 140 kV x-rays. Measurements were performed both with the pitch parallel to the long side of the sensor and pitch perpendicular to the long side of the sensor, as depicted in the schematic diagram. The inset plot shows the actual device response during the measurement.

Above an incident angle of 60° relative to the surface normal, a slight decrease of the signal is observed and the responses for the parallel and perpendicular pitch irradiations diverge. Interpolation of the readings shows a statistically significant signal decrease of up to 2.6% for the pitch perpendicular measurement and of up to 8.5% for the pitch parallel measurement at irradiation angles of greater than ~80°.

The dependence of the measurement signal on high pitch angles (ρ > 60°) relative to the surface normal is most likely a consequence of increased shielding of the film structure by the contacts. Nevertheless, these results indicate that the devices are insensitive to the angle of irradiation over a very wide range of geometries. Thus, the devices may be used in diverse configurations without the need for additional calibration.

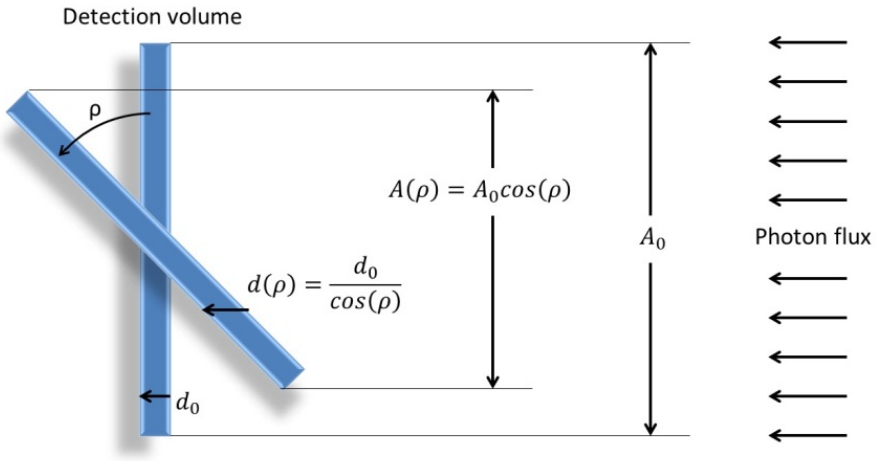

Figure 3.18: Angular dependence of the active sensor volume penetrated by x-rays. A rotated detection area A_0 is exposed to fewer photons but the path length d_0 increases with the angle ρ. Both geometrical effects cancel each other out.

3.6 Impact of electrode and 2DEG channel geometry on buffer response

It was recently reported that both the contact and 2DEG geometries have severe impacts on HEMT device characteristics [Pod2010]. Besides this fact, experiments have shown that, although a HEMT channel on the GaN buffer layer samples does not alter the absolute x-ray sensitivity of the buffer layer, it changes the signal stability with time of the sensors. To test the influence of both the contact pad and HEMT channel geometries on the buffer layer response, multiple sensor device structures on single wafer samples were developed and produced. The sensor types, as well as the geometry of the devices, are given in table 3.3 and are illustrated in figure 3.19.

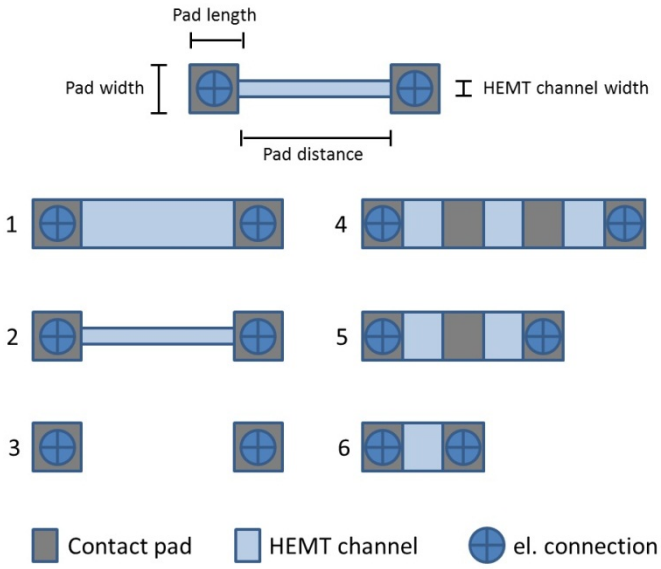

Figure 3.19: Electrode and HEMT channel geometries used for irradiation experiments to evaluate its influence to the device response. The corresponding dimensions are given in table 3.3.

Structure	Pad length (µm)	Pad width (µm)	Pad distance (µm)	2DEG width (µm)
1	500	500	1800	500
2	500	500	1800	30
3	500	500	1800	-
4	400	500	2000	500
5	400	500	1200	500
6	400	500	400	500
IDT	2000	50	50	2350

Table 3.3: Dimensions of the HEMT and contact pad structures shown in figure 3.18.

Beside the structures in figure 3.19, an interdigital transducer structure (IDT) was evaluated, consisting of a total area of 2.8 x 2.35 mm^2 with 24 contact pads, each having a width of 50 µm separated by a distance of 50 µm. The irradiation protocol for evaluating the radiation response of the different structures is summarized in table 3.4. The protocol consists of a 10 min pre-irradiation to bring the sample to a comparable excited state, followed by irradiations with different air kerma rates at 5 min intervals. This protocol enables a detailed comparison of in-drifts, out-drifts and radiation responses for the different structures. Every sample was exposed to four irradiation series, two at a low kerma rate with the Philips MG320 at 40 kV and 150 kV and two at a high kerma rate with the TR300f at 75 kV and 150 kV. Table 3.4 gives the setting of the x-ray tubes, and the corresponding air kerma rates are given in the plots. These settings were chosen to cover a wide range of dose rates. All GaN samples were exposed to the same irradiation procedures to preserve the comparability of the device responses.

Some evaluated structures show poor radiation sensitivity and irradiations at 5 min intervals are too short for such devices to reach saturation level. Nevertheless, the intention of these experiments is to give a qualitative impression of x-ray detection capabilities and not to produce calibration curves. These experiments are carried out to test the structures for real dosimetry applications and provide comparability. Drift times > 5 min are not appropriate for such measurements and were not investigated.

Since transition times play an important role for these experiments, the complete time dependent measurements are always shown in this chapter, which give a good impression for sensing capabilities. The device response is evaluated by plotting the signal reading after the pre-irradiation pulses, independent of the signal reaches saturation level or not. Therefore, the graphs do not only show the dose rate response curves but also give the temporal progression of the measurement signal. The devices are supplied with a 120 mV bias voltage, unless otherwise noted.

Time (s)	MG320 N-40	MG320 N-150	TR300f 75 kV	TR300f 150 kV
0	-	-	-	-
300	10 mA	10 mA	10 mA	10 mA
900	-	-	-	-
1500	0.5 mA	0.5 mA	2 mA	2 mA
1800	2 mA	2 mA	6 mA	6 mA
2100	5 mA	5 mA	10 mA	10 mA
2400	10 mA	10 mA	14 mA	14 mA
2700	15 mA	15 mA	18 mA	18 mA
> 3000	-	-	-	-

Table 3.4: Irradiation protocols for the device characterizations. The tube acceleration currents are chosen to cover a broad x-ray intensity range.

A typical irradiation with 150 kV x-rays is shown in figure 3.20, according to the protocol given in table 3.3 with a GaN thin film without a HEMT (Structure 3, Wafer TG1592). Although the baseline does not reach its initial level during the irradiation pause from 15 – 25 min the device current reaches exactly the same level for each 2.2 mGy/s irradiation. This is an effect that was observed for all experiments and leads to one of the main conclusions regarding x-ray dosimetry with GaN films**: The sensor signal correlates to the air kerma rate independently of the pre-irradiation baseline current.** Therefore, a shift of the baseline current caused by a pre-irradiation plays no role for absolute dose rate measurements but has only effects for transient time alterations.

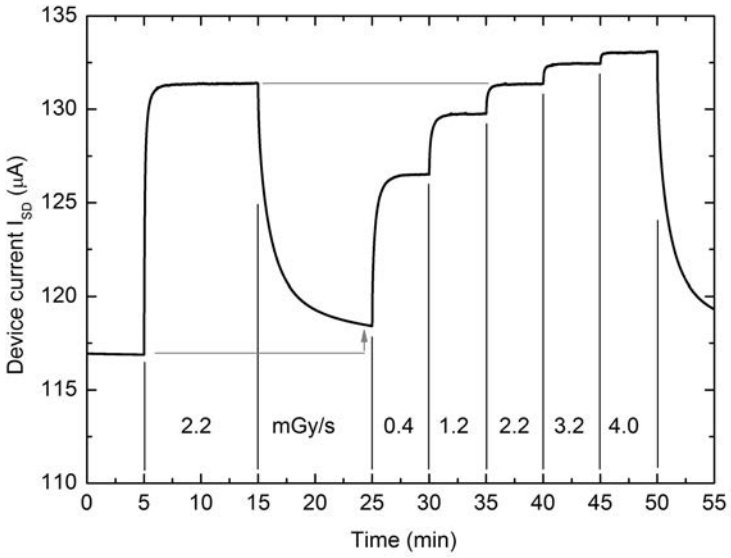

Figure 3.20: Typical device response of a GaN thin film sample (structure 3, wafer TG1592) without at HEMT structure. Although the sensor is still in an excited state after the pre-irradiation peak, the irradiation at equal dose rates yield exactly the same signal level.

The influence of the HEMT channel on radiation measurements has already been discussed in the introduction of chapter 3. Figure 3.21 shows a direct comparison of structures 1-3: a GaN layer with a 500 µm wide channel, a GaN layer with a 30 µm wide channel, and a GaN layer without a HEMT. To provide a direct comparison of the measurements, the plots are off-set to the initial baseline current at t = 5 min. The values of the off-sets are given in figure 3.21. As one could expect, the structure with the broad HEMT channel has the highest baseline current and the structure without HEMT has the lowest one. Nevertheless, although the absolute response scales in height for the different structures, the qualitative characteristics of the x-ray response are preserved. In other words: the HEMT channel on the GaN surface has an influence regarding signal height but does not change the x-ray sensing characteristics. The 2DEG inside the HEMT acts as a 1-dimensional trap for electrons. This quantum well changes the charge carrier distribution near the sensor surface and explains both the different baseline conductivity and the different magnitude of photon induced conductivity. It is unclear why just the structure with the 30 µm channel shows the lowest absolute response. An additional effect

of, for example, contact preparation, can be excluded since a repetition of the experiments with samples from wafer TG400 revealed exactly the same results (not shown here).

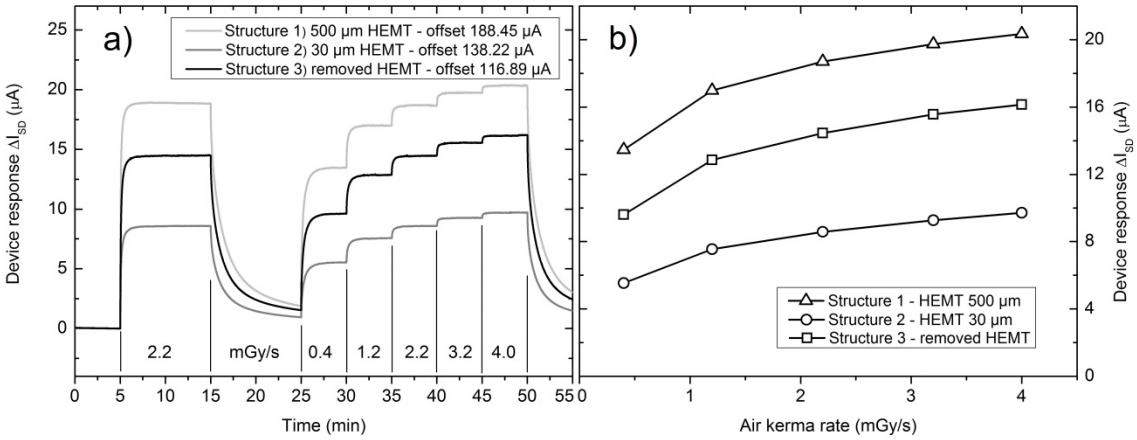

Figure 3.21: Comparison of the influence of the 2DEG channel for measurements with the GaN buffer layer. (**a**) gives the temporal progression of the measured signal and (**b**) the corresponding kerma rate-response curve. The HEMT channel scales the absolute height of the signal but preserves the qualitative x-ray response. Why structure 2, with the 30 µm wide channel, shows the lowest response is unclear.

Structures 4-6 have the same channel widths but different lengths of the active area between the contacts. A direct comparison of a measurement of the devices is given in figure 3.22. While the off-set and, therefore, the baseline current for structure 4 (ladder large) is comparable to structures 1-3, the baseline current increases for structure 5 (ladder medium) and structure 6 (ladder small). With the ohmic behavior of the semiconductor material, one would expect a smaller resistance and, therefore, a higher conductivity with reduced channel length, which is observed. Furthermore, the measurements show an increase of the absolute x-ray response with reduced channel length. This effect is atypical for ionization chambers, where the response is proportional to the detection volume, but can be explained for semiconductor detectors. The velocity v of an electron in an electric field E is determined by the mobility µ of the material. If l is the length of a detector, τ_l is the time for an electron passing the detector lenght.

$$v = \mu E = \frac{l}{\tau_l} \tag{3.4}$$

The GaN layers are operated as active devices with a bias potential and associated baseline current. Due to charge equilibrium, an electron enters the detector at the source contact when a charge carrier has transited the detector length and leaves the material at the drain electrode.

If the recombination time τ of an electron-hole pair is longer than the drift time τ_l ($\tau >> \tau_l$) an electron traverses the detector several times before recombination. In such a way, a photoconductor can yield a positive gain G.

$$G = \frac{\tau}{\tau_l} = \frac{\tau \mu E}{l} > 1 \tag{3.5}$$

Equation 3.5 shows that the gain of an x-ray detector operated as photoconductor is indirectly proportional to the length l of the detector and the results given in figure 3.22 fit well to the this correlation.

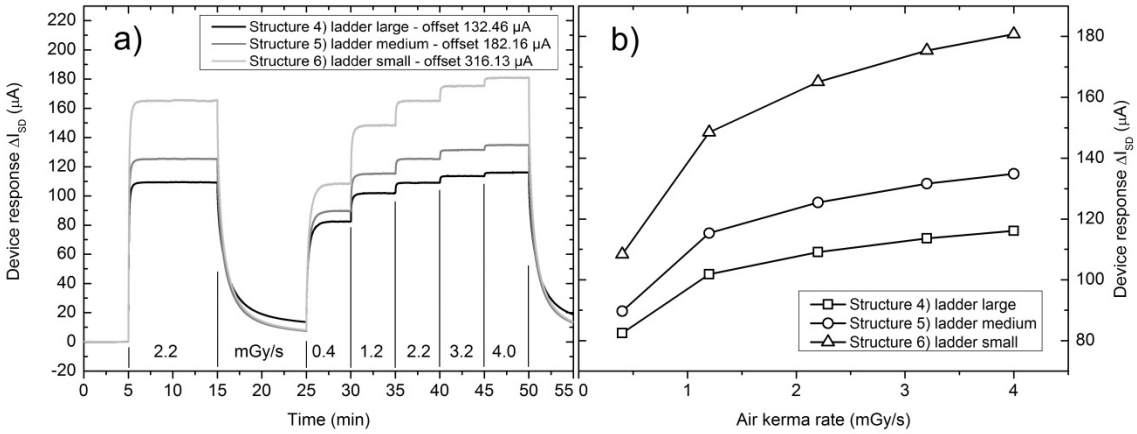

Figure 3.22: Comparison of the influence of the distance between the metal electrodes and the size of the active area. Although structure 6 has the smallest active area it shows the highest response. This is an expectable result since the gain of the device falls with the distance between the contact pads. (**a**) gives the temporal progression of the measured signal and (**b**) the corresponding air kerma rate-response curve.

For structure 4 and 5 it is additionally necessary to consider the metal pads on the active area. All structures in figure 3.22 show a much higher absolute response ΔI_{SD} compared to the measurements in figure 3.21. The absolute response of structure 4 is in the 100 µA regime while the absolute response of structure 1 is in the 20 µA regime, although their overall dimensions are almost similar. The metal-semiconductor interface aligns at the Fermi level via electron transfer processes and usually causes a bending of the conduction band at the heterointerface. Electrons transfer from the n-type semiconductor to the metal and cause a positive space charge region in the semiconductor which is confined to the interface region. Obviously, the shifted potential on the active area lead to an enhancement of the sensor response, although hereby loosing transparency of the devices and increasing x-ray absorption.

Figure 3.23 shows a direct comparison of a 75 kV and a 150 kV irradiation of structure 1. The dose rate response curve is a continuous function of the air kerma rate, without dependence on x-ray energy, which supports the discussion in chapter 3.4.2 that the device works independently of the x-ray energy in this dose rate regime. The continuous line in the rate-

response plot represents a second order exponential fit of both data series. A total error of 0.3% is approximated due to x-ray intensity fluctuations and temperature drifts, which is shown with error bars in the rate-response curve. For the 150 kV irradiation a higher signal is produced due to the higher dose rate. Nevertheless, it is noticeable that the de-excitation of the device after the 10 min pre-irradiation peak declines more rapidly for the 150 kV irradiation and the signal converges faster to the baseline level, though the absolute response signal is higher. This is a clear indicator that the de-excitation process is not a simple decay of equivalent electron-hole pairs and x-ray absorption might become important. Probably, although the photo-voltage saturates, a different steady state proportion is established. Again, a simple correlation between the absorbed energy and the output response does not hold. Although the devices do not show energy related signal magnitude dependence above air kerma rates of ~0.2 mGy/s, the de- and excitation times do.

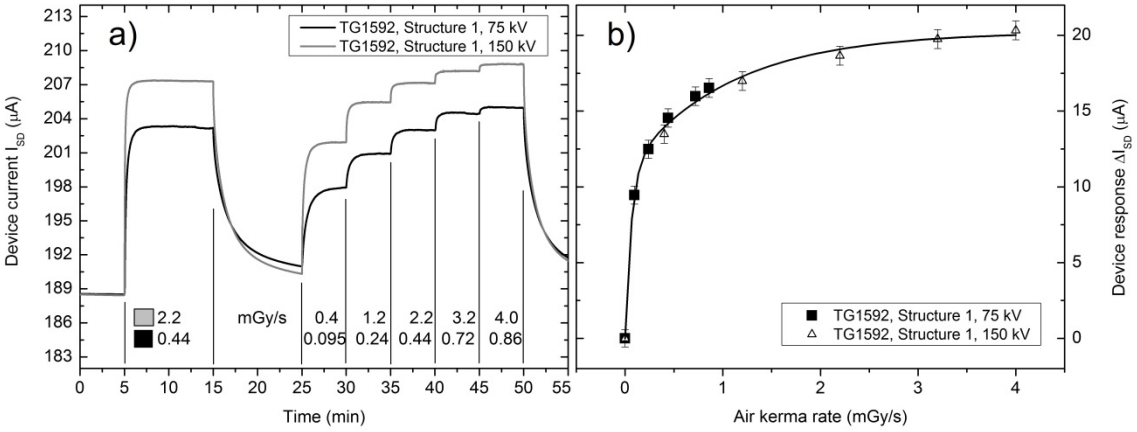

Figure 3.23: Radiation response of a GaN HEMT sample (structure 1, wafer TG1592). (**a**) shows the temporal progression of the measured signal and (**b**) gives the corresponding kerma rate-response. Despite a change in acceleration voltage from 75 kV to 150 kV, the rate-response curve shows a continuous progression. Again, this fact strongly indicates the independence of the sensors to the photon energy in the given kerma rate regime.

Measurements with structures 1-3 at 150 kV acceleration voltage and low air kerma rates below 100 µGy/s are given in figure 3.24. At these rates the devices show a much slower response time compared to the high dose rate regime. Structure 2, with the 30 µm HEMT channel, shows again the lowest absolute x-ray response. It is important to emphasize that the non-linearity in the dose response curves is caused by the limited irradiation time of 5 min. When choosing longer irradiation intervals the rate-response curve is linear, as demonstrated in chapter 3.1 and 3.4.2. However irradiations are performed according to the protocol in table 3.3 to provide a reasonable comparison between all measurements carried out in this chapter.

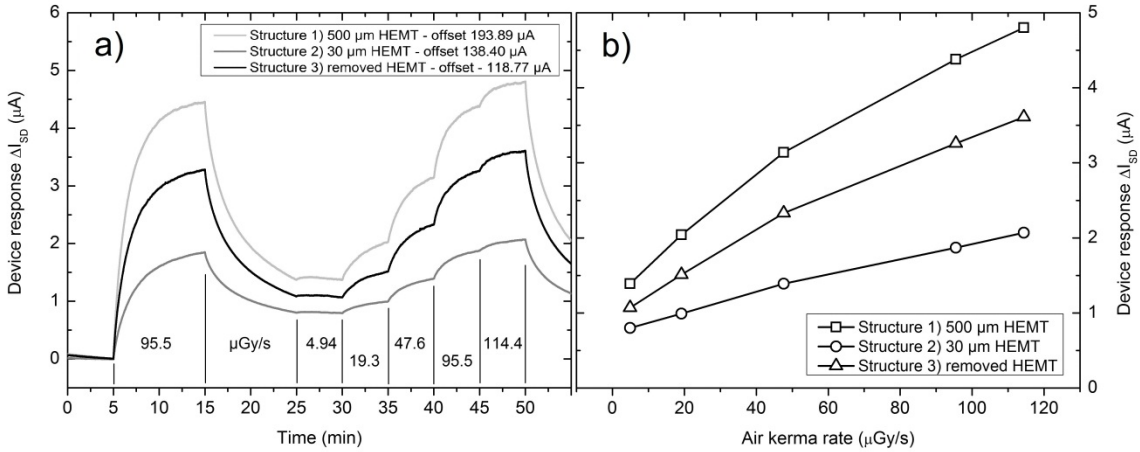

Figure 3.24: Radiation response of a GaN HEMT sample (wafer TG1592) in the low air kerma rate regime. (**a**) gives the temporal progression of the measured signal and (**b**) the corresponding rate-response curve. It is found that the measured signal is dominated by transient times, although a kerma related device response is still preserved. The kerma rate-response plots show a slight non-linearity since the sensor signal was not saturated after 5 min irradiation intervals.

Figure 3.25 shows a comparison of structure 3, a GaN thin film layer without HEMT channel, irradiated with 150 kV x-rays and 40 kV x-rays at low dose rates. The dose response curves are different for different irradiation energies and therefore, show a strong energy dependence at that kerma rate regime. Although the kerma rates are higher for the 150 kV irradiation, the device response is smaller. Here, the dominating factor is clearly the energy related absorption in the material.

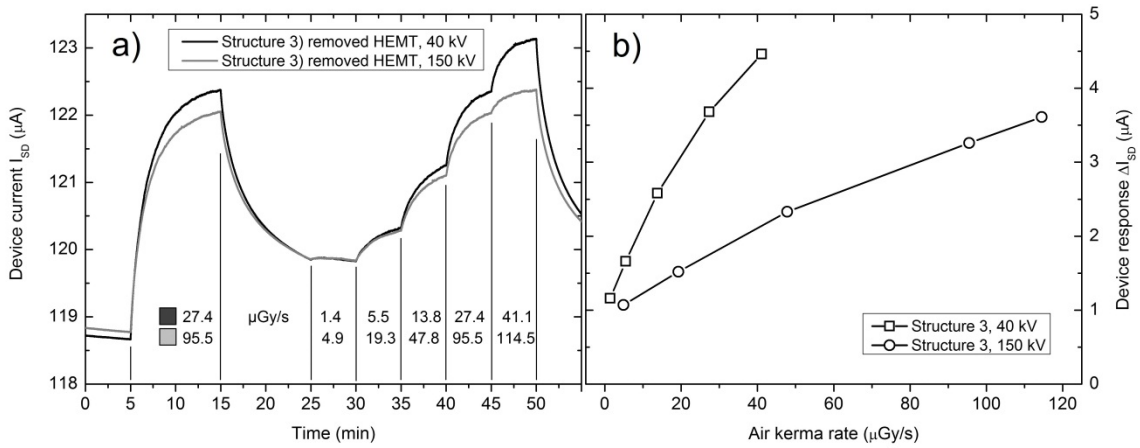

Figure 3.25: Radiation response of a GaN thin film sample (structure 3, wafer TG1592). (**a**) gives the temporal progression of the measured signal and (**b**) the corresponding kerma rate-response curve. A change in acceleration voltage from 40 kV to 150 kV alters the rate-response curve dramatically. In this kerma rate regime (< 0.2 mGy/s) the device response is not independent of the x-ray energy.

Measurements revealed benefits for the device response caused by a wide HEMT/contact channel with a short distance between the electrode pads. Therefore interdigital transducer structures (IDT) on a GaN thin film and a GaN 2DEG structure were investigated. The 12 finger-pairs of the IDT structure have a length of 2 mm each and a width of 50 µm, while the distance between the fingers is also 50 µm. An irradiation with a bias voltage of 10 mV is given in figure 3.26 for the TG1592 and the TG400 wafer. Contrary to expectations, the devices show a very low x-ray response, an unstable signal and a high noise. Repetition of experiments verified reproducibility of the finding and showed that IDT measurements likely suffer from charging effects. To determine the specific effect due to the 2DEG of a HEMT, the experiment was repeated with the Fe compensated GaN wafer 07-535. Although the device response is higher than for the HEMT, the stability is poor and the transients are long compared to the mesa structures.

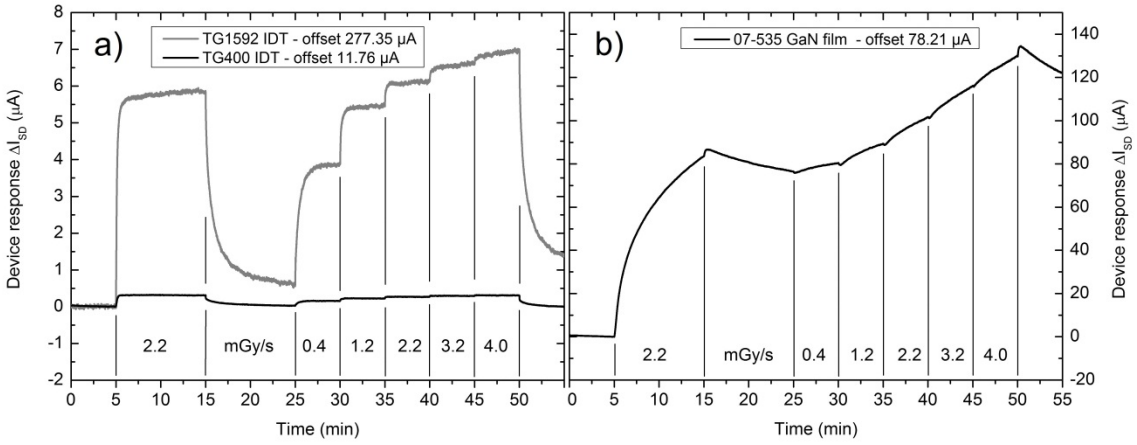

Figure 3.26: (**a**) shows the temporal signal progression of an IDT structure on two different HEMT wafers (TG1592 and TG400). Although the distance of the electrodes is only 50 µm and expanded over a large area, the IDT structures show a relatively low and unstable response. (**b**) shows the IDT signal on a Fe compensated GaN film. Although the radiation induced response is high, the drift times are not appropriate for dosimetry purposes.

3.7 Luminescence

Luminescence is the emission of light from a substance caused by the transition from an excited state to the ground state. The mechanism is called photoluminescence for an excitation of the system with photons, which can be, in turn, split into two parts: fluorescence is the short lived spontaneous emission of light, while phosphorescence is the ability of a material to produce a long-lived after-glow. GaN shows both effects after photo-excitation. In addition to the described electrical measurements, the GaN-sensors can also be used as optical dosimeters. For some applications in medical dosimetry, it can be challenging to provide direct electrical connections to the region of interest. Therefore, the utility of these devices for optically-detected dosimetry based on x-ray induced photoluminescence of GaN is highlighted. The well-known “yellow luminescence” of GaN [Cha2008], which is associated with capture of photo-excited electrons by broadly distributed deep defect-related acceptor levels, is weak under x-ray irradiation, but clearly observable with a low-light camera.

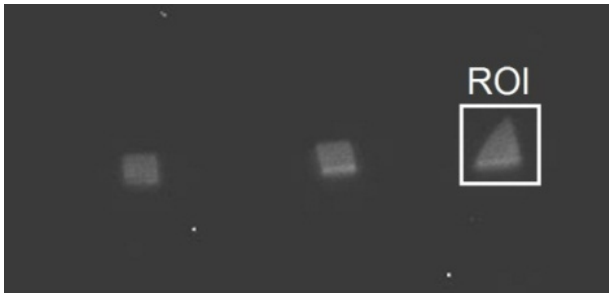

Figure 3.27: Optical image of the luminescence of HEMT samples recorded with a low light camera. The region of interest (ROI) defines the area of the evaluated luminescence intensity.

HEMT/GaN samples were irradiated at different air kerma rates while recording the fluorescence intensity with a Luca S 658M (Andor Technology, Belfast, U.K.) low-light imaging camera, as illustrated in figure 3.27. The sample was irradiated for 30 s at each adjusted air kerma rate, after which a total of 50 pictures were taken within 3 s under constant x-ray irradiation. For evaluation, the average intensity within the defined region of interest (ROI) from the 50 pictures was calculated at each dose rate.

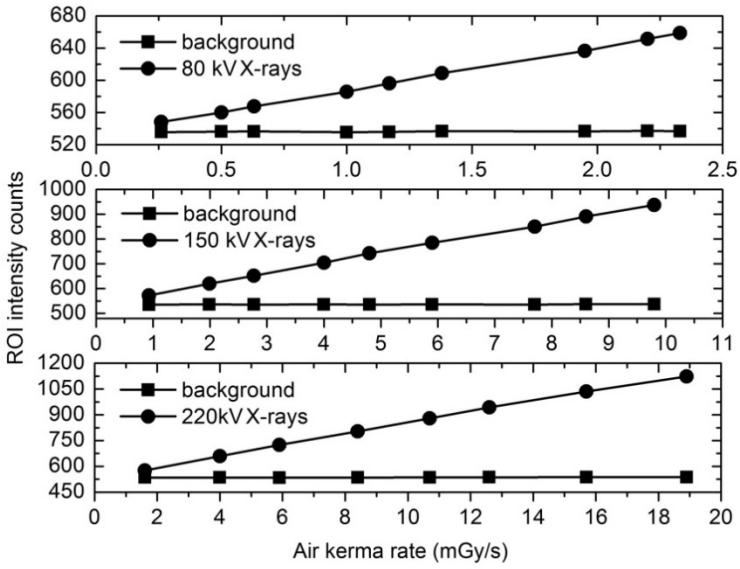

Figure 3.28: Pixel intensity counts for a fluorescent HEMT-sample during irradiation. Pictures were taken with a low light camera. Intensities were averaged over 50 single pictures in the region of interest (ROI) for each signal reading.

As shown in figure 3.28, the average emission intensity is linear with the air kerma rate. Thus, these devices provide the possibility for true multi-mode operation via electrically- and/or optically-detected dosimetry. The background is obtained from the measured intensity next to the ROI.

3.8 Evaluation of GaN-based thin films for sensor applications

Human phantom and object irradiation experiments were performed in order to more fully assess the efficacy of these devices for medical and technical x-ray dosimetry and imaging.

3.8.1 Local dosimetry

The HEMT-sensors were placed in the mid-torso region of a human irradiation phantom composed of both soft tissue equivalent material and a natural human spine, as shown in figure 3.29. The placement of the devices was chosen such that their sensitivities to x-ray attenuation by 2.5 and 5 cm each of human soft tissue and of bone could be measured. The irradiation was repeated five times in order to demonstrate the measurement stability.

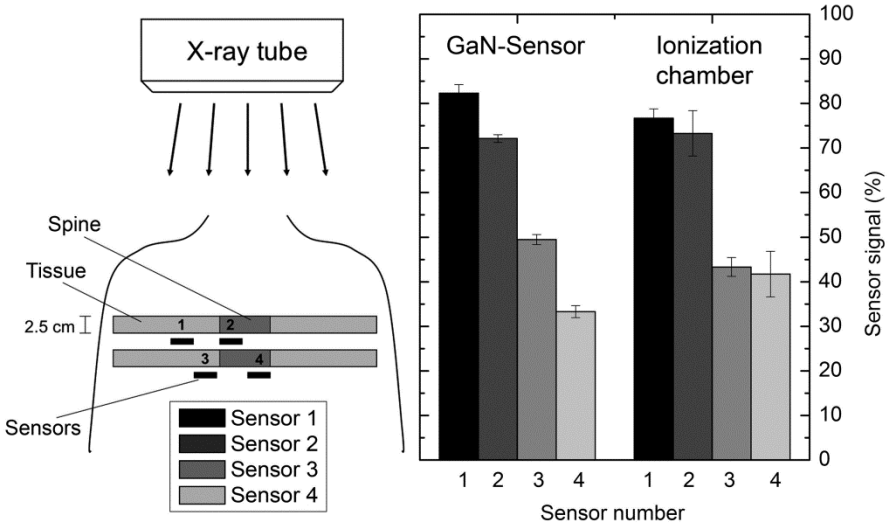

Figure 3.29: Schematic illustration of the sensor arrangement for the human phantom experiments. Sensors were placed behind 2.5 cm thick slices from an Alderson radiation phantom. A human spine is embedded inside soft tissue equivalent material. Two sensors were fixed behind the soft tissue and two sensors behind the bone, for total shielding depths of 2.5 cm and 5 cm for each material. A differentiation of the x-ray attenuation by bone and by tissue is clearly observed in the measurement, as is the impact of the slice thickness. The 100%-level is referenced to 100 kV x-rays in air at a rate of 0.35 mGy/s.

Measured transmission signals for each device, in percent of full-scale response, are shown in figure 3.28 together with corresponding reference measurements obtained from the ionization chamber. Bone material is known to exhibit a higher mass attenuation coefficient than soft tissue, especially at energies below 100 keV [ICRU1989]. The expected difference between x-ray attenuation by bone and by soft tissue is clearly observed. The experiment was

repeated five times and the standard deviations of the signals are presented as error bars in the plot. The average standard deviation for the four sensors is 1.3%, indicating good reproducibility between measurements. Since the dimensions of the ionization chamber are in the range of the spinal diameter, a large positioning error of ±3% due to shape inhomogeneity of a human spine and an additional uncertainty of ±2.1% due to limited decimal resolution of the dose meter (Dosimentor DL4, PTW, Freiburg) must be considered. Due to their small dimensions and high sensitivities, GaN-based devices provide significantly more accurate and reproducible readings.

To further investigate the effect of the x-ray energy distribution under operational conditions, the experiment was repeated using the human phantom set-up shown schematically in figure 3.29. Figure 3.30 shows the results produced by constant air kerma rate irradiation at three different energies. For all sensors, there is a clear dependence of signal on x-ray energy at constant dose rate. As was previously demonstrated, the inherent sensor response depends strongly on dose rate but is nearly independent of energy. Thus, the effect observed in figure 7 is a direct consequence of material specific shielding properties due to energy dispersive x-ray absorption within the phantom. The combined sensitivity of the devices to dose rate and insensitivity to irradiation energy and/or energy distribution permit precise measurements of energy-dependent material shielding. Furthermore, these sensors provide an ideal tool for directly monitoring x-ray doses without the requirement for energy calibration.

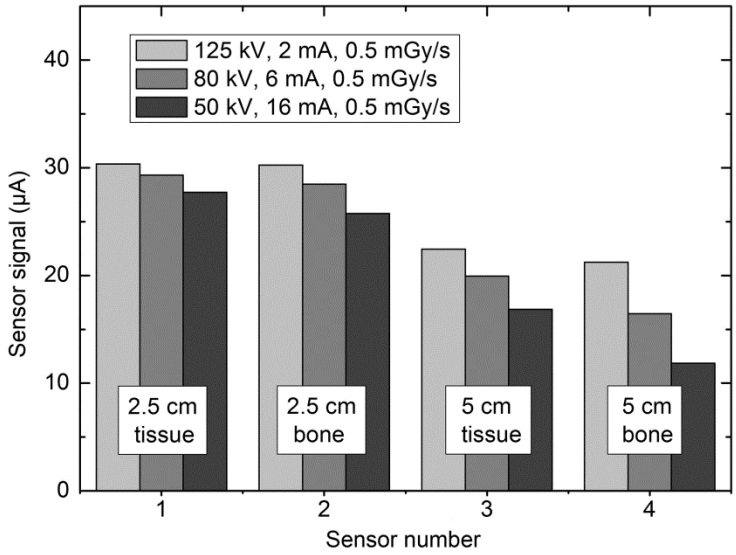

Figure 3.30: Sensor responses under constant air kerma rate phantom irradiations at different x-ray energies using the configuration shown in figure 3.28. As expected, the x-ray transmission through soft tissue equivalent material and human bone is altered by the incident energy and material thickness.

3.8.2 Time resolved dosimetry

To demonstrate measurement dynamics, a transient phantom experiment was performed using water as a variable shielding agent. A HEMT device was placed in a glass cylinder into which water was continuously pumped, with the surface rising at a constant rate of 1.6 mm/s. In order to avoid temperature drifts arising from direct contact with the water, the sensor was placed within an isolated cylinder. The sensor response was converted to dose rate using a calibration curve obtained from reference measurements in air. For comparative purposes, simultaneous air kerma rate measurements were obtained using an ionization chamber. A schematic diagram of the transient water phantom apparatus is shown in figure 3.31.

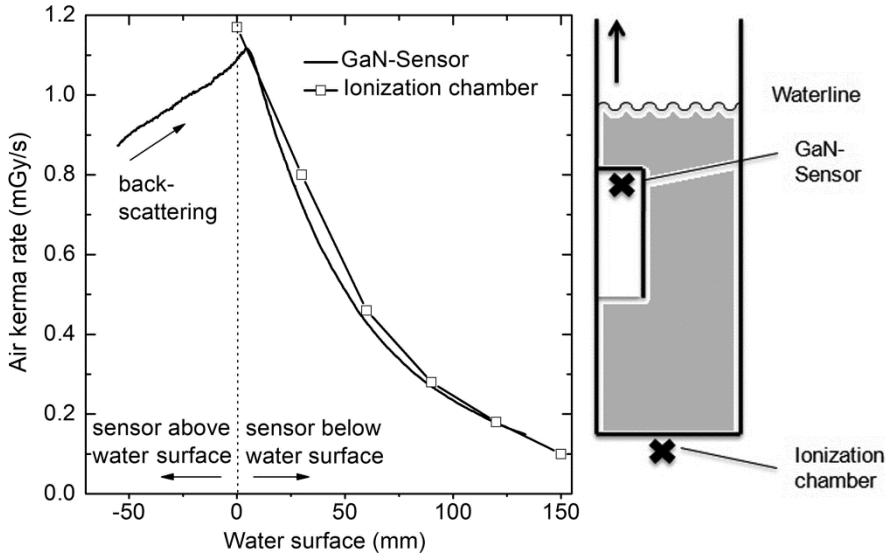

Figure 3.31: Water shielding experiment in which the constant rise of the water level during a continuous irradiation with an air kerma rate of 0.95 mGy/s leads to a transient dose rate. A GaN-sensor and an ionization chamber (23331, PTW) are placed as shown in the illustration. Dose rates measured with the sensor above and just below the water surface exceed the applied x-ray dose rate due to volume back-scattering effects in water.

The measurement was performed under continuous irradiation with 100 kV x-rays at an air kerma rate of 0.95 mGy/s. Initially, a dose rate of ~0.87 mGy/s is observed, a value which is somewhat lower than the known source air kerma rate due to shielding by the isolation capsule surrounding the GaN device. However, as the filling water approached the sensor, the measured signal increased continuously to a maximum dose rate of 1.12 mGy/s, which corresponds to an increase of 18% due to volume back-scattering effects from the approaching water. Although reported values of the backscatter factor (BSF) from water exhibit significant scatter, the observed value is consistent with expectations [Gro1990]. Secondary electrons are produced by the interaction of photons with dense material and these electrons contribute to the absorbed dose. The BSF increases with the atomic number of the interacting material.

Once the sensor passed below the surface of the water, a monotonically decreasing dose rate versus depth was recorded. Due to the low noise relative to the device response, small changes of the shielding thickness are readily observed. Under the current experimental conditions and with the used sampling rate of 9.3 Hz, water shielding changes in the sub-mm range are possible to resolve. We note that, while there is good agreement between the ionization chamber and GaN-sensor responses, geometric differences make quantitative comparisons unjustified and offsets may be present. Nevertheless, comparison of the measured dose rate changes with water depth is valid and excellent agreement is observed.

3.8.3 Imaging

To demonstrate the versatility and possible future applications of these devices, x-ray images of the index finger and wrist sections of a human phantom were obtained using GaN-based sensors. While such devices have the potential to be straightforwardly miniaturized in order to form high density pixel arrays for imaging purposes, the fabricated chips were 5×3 mm^2 and only contained a single device, thus limiting the pixel dimensions to this size. To boost the spatial resolution, an automated two-dimensional translation stage was used to create the images. Several hundred pictures were taken at different offsets from the center position of each pixel with an acquisition time of 200 ms and the data were recombined into a single image by interpolation and averaging. This technique better utilizes the intentional 2.8×1 mm^2 active area of the device, and gives additional data to further enhance the image in post processing. In contrast to conventional semiconductor detectors, images were recorded at room temperature without an additional cooling of the sensor material.

The two-dimensional data were plotted into 8 bit x-ray gray scale contour maps to resemble standard x-ray photographs. For each plot, an optical picture of the corresponding human phantom segment is provided. In figures 3.32 (a-d), the differences between tissue, bone and air, as well as the distances between specific features and joints, can be clearly identified. Furthermore, close inspection of figures 3.32 (a) and (b) reveals that segments of the phantom tissue appear as vertical lines in both pictures.

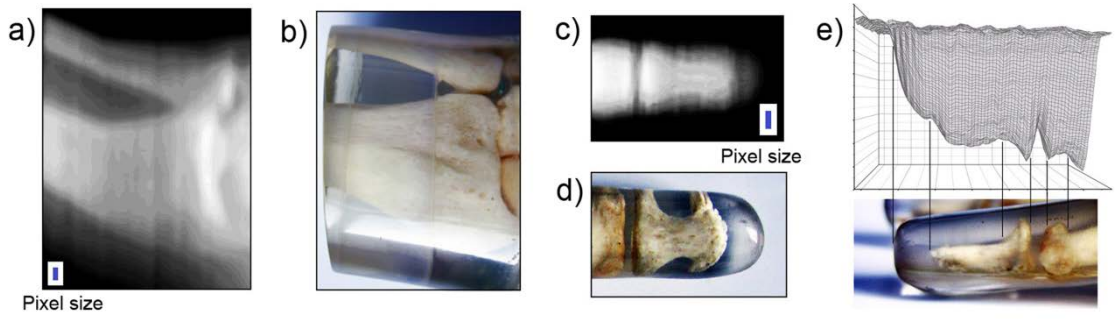

Figure 3.32: The 8 bit x-ray gray scale contour maps recorded using GaN-HEMTs (the total device size is indicated white and the active area blue) of a human (**a**) wrist and (**c**) index finger phantom. Optical pictures of the scanned (**b**) wrist and (**d**) finger phantom. (**e**) Side view of a 3D plot of the data in (**c**) compared to an optical image in the same orientation.

The depth scale of the x-ray images, which correlates well with comparable optical images, can be somewhat misleading and masks the true extent of the data. To illustrate this point, the data from figure 3.32 (c) were plotted in three dimensions and rotated to a side view. The resulting plot is given in figure 3.32 (e) along with an accompanying optical picture in the same orientation. The signal minimum represents the maximum x-ray absorption and correlates well with the profile of the bone in the optical image. Importantly, the large signal arising from x-ray absorption in soft tissue is represented more clearly. In regions away from the finger, the sensor signal reproducibly goes back to the baseline value in air. The results presented here serve to illustrate the utility of GaN-based devices for x-ray imaging applications. Importantly, device dimensions can be reduced by orders of magnitude using standard micro-fabrication techniques. Thus, high resolution imaging with integrated GaN pixel detectors should be possible based on these proof-of-principle measurements.

Another irradiation experiment was performed with a GaN sensor possessing an active area width of 30 µm. To demonstrate possible imaging resolutions a Pb line mask was scanned inside the x-ray beam with a GaN sensor fixed at the XY-translation stage. The mask consists of thin slits in a 0.5 mm thick Pb plate. The limiting factor of the measurement was given by the translation stage, which had a minimum step width of 100 µm. The 1-dimensional scan is shown in figure 3.33. The thickness of the slits is equal to the Pb material separating the slits and is given in line-pairs per millimeter (LP/mm). Therefore, for example, 1.6 LP/mm stands for an opening with a thickness of 0.5×(1/1.6 mm) = 312.5 µm. The overlay in figure 3.33 (a) shows a section of a real optical image of the slit phantom. The image is scaled and adjusted to the measurement peaks. It is clearly observable that the spatial distribution of the peaks corresponds almost perfectly to the optical image. These experiments demonstrate the capability of GaN devices, accomplishing measurements in the sub-mm regime.

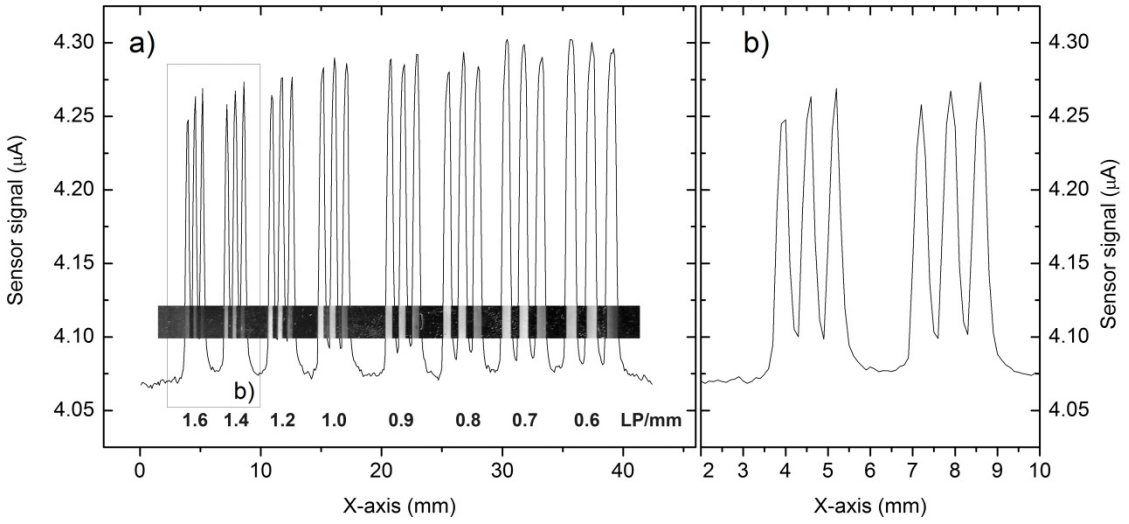

Figure 3.33: Radiation response during a 1-dimensonal scan across a 0.5 mm thick Pb line phantom. The phantom consists of thin openings separated by Pb material with equal thickness. In (**a**) an optical image of the slit phantom is given and adjusted to the measurement. (**b**) shows a zoom in on the first two sets of line pairs (LP).

4 X-ray radiation response of GaN-HEMTs

Experiments in this chapter were carried out at the BESSY II synchrotron (Berlin, Germany). Two BESSY beam-times were achieved by a collaborative application of the Walter Schottky Institute (WSI, Garching, Germany) and the Helmholtz Zentrum München (HZM). A suite of experiments was performed in order to fully assess the detection mechanism of the GaN devices. This, however, is beyond the scope of this thesis and the results can be found elsewhere [How2012]. Nevertheless, a brief presentation will be made on the efficacy for these devices to be used for medical x-ray dosimetry and imaging.

In contrast to the previous chapter, which focused on the radiation response of single GaN buffer layers, this chapter presents the radiation response of a two-dimensional electron gas (2DEG) inside of a GaN-HEMT structure. As already discussed, the HEMT layer does not alter the qualitative radiation response of the GaN buffer layer, evaluated in chapter 3. While experiments in chapter 3 showed the radiation response of GaN thin films, independent of the presence of a HEMT, experiments in this chapter show the pure radiation response of a 2DEG. Experiments with a micro beam at the BESSY II synchrotron enabled the discovery of an intrinsic and independent radiation response of the 2DEG, which is superimposed on the GaN buffer layer signal at dose rates used for experiments in the previous chapter.

The conductivity of the channel between the source and drain electrodes can be altered by applying an external gate potential V_G via a third electrode, located on top of the channel, in order to form transistors. A typical transfer characteristic is given in figure 4.1. The experiments presented in this chapter reveal a strong correlation between gate potential and radiation response of the HEMT and show a high photon sensitivity of the 2DEG channel.

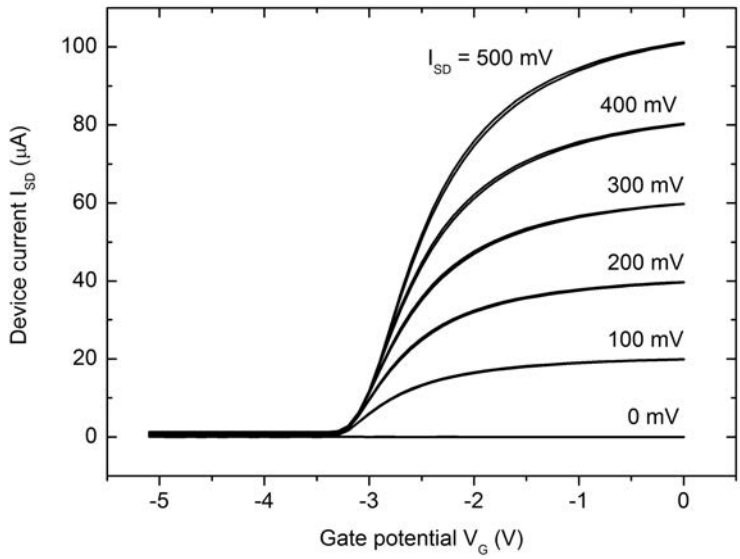

Figure 4.1: Cyclic characterization of a HEMT device with a Pt gate electrode at different source-drain voltages U_{SD}. The observed behavior is characteristic for HEMTs and comparable to applying a gate bias via an electrolyte.

For irradiations on different locations on a HEMT sample, a micro beam with a spot size of ~3 µm was used. Monochromatized x-ray radiation was produced at the BESSY II synchrotron source. If not otherwise noted, 7 keV x-rays were used for the irradiation experiments. The micro beam of the µ-spot beam line provides the possibility to irradiate specific regions of the HEMT device and investigate their behavior during x-ray illumination. Figure 4.2 shows schematically the irradiated regions of the device:

1) On the gate electrode and on the HEMT channel
2) Off the gate electrode but on the HEMT channel
3) Off the HEMT channel but between source-drain electrodes (GaN buffer response)

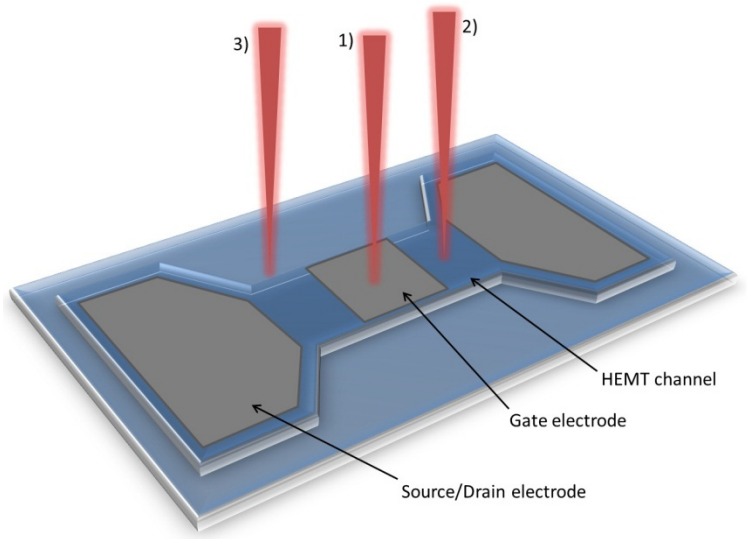

Figure 4.2: Irradiation locations on the HEMT device. The illustration shows a HEMT mesa structure with electrodes (gray). **(1)** illustrates an irradiation on the gate electrode and on the HEMT channel, **(2)** an irradiation on the HEMT channel but off the gate electrode, and **(3)** an irradiation of the buffer layer next to the HEMT channel.

During illumination, the device was biased with a source-drain voltage of 120 mV and the photon flux was measured with an ionization chamber. Two dimensional scans were performed by moving the HEMT sensor at the focal point of the x-ray beam with a translation in X- and Y-directions, while the beam is located parallel to Z-direction. Beam intensities were adjusted with filter sets. Figure 4.3 shows a typical beam intensity curve for a pre-filtration with a 0.2 mm Al filter and a V-slit filter, moving from position 5 to 25. The filter blocks the photon intensity completely up to position 8 and opens completely at position 20. This instrument behavior is similar for different pre-filters, which scale the total intensity.

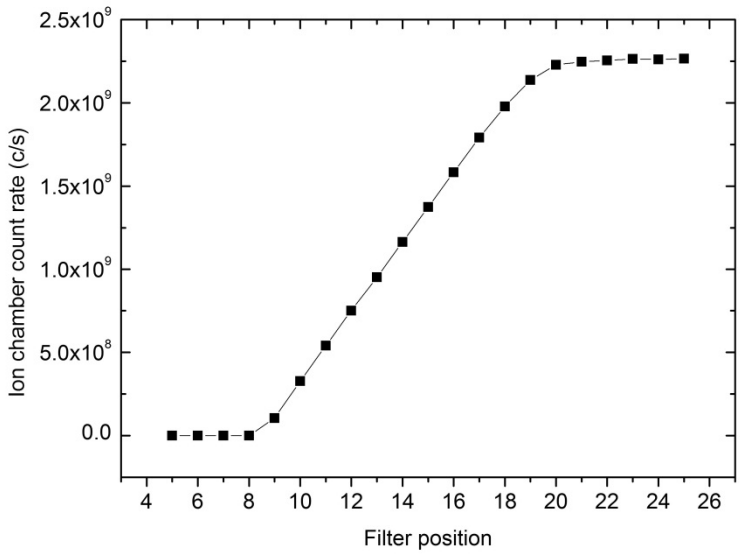

Figure 4.3: Ion chamber counts as a function of the V-slit filter position. The filter starts opening at position 9 and is completely opened at position 20. Between these settings, the filter shows a linear behavior. Due to a capillary after the ionization chamber, the count rate for photons hitting the sample must be divided by a factor of 300.

The beam is focused with a silica capillary which is mounted between the ionization chamber and the GaN samples. Since the capillary blocks a large fraction of the x-ray intensity, only 0.33% of the photons counted by the ionization chamber hit the GaN sample. In the following chapter, the graphs are plotted using this correction of the photon counts. For an overview, the entire beam path is illustrated in figure 4.4.

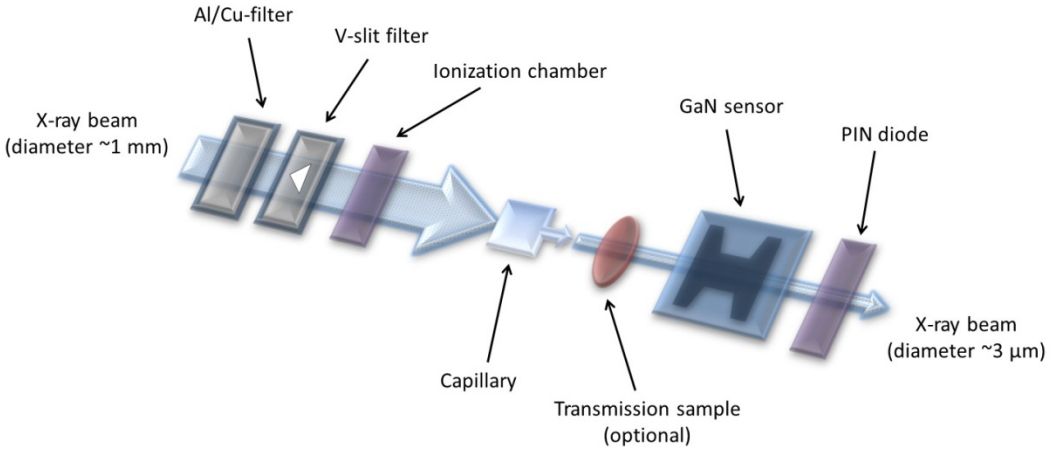

Figure 4.4 Schematic illustration of the x-ray beam path at the µ-spot beam line at the BESSY synchrotron. Transmission samples are used for the imaging experiments, shown in chapter 4.3.1.

4.1 Buffer vs. HEMT response

The results of an irradiation of a 20 µm HEMT channel (position 2) with a pre-filtration of 0.2 mm Al are shown in figure 4.5 The device was operated with a bias voltage of U_{SD} = 120 mV and without a gating of the HEMT channel. The response of the sample is clearly observable and starts immediately at filter position 8. Comparison with an irradiation next to the HEMT channel (position 3) in such a way that only the GaN buffer layer between source and drain contact is irradiated, reveals that the GaN buffer layer shows no response at all for given filter settings (not shown here). This fact proves that the response, shown in figure 4.5, is a result of the presence of the HEMT channel, while the beam intensities are too low to produce a measureable signal in the GaN buffer layer.

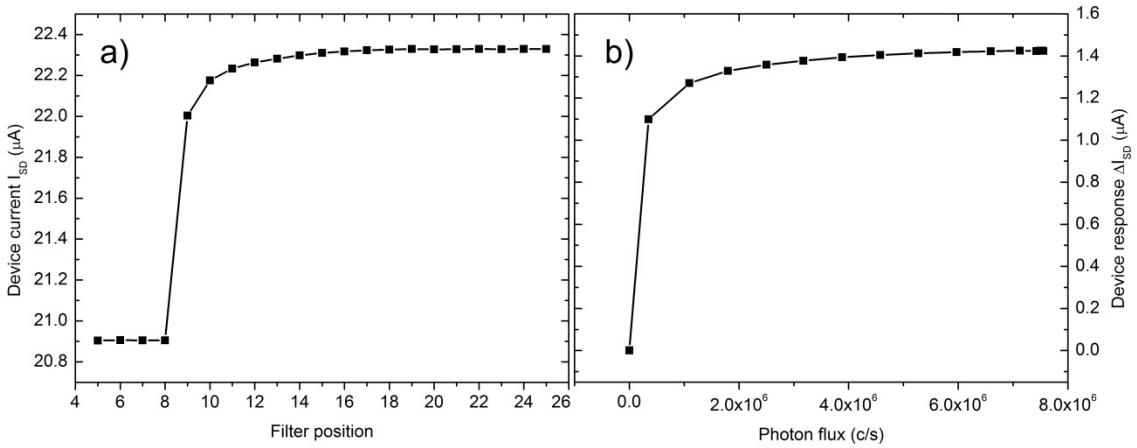

Figure 4.5: (a) shows the device current I_{SD} of the HEMT according to different V-slit filter positions with a 0.2 mm Al pre-filtration. **(b)** illustrates the corresponding device response as a function of the photon flux, given in photon counts per second (c/s). The device shows a similar behavior compared to the measurements with a single GaN buffer layer.

It was possible to produce a signal at position 3 by increasing the photon flux to a factor of $> 10^{10}$ counts per second (c/s) by removing the pre-filtration completely. The threshold difference of the GaN buffer layer and the HEMT response is shown in figure 4.6. These results support the finding that the GaN buffer layer does not contribute to the device response at lower photon intensities and the x-ray sensitivity is enabled only by the heterostructure. At these photon rates, either the recombination times of electron-hole pairs inside the single GaN buffer layer are too fast or the electron mobility of in the GaN is too low to produce a measureable signal. However, the 2DEG channel enables much higher electron mobility. Free electrons produced near the material interface could be trapped inside the potential well, thereby amplifying the device response, as will be discussed.

The height of the HEMT signal is in the sub-µA regime and saturates with photon rate. Therefore, the signal is superimposed by the buffer response for the large area irradiations

presented in chapter 3. A separation of the two signals is possible by reducing the photon flux until only the HEMT response is observable. As already discussed, the HEMT response has no impact on the GaN buffer measurements (with HEMT channel on top) since at such high dose rates the HEMT channel causes only a constant offset.

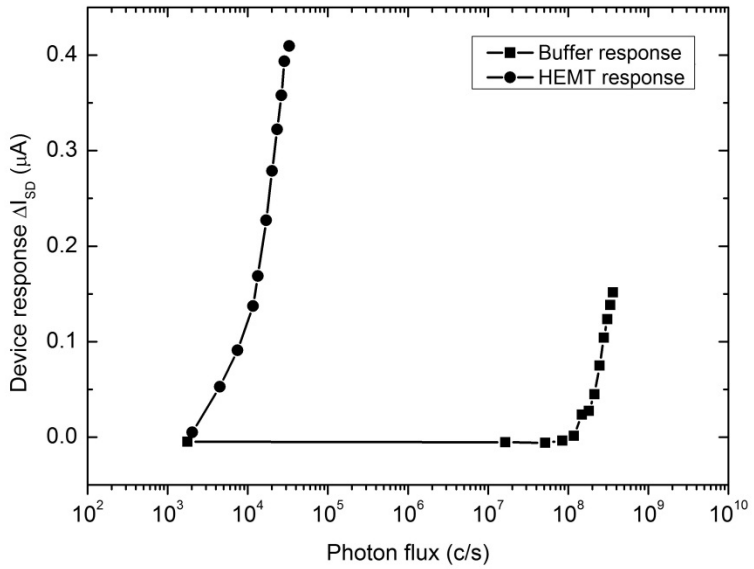

Figure 4.6: Direct comparison of the buffer response and the HEMT response. The plots are achieved by adjustment of the V-slit filter. Both plots show the threshold for response at low photon rates. For the HEMT response, about 10^4 - 10^5 fewer photons per second are necessary to produce a measureable signal.

Measurements with low photon rates reveal that the devices have great potential for dosimetry with very low x-ray intensities. Furthermore, for any incident intensity, it is possible to reduce the photon intensity with appropriate filters to a regime where only the HEMT channel of the GaN device is photo-responsive. Especially in medical imaging, a reduction of dose is one of the main goals. As shown in figure 4.6, a similar HEMT response is observed at ~10^4 times lower photon rate. The sensitivity of the HEMT channel with a 1 mm Al pre-filtration is shown in figure 4.7. While the ionization chamber is operated below its responsivity limit, the HEMT sensor still recognizes a change in photon flux due to the movement of the V-slit filter. This experiment shows again the huge potential of the HEMT devices for dosimetry purposes, especially when considering the enormous difference in detection volume.

By moving the sample in X- and Y-directions, it is possible to produce a sensitivity map of the HEMT channel. Figure 4.8 shows the mapping of a 120 mV biased, 20 µm thick HEMT channel with 0.2 mm Al pre-filtration of the x-ray beam. The movement and therefore, the resolution in X-direction, were 2 µm and the resolution in Y-direction was 3 µm. After every movement step the device current was recorded by automated computer control. The measurement reveals an artifact in the HEMT structure which is most likely caused by an error during etching and processing of the HEMT sample. This feature was observed for all measurements at the

same sample position, carried out with this device. Nevertheless, again, a clear response of the HEMT channel is observed while the buffer layer exhibits no response when the beam leaves the mesa structure at the given intensities. The maximum device current I_{SD} shows a small decrease during the measurement which is most probably caused by the exponential decay of the synchrotron intensity, since the whole measurement took about 4 h.

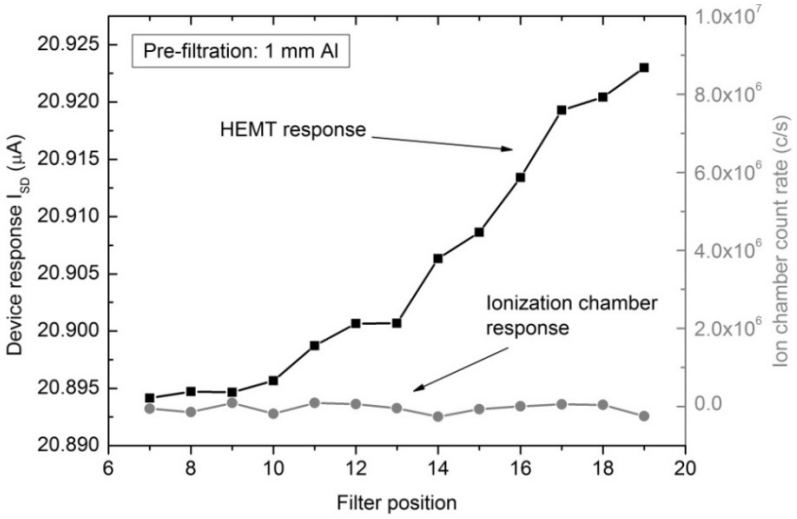

Figure 4.7: Direct comparison of the HEMT response and the reading of the ionization chamber with equal pre-filtration. While for the HEMT a signal change is still observable, the ionization chamber shows no response in this regime. The reading of the ionization chamber must be divided by a factor of 300 to achieve the photon flux hitting the GaN device due to the presence of the capillary.

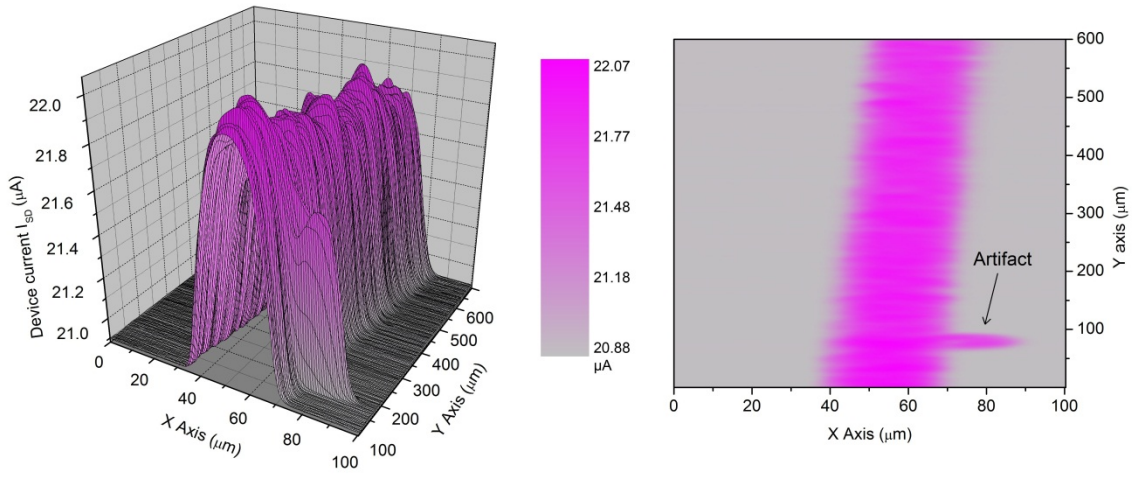

Figure 4.8: Plot of a 2-dimensional scan of a GaN-HEMT sample with a 20 µm channel. The HEMT device is moved inside the beam in the X- and Y-directions with a translation stage. For a pre-filtration with 0.2 mm Al, a response is only observable in the 2DEG channel region. The feature at Y = 80 µm indicates a blemish in the lithography and etching process of the HEMT channel.

4.2 Transient behavior

This chapter focuses on the beam on/off current transient times of the GaN devices. The transient times were investigated after switching the x-ray beam with a beam shutter. The movement time of the shutter is about 20 ms, which is in the same range as the acquisition frequency of the measurement devices. Therefore, investigation of device drifts was limited by the utilized equipment and device analysis below the sub-20 ms regime was not possible. Figure 4.9 shows a comparison of an irradiation at position 3, next to the HEMT channel, and at position 2, on the HEMT channel. Figure 4.9 (a) illustrates a GaN buffer response, which is comparable to the buffer irradiations in chapter 3. The 25 s irradiation peak without pre-filtration shows the typical transients, as well as a baseline offset before and after irradiation. However, the irradiation of the HEMT channel, plotted in figure 4.9 (b), shows a highly improved behavior for x-ray dosimetry. The beam is pre-filtered with a 0.2 mm Al filter, resulting in a beam intensity in the range of 10^6 c/s before traversing the capillary. At this intensity, the buffer layer shows no response at all and the signal is generated exclusively by the HEMT channel. As discussed in the previous chapter, the HEMT shows a much higher response compared to the buffer layer, although the beam intensity is about 10^4 times lower. Transient times for the HEMT are below 20 ms, and therefore not observable with the measurement apparatus. Furthermore, there is no offset in the baseline current.

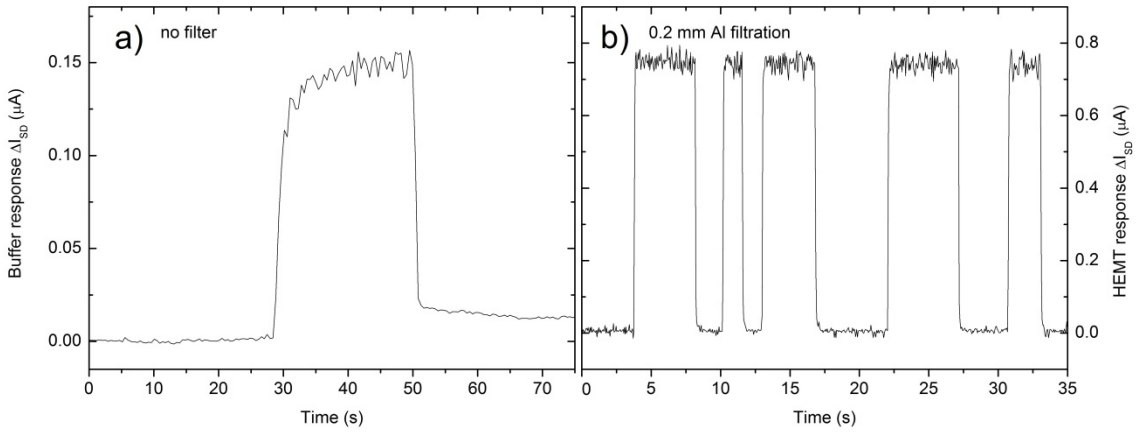

Figure 4.9: Direct comparison of the temporal progression of an irradiation pulse on the buffer layer (**a**) and the HEMT channel (**b**). To produce a signal in the buffer layer, no pre-filtration was used. The response shows the typical characteristic, an exponential signal increase and offset of the baseline current after the irradiation pulse. For irradiations of the HEMT channel, transient times were faster than the data acquisition and shutter response times and the baseline offsets were observed.

These measurements reveal the high potential of the HEMT devices for possible future dosimetry applications. Although the GaN buffer layer sensors exhibit a novel and sophisticated method for radiation dosimetry, the HEMT sensors represent a further enhancement regarding dosimetry, since the device characteristics make them well suited for radiation detection and dosimetry. With given sensitivities of these devices, reductions of the radiation doses for medical applications by several orders of magnitude may be possible.

4.3 X-ray response of gated devices

To test the influence of the gate potential V_G on the device response, a HEMT sensor with a gate electrode was prepared. As shown in figure 4.2, a Pt gate electrode was evaporated onto a 500 µm wide HEMT channel in such a way that the width of the channel is covered with the contact pad but both covered and uncovered areas exist along the length of the channel. This allows radiation of the HEMT channel at position 1, directly on the gate contact, and at position 2, off the gate contact. The cyclic transfer characteristics of the device are shown in figure 4.1 for different source-drain voltages. The behavior of the metal gated transistor is similar to those with a gating via an electrolyte, described in detail in chapter 6. The leakage current across the gate electrode is, as for the ISFETs, negligible.

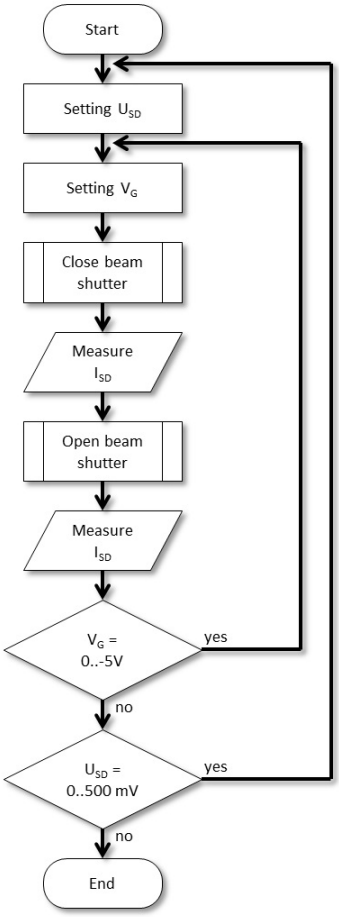

Figure 4.10: Program flow chart for the measurement of the device response. To test the influence of irradiation, one measurement is performed with open beam shutter and one measurement with closed beam shutter at a given source-drain bias U_{SD} and gate potential V_G. To achieve a complete characterization, the measurement was repeated at different U_{SD} and V_G.

Communication between the LabView measurement program and the beam shutter of the BESSY µ-spot beam line was established to test the device response. In this way, it was possible to write a program code to measure the source-drain current I_{SD} at a given gate potential V_G first with open shutter and then with closed shutter, before adjusting the next value for V_G. This automated method was possible due to the much faster transient times of the device compared to the characterizations of the GaN buffer response. The subsequent measurement of on/off data points reduces long time drift errors. A program flow diagram is given in figure 4.10.

The device response ΔI_{SD} of the HEMT sample irradiated at position 2 (on HEMT channel, off gate contact) is shown in figure 4.11, which was calculated by subtracting the measurement value I_{SD} with closed shutter from the measurement value I_{SD} with open shutter. Two values from a cyclic forward and backward scan of the gate potential V_G with a resolution of 20 mV were averaged. The irradiation was performed with a 0.2 mm Al pre-filter at a measured photon rate in the range of ~0.7×10^6 c/s. In contrast to the device with the 20 µm wide channel, the device with the 500 µm wide channel and the Pt gate shows nearly no response at zero gate potential. Applying a negative gate voltage increases the device response. The channel is shut down at gate voltages lower than V_G = -3.3 mV, while the device response stays at a constant level. This experiment reveals that the amplification of the sensors can be adjusted via external gating of the HEMT channel. Therefore, the sensors provide a method for tuning the sensitivity in dosimetry applications. This fact could be a substantial advantage for the implementation of the sensors in medical devices. A detailed description of these physical mechanisms was recently published by Howgate *et al.* [How2012].

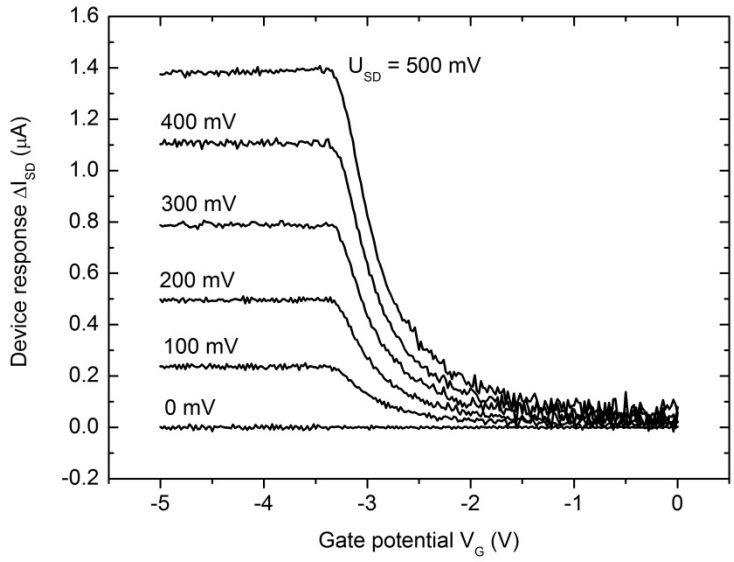

Figure 4.11: Device response of the HEMT channel. The signal is recorded according to the program flow chart given in figure 4.10. The channel is irradiated next to the gate electrode with a 0.2 mm Al pre-filtration.

An estimation of the measured charge carriers per time and the absorbed photon energy reveals that the device in fact amplifies the signal and energy conservation by a simple electron-hole pair production does not hold. The average absorbed energy per single photon can be estimated for a 2.5 µm thick GaN layer to 764 eV using the x-ray transmission tool from the Center for x-ray Optics [Hen1993]. For a photon rate of ~3.5×10^6 c/s and a measured response current $\Delta I_{SD} \approx 0.25$ µA (at a bias of $U_{SD} = 100$ mV) it is possible to estimate a maximum absorbed energy of 1.6 meV per measured charge carrier. As for the buffer response, this value is at least 3 orders of magnitude smaller than the bandgap of GaN (3.4 eV) which is the minimum energy for the production of an electron-hole pair. This analysis reveals that internal amplification within the HEMT must occur in order for these response currents (see figure 4.11) to be generated.

For device irradiation at position 1, directly on the gate contact, the pre-filtration was reduced to 0.06 mm Al due to the additional absorption of the Pt layer. A repetition of the measurement yields the results presented in figure 4.12. Down to a gate potential of -3.3 V, the device shows the same qualitative behavior as for the irradiation next to the gate electrode. However, when the channel is closed completely, the device response is quenched. Since the absorption in the Pt layer is only in the lower percentage range the total device response is smaller compared to the off-gate irradiation. While the conductive path for the whole active area and therefore the amplification of the channel could be altered with a local gate potential it is only possible to have a direct impact on charge carrier generation and de-excitation with an adjacent potential via a metal contact. In other words: it is possible to alter the x-ray sensing characteristics by a very thin gate electrode which only covers a small fraction of the HEMT channel. It is not necessary to shield the whole channel with a metal in order to adjust the x-ray sensitivity. Again, details can be found in Howgate *et al.* [How2012].

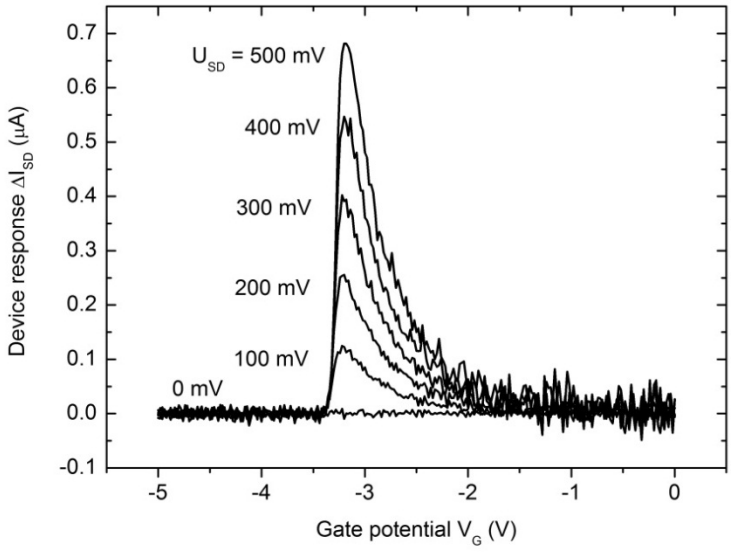

Figure 4.12: Device response of the HEMT channel. The signal is recorded according to the program flow chart given in figure 4.10. The channel is irradiated on the gate electrode with a 0.2 mm Al pre-filtration. In contrast to the irradiation next to the gate electrode, it is possible to quench the radiation response at high negative gate potentials V_G.

4.3.1 Imaging

Imaging by use of the HEMT channel response was carried out by aligning a transmission object between the capillary and the HEMT sensor. First, the GaN device was brought into beam focus without a scan sample and then the sample was aligned with a second three-dimensional translation stage. In contrast to the imaging experiments with the GaN buffer layers, shown in chapter 3.8.3, the transmission sample itself is moved during the intensity scan and the sensor stays at a fixed position. From the physical point of view, it does not matter if the sample or the sensor is moved but the resolution is now determined by the size of the x-ray beam and the movement step length of the translation stage for the transmission sample. The intention of these experiments was simply to show the imaging capabilities of the devices in order to carry out proof-of-principle experiments.

The scans were performed with a Pt gated device with a 500 µm HEMT channel. The beam was focused on the HEMT channel but not on the gate contact (position 2). The source-drain bias was set to 120 mV and the gate was biased to V_G = -3.5 V. Thus, the channel current is quenched nearly completely, while the device response is set to its maximum amplification. All measurements in this section were performed with 5 keV x-rays.

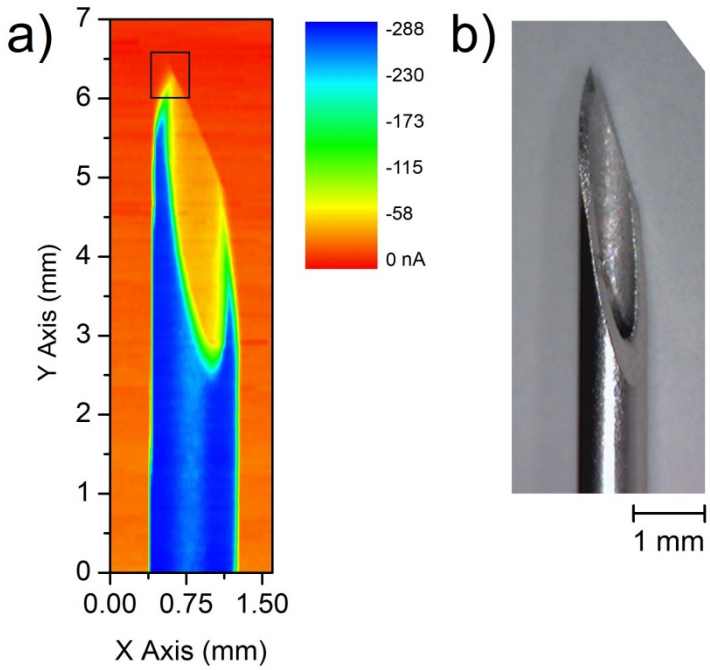

Figure 4.13: (a) shows a transmission image of a syringe needle. The sample was moved inside the x-ray beam with a translation stage, while the GaN sensor was fixed at the focal point. The colors represent the signal change caused by absorption in the sample. **(b)** shows a real optical image of the syringe for comparison. The box in **(a)** indicates the area of the high resolution scan illustrated in figure 4.14.

Figure 4.13 shows a scan of a tip of a medical syringe needle. The movement step width and therefore, the resolutions, are 26 µm in the X-direction and 58 µm in the Y-direction. The scale bar gives the decrease of the device current ΔI_{SD} due to sample absorption of the x-rays, normalized to the background current. The data in figure 4.12 is not corrected or manipulated in any way. The plot represents the raw data. The right pattern shows an optical micrograph of the syringe for comparison. One should emphasize that even the cylindrical channel inside the metal syringe is observable.

For demonstration of imaging capabilities, the measurement was repeated at a higher resolution. Since the scans take about 4-5 h, only the lower end of the tip was measured. The result is given in figure 4.14. The resolution is 2.25 µm in the X-direction and 2.75 µm in the Y-direction.

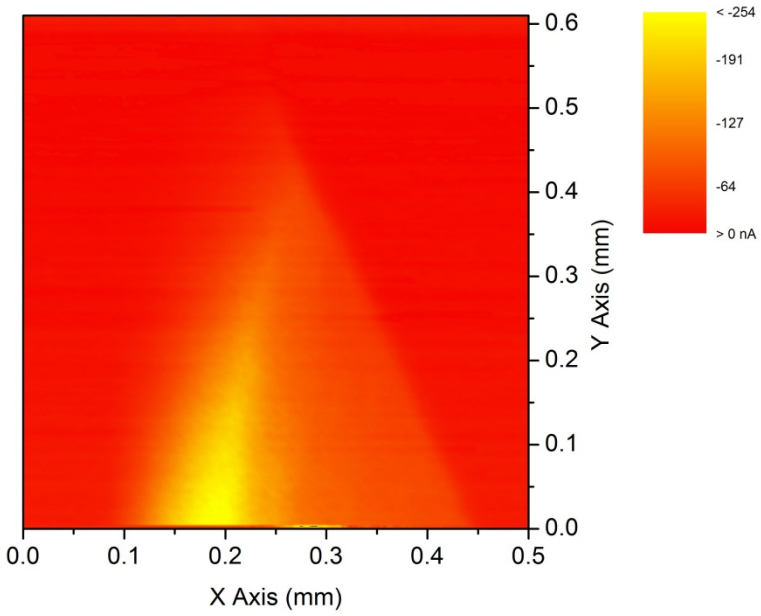

Figure 4.14: High resolution image of the outer tip of the syringe. A small area of the syringe tip shown in figure 4.13 (b) is scanned with a high spatial resolution of 2.25 × 2.75 µm.

For a further demonstration of the imaging capabilities of the HEMT devices, the spiral-glow filament of a flashlight was scanned, as illustrated in figure 4.15. The scanning resolution was set to 20 µm × 20 µm to achieve a complete image of the bulb. This image shows clearly the outer border of the glass casing and the cavity inside. The tungsten filament is observed inside the cavity, even at this resolution. A 10 µm × 10 µm scan shows a zoom-in into the cavity and another 1 µm × 1 µm scan shows a high resolution image of the filament itself. For the scan with the 1 µm motor movement, the total resolution is enhanced by oversampling since the beam diameter is about 3 µm. Therefore, the beam diameter is the limiting factor for the given scan. Nevertheless, intention of these experiments is to demonstrate the imaging capabilities of the devices. Although for the given measurement configuration the sensor characteristics

are independent of the device size, it is possible to produce device structures or arrays with active areas in the sub-µm regime, which may allow high-res imaging with large x-ray fields.

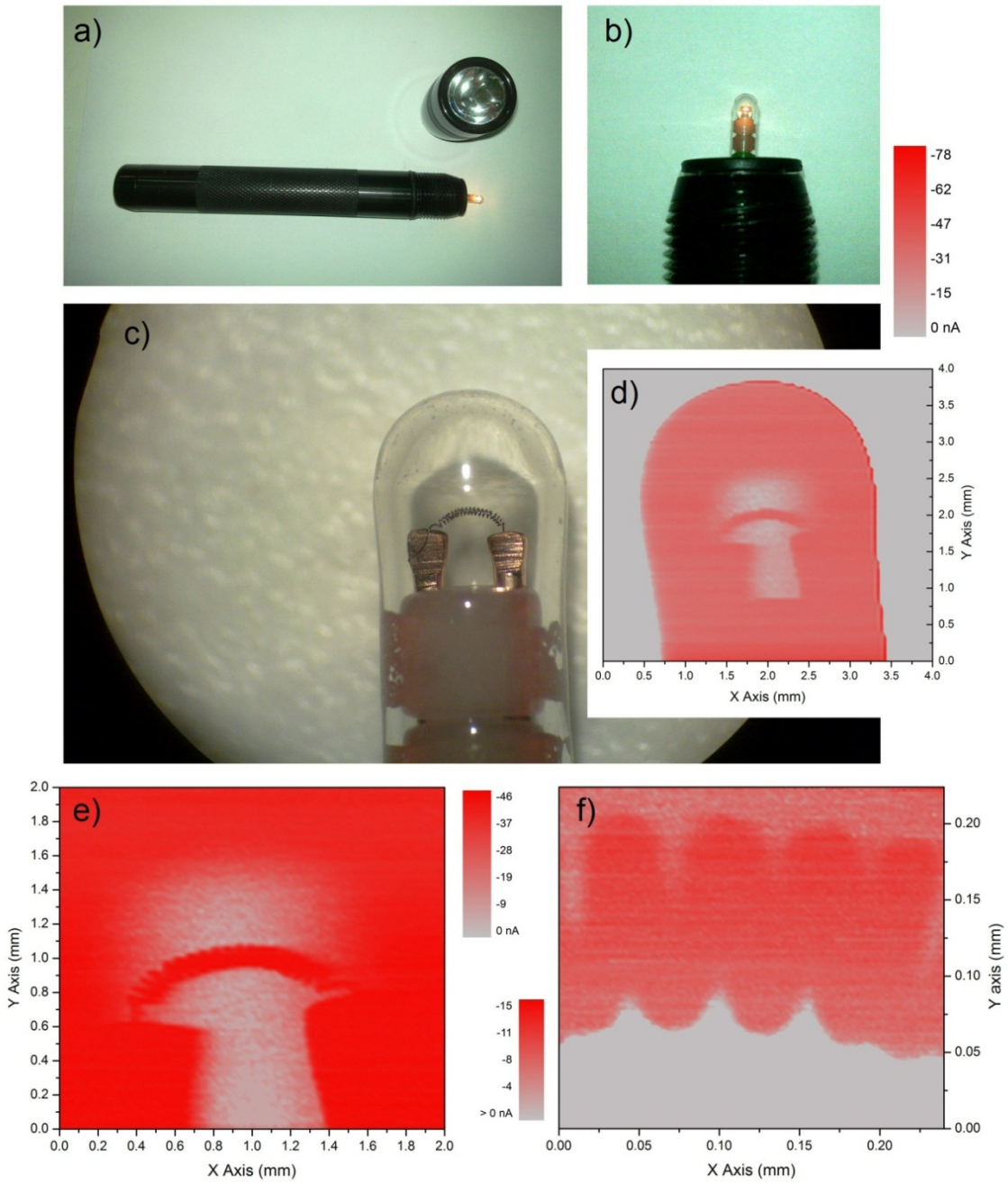

Figure 4.15: Transmission measurement through a light bulb of a flashlight. (**a**), (**b**), and (**c**) show real optical images of the light bulb at different magnifications. (**d**), (**e**), and (**f**) show plots of the device current according to the X- and Y-positions of the sample for different areas and spatial resolutions: (**d**) 20 × 20 µm, (**e**) 10 × 10 µm, (**f**) 1 × 1 µm. While (**d**) shows the whole bulb with the cavity and the glow filament inside, (**f**) shows at a higher magnification only a part of the glow filament but with a very high spatial resolution. The legends give the current change ΔI_{SD} due to the change of x-ray intensity, caused by photon absorption of the sample.

Another imaging experiment was performed with small Cu letters evaporated on synthetic substrate. The absorption of the substrate is constant since it has homogenous thickness. The current change ΔI_{SD} is therefore caused by absorption of the 140 µm thick Cu letters. The scanning resolution was 20 µm in the X-direction and 12 µm in the Y direction. It is observed that the transmission image (figure 4.16 (a)) fits perfectly to the optical image (figure 4.16 (b)) of the letters. Even small partial damages are observed in the transmission scan. This experiment demonstrates the potential of the devices regarding material analysis with very low photon intensities.

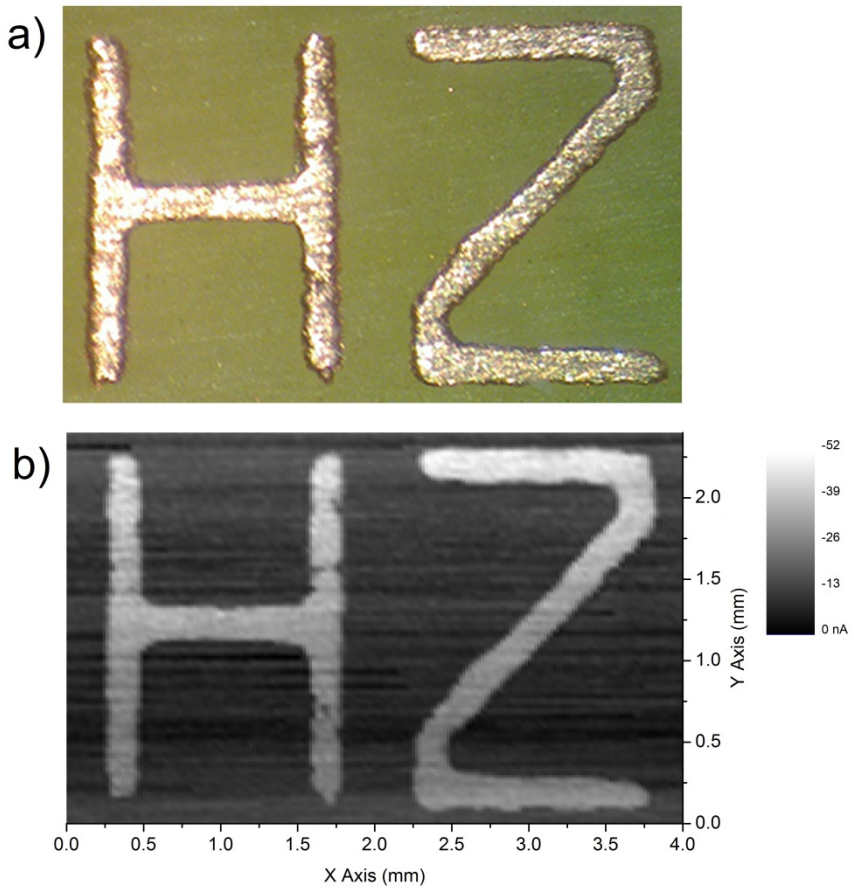

Figure 4.16: Transmission image through 140 µm thick Cu letters. The transmission image **(a)**, which results by plotting the device current according to the X- and Y-position of the sample letters, compared to a real optical image of the letters **(b)**.

5 Proton radiation response of GaN HEMTs

Nearly all previous work in the past years regarding impact of ion irradiation on GaN-HEMTs was carried out to test material damage after heavy particle hits [Luo2001, Luo2002], and not to utilize the device itself for particle detection. Nevertheless, Neuberger *et al.* showed the sensitivity of GaN-HEMTs to negatively and positively charged ion beams in the kV regime [Neu2002]. He reported a channel current modulation during an exposure of the HEMT devices to ions, generated by ion spray technique.

In order to test the response of the GaN devices to highly energetic ions, irradiations at the Munich Tandem Accelerator (Technische Universität München, TUM) were performed. The facility consists of an ion source in combination with a Van-de-Graaff accelerator, which utilizes a high voltage twice to accelerate particles. For this work, only protons with a final energy of 20 MeV were utilized. The SNAKE (superconducting nanoprobe for applied nuclear physics experiments) beam line offers the possibility to focus the proton beam to a diameter of less than 1 µm FWHM in air.

The device responses due to protons look qualitatively similar to the responses caused by an x-ray micro-beam, discussed in detail in chapter 4.3. This is a strong indicator that mechanisms occurring inside the HEMT devices are equal for x-ray and particle detection. Exposure to both photons and particles results in a production of electron-hole pairs inside the GaN layer. Electrons drift to the 2DEG layer due to the electric-field caused by the hetero-junction and alter the conductivity of the device, as well as the recombination times of the electron-hole pairs. The device response does not differ if these electrons, which are collected in the 2DEG, are produced by the photo-effect or ionizations due to particle hits [How2012].

5.1 Proton flux dependence

For the following experiments, a HEMT device (wafer TG400) with a 20 µm wide and 2 mm long channel, biased with U_{SD} = 120 mV, was used. To test the device response to heavy particles, the GaN sensor was irradiated with 20 MeV protons. Irradiation was carried out in scanned line geometries, as explained in detail in the materials section and illustrated in figure 5.1.

The device current of a line irradiation with irradiation steps of ΔX = 1.05 µm and ΔY = 20 µm with a total count of 100 protons per step (see section 2.4 for details) is shown in figure 5.2. A proton flux rate of about 4800 protons per second (p+/s) sets the scanning speed of the beam to 50.4 µm/s. The total beam deflection in the X-direction was set to ±262.5 µm. Every time the beam crosses the HEMT channel, a response signal ΔI_{SD} is produced. The doublet structure is due to forward and a backward scans across the channel.

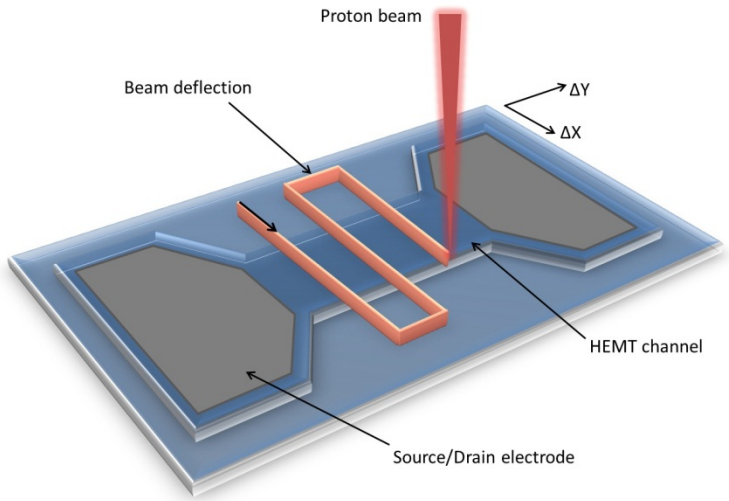

Figure 5.1: Schematic illustration of the irradiation geometry at the SNAKE accelerator. To perform line scans across the active HEMT channel, the beam is deflected by magnets in the X- and Y-directions. Beam deflection is recorded via an electrical signal to enable reconstruction of the spatialized measurements.

The signal height changes from line to line, most probably due to statistical distribution of the particle flux in combination with the relatively fast scanning speed. **It is observed that there is no baseline shift and there is only a proton response produced when the beam hits the 2DEG channel.**

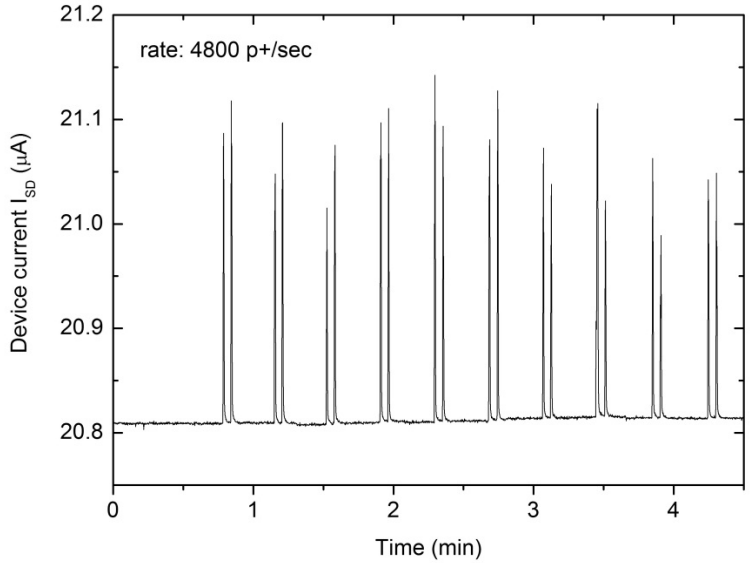

Figure 5.2: Device response of a 20 μm GaN device when the beam crosses the HEMT channel. Dual lines arise due to forward and a backward scans over the HEMT channel, whose position was off-center during the scan. The irradiation was performed at a proton impingement rate of 4.8 kHz.

Figure 5.3 shows slower line scans with a scanning speed of 6.8 µm/s and a proton rate of 6650 p+/s. Although the dimension of the response is a larger than the channel width of 20 µm caused by beam spreading, it is observed that the device response is localized to the HEMT channel. The beam changes the conductivity in the HEMT channel, while the GaN buffer layer shows no response.

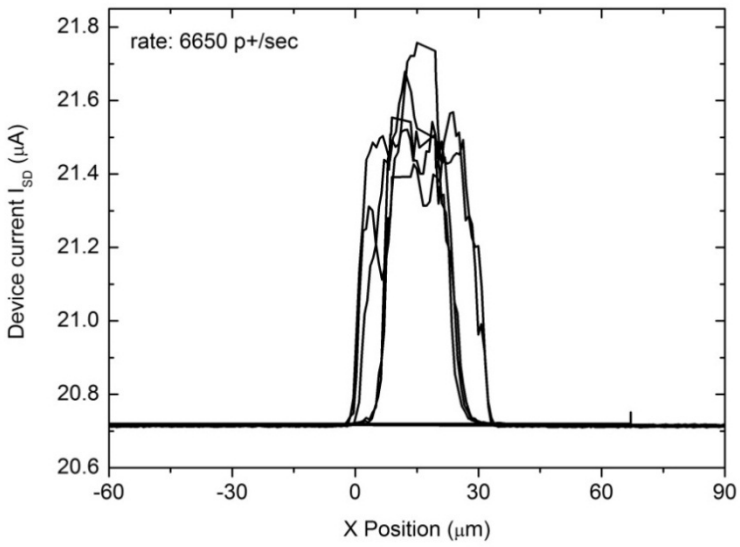

Figure 5.3: Zoom in on the device response of a 20 µm HEMT device. The irradiation was performed at a proton impingement rate of 6.65 kHz.

For investigating the correlation of the device response and the proton flux, a measurement was carried out during a continuous change of the proton impingement frequency. Therefore, the beam has been focused on the active area without a movement during the irradiation. Figure 5.4 shows the device current I_{SD} and the simultaneously measured proton rate over time.

The device current of the GaN sensor follows the proton flux between impingement rates of 0 – 10 kHz. Above a rate of 10 kHz, the device current saturates and a correlation between the signal reading of the GaN sensor and the scintillator does not hold. As for the x-ray irradiations of the GaN buffer layer, the device response saturates for high dose rates and the sensitivity to protons decreases. Nevertheless, investigation of the low kHz-regime reveals an excellent agreement between the device response and the proton rate, as shown in figure 5.5, and even small fluctuations are resolvable.

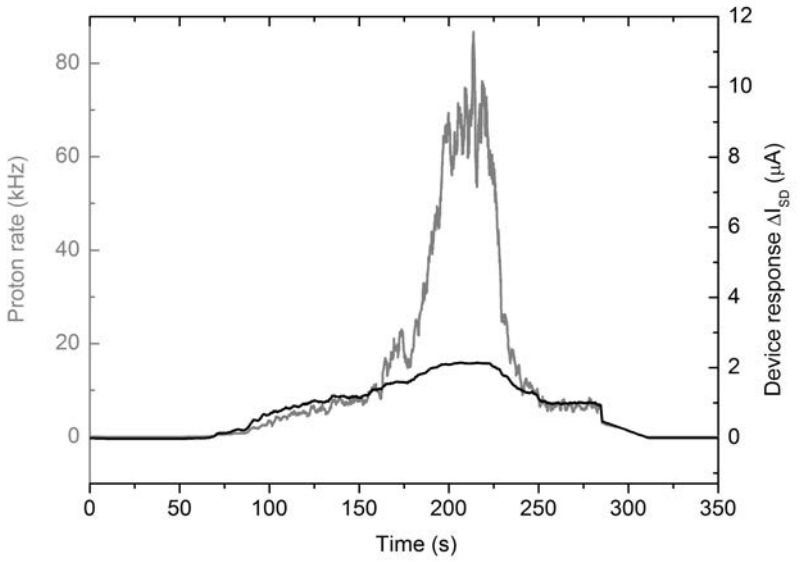

Figure 5.4: Direct comparison of the count rate of the scintillator, operated at the SNAKE set-up, and the device response ΔI_{SD} of a HEMT sample. The proton rate is manually altered. While there is a correlation for a proton rate < 10 kHz observable, the GaN sample could not follow for higher proton rates.

It is necessary to emphasize that the devices are not optimized for proton measurements. A further adaption of the HEMT sensors could improve the ion sensitivity and enhance the regime of operation. One method of device adjustment is the application of an external gate potential, which will be discussed in the following chapter.

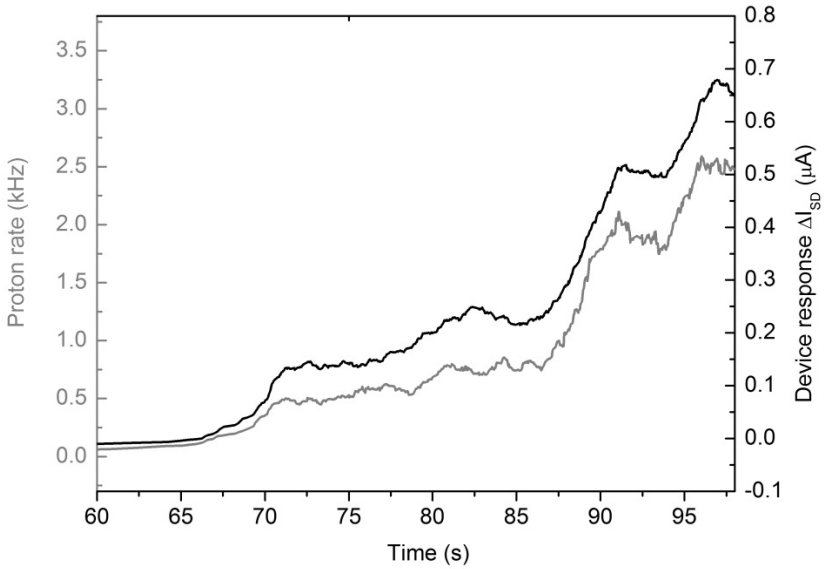

Figure 5.5: Zoom in on the measurement shown in figure 3.60. While the HEMT device could not follow the signal at proton rates > 10 kHz, good correlation for lower proton rates is observed.

5.2 Proton response of gated devices

To test the influence of the gate potential on the ion response, a GaN device with a 500 µm HEMT channel was investigated. For the used device, a sputtered 100 nm SiO_2 layer on the active HEMT area insulates the used Ti/Al gate electrode from the channel. The characterization of I_{SD} with V_G is comparable to electrolyte gated devices and given in figure 5.6 (a). The device response, shown in figure 5.6 (b), is given by plotting the current change ΔI_{SD} caused by a proton beam with a particle rate of 14.2 kHz for different gate potentials V_G. As mentioned in the introduction of this section, the device response for protons looks qualitatively similar to the HEMT irradiations with the synchrotron source.

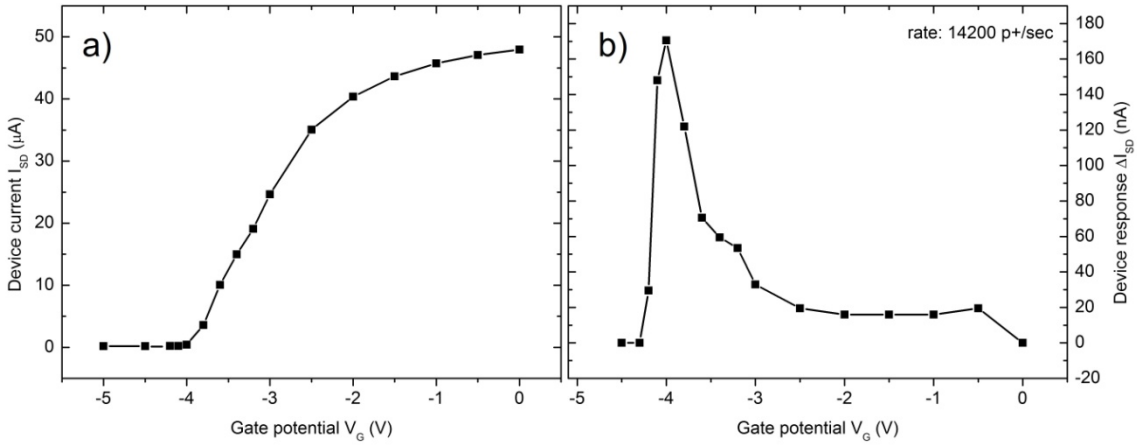

Figure 5.6: (**a**) shows the typical device transfer characteristic of a HEMT sample. The gate potential V_G is applied with a Ti/Al metal electrode. (**b**) shows the corresponding device response to proton irradiation as a function of V_G. The device shows a response comparable to that produced with an x-ray microbeam, as presented in detail in chapter 4.3.

Figure 5.7 shows the device current I_{SD} of a forward and backward scan when the proton beam hits the 2DEG channel at gate voltages V_G near the threshold voltage. While the persistent current of about 0.25 µA changes only slightly for different gate voltages V_G, the HEMT response is radically different. At a gate potential of -4.0 V, the device shows the highest amplification and a sharp transient edge when the beam passes from the buffer layer to the HEMT channel. At a gate potential of -4.1 V the amplification becomes smaller and the transient edge smears out, which is an indicator that boundary effects due to bending of the energy bands at the HEMT border plays an important role for signal amplification. This is also consistent with the observation that a 20 µm wide HEMT channel shows a HEMT response at zero gate potential, while the 500 µm channels yield no response at this potential. Due to boundary effects at the HEMT border, the whole 20 µm HEMT channel is energetically aligned for effective sensitivity, unlike the 500 µm channel. At a gate potential of -4.2 V the response is nearly quenched, though there is still a small increase in source-drain current I_{SD} observable.

The current I_{SD} changes slightly with the beam position. This supports the finding that the energetic bands are not constant along the HEMT width and the amplification correlates with the internal electric field at the given gate voltage.

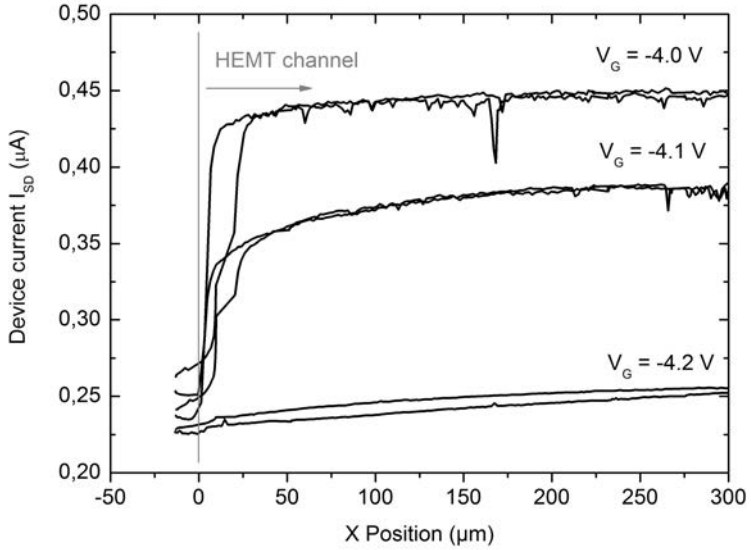

Figure 5.7: Spatial resolved proton response of a HEMT channel. For every gate voltage V_G a forward and a backward scan is given. Beside the change of the total signal height at different gate potentials, the plot reveals a signal alteration at the boundary of the HEMT mesa structure.

6 Towards a GaN based biosensor for radiation experiments

This chapter focuses on measurements of physiological parameters with GaN-HEMT devices. Therefore, the sensors are evaluated regarding their applicability for surface potential measurements during an exposure to a radiation field, related backscattering effects and their biocompatibility and biofunctionality. Although real signal measurements with biological material are beyond the scope of this work and are not shown here, the presented experiments highlight the potential of the devices regarding future biosensing applications.

6.1 Combined surface potential and radiation measurements

As shown in chapter 3, devices consisting of a single GaN buffer layer are utilized for pure radiation measurements. For experiments presented in this chapter, the sensors are equipped with a HEMT structure and a 2DEG which provides the possibility of altering the conductivity of the devices via an external gate. The external gate can be either realized with an electrolyte which is in direct contact with the sensor surface or an electrical metal contact which is located on the HEMT channel. In this chapter, measurements with an electrolyte are described. Sensors with metal gates are used in chapter 4 and described there. The overall performance of the sensors is independent of whether the gate potential is applied with an electrolyte or a metal pad. Measurements in fluids are accomplished by isolating the electrical source-drain contact from the fluid while the active HEMT area is in direct contact with an electrolyte. It is necessary to differentiate between three different kinds of measurements:

1) The HEMT channel of the sensors is sensitive to **surface potential** alterations, as for example pH value changes. The set-up is described in section 2.6.3. The GaN-sensor acts as a working electrode in a three electrode setup with control by a potentiostat. The potential V_G of the surface gate is adjusted against an Ag/AgCl reference electrode. The pH response of GaN-HEMTs has been described in previous publications [Stei2003, Pod2010].

2) Measurements of **radiation doses** inside of a fluid are performed as described in chapter 3, but now, with isolated electrical contacts. No additional adaption of the measurement set-up is necessary. This chapter clarifies if the direct contact of the sensor surface to a fluid has an influence concerning dose rate measurements.

3) A combination of 1) and 2): measurements of **surface potentials during radiation exposure** and vice versa, **the measurements of radiation doses during a change of the surface potential**. This allows measurements of physiological parameters, such as the pH-value, during irradiation experiments. The aim is to combine biosensing capabilities with irradiation experiments. Therefore, it needs to be determined if the exposure to radiation has an impact on surface potential sensitivity, since non-linear mechanisms due to saturation effects of the device current are conceivable.

6.1.1 ISFET operation

The HEMT devices can be operated as ion sensitive field effect transistors (ISFETs) since their 2DEG channels show a high sensitivity to surface potentials. Figure 6.1 shows a typical characterization curve of a GaN-HEMT with a channel width of 400 µm operated in an electrolyte with 10 mM HEPES buffer and 0.1 M NaCl. An external gate voltage V_G is applied between an Ag/AgCl reference electrode in the electrolyte and the source contact, which causes a potential drop on the device surface. Five repetitions of the cyclic change of the gate voltage V_G reveals a hysteresis of the curve which is shown in figure 6.1. For characterization plots presented in this chapter the mean value of cyclic measurements of the device current I_{SD} is calculated and shown. Although the hysteresis is clearly observable for a full transistor characterization, it plays no role for real measurements since the gate potential is not varied over the full range but only in the mV regime. The GaN-HEMT used for the measurement in figure 6.1 blocks the source drain current I_{SD} almost completely at a gate voltage of -3 V. Tests with different devices revealed a strong dependence of the cutoff voltage V_{cutoff} on the composition of the wafer structure and processing of the HEMT channel and electrical contacts. The residual current occurring in the cutoff region can be either caused by a remaining excitation of the GaN layers, for example by light, or a residual conduction through the buffer layer.

Experiments in chapter 3 have shown that the conductivity of the devices is not only provided by the HEMT channel but also by the GaN buffer layers. It is possible to produce devices with a zero residual in the cutoff region by using highly resistive buffer layers of high quality.

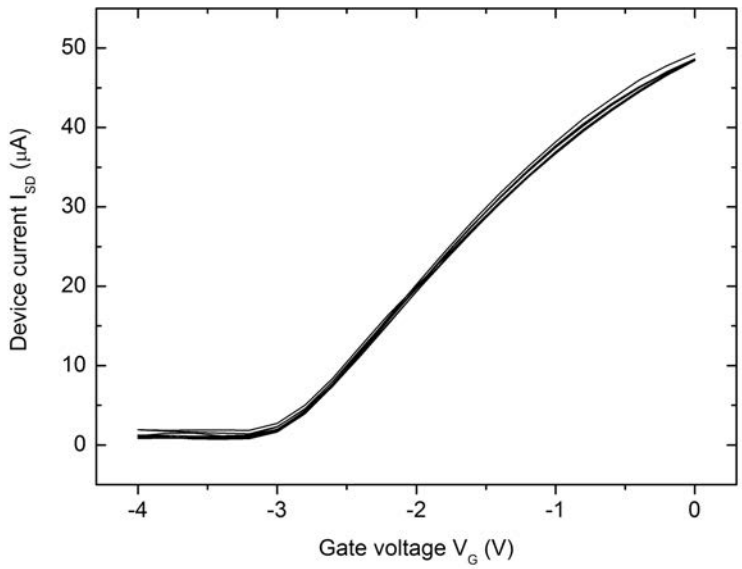

Figure 6.1: Cyclic characterization of a GaN-HEMT. The plot shows the source-drain current I_{SD} as a function of the gate potential V_G, which is applied via the front gate, the electrolyte. A small hysteresis is observed.

To gain the surface charge level per pH, the source-drain current, I_{SD}, was kept constant by compensating the gate potential with a computer control at a constant source-drain voltage of 120 mV. The electrolyte was titrated with NaOH and HCl diluted with buffer. Automated pumps were utilized which titrated 0.5 ml of acid or base inside the electrochemical cell in 5 min intervals. The regulated changes of V_G and the simultaneous reading of a pH electrode are plotted in figure 6.2. The linear relationship of the gate voltage V_G and the pH has been reported by Steinhoff *et al.* and was determined at 56 mV/pH [Ste2003a]. Due to the use of different devices and a different set-up, the sensitivity shown in figure 6.2 is 40 mV/pH. All experiments were performed in a completely darkened environment due to the light sensitivity of the transistors.

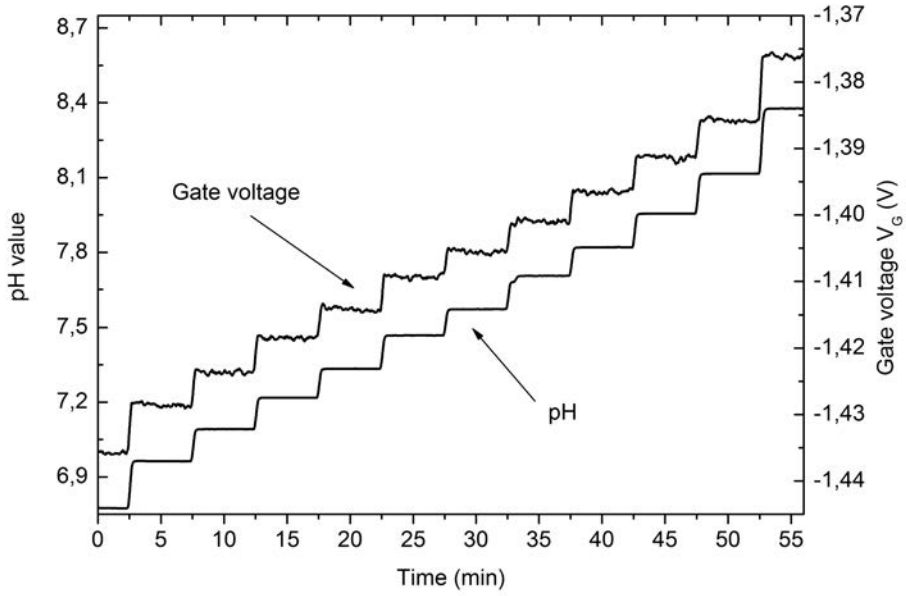

Figure 6.2: Direct comparison of the measurement of a pH meter (pH-meter 780, Metrohm, Germany) and the gate voltage V_G of the HEMT device during a titration experiment. NaOH is titrated in 5 min intervals into the buffer solution, which is in direct contact with the active area.

Figure 6.3 illustrates full characterizations of a GaN-HEMT device with an electrolyte titrated to pH 4, 7 and 10. It is observed that the change of the gate potential due to the different buffer solutions must be compensated by a shift of the gate voltage V_G and the overall curve progression is preserved for the different pH. The aim of these experiments is to investigate the sensitivity and stability of the HEMT devices for the measurement of physiological parameters such as the pH or ion concentrations. The following sub-chapter focuses on the combination of measurements of physiological parameters during irradiation experiments.

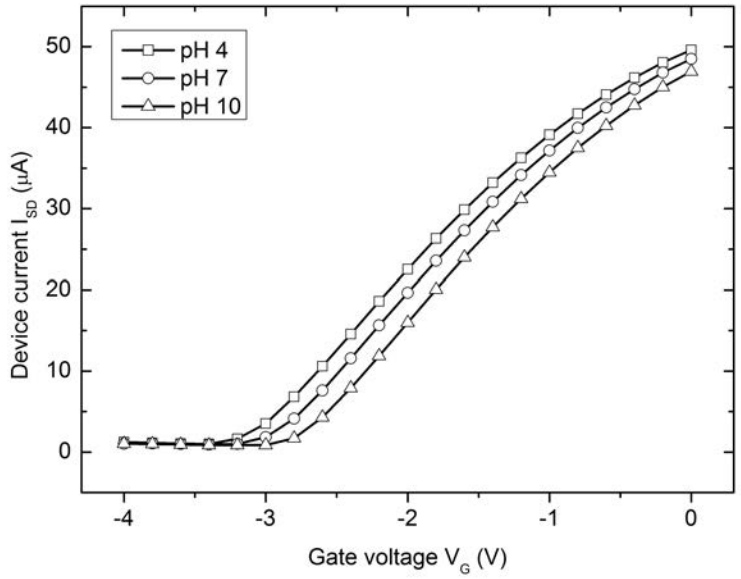

Figure 6.3: Device characterization at different pH levels, exposed to the HEMT area. The different proton concentrations on the device surface results in a shift of the gate potential V_G.

6.1.2 ISFET response during x-ray irradiation

The question which is discussed in this chapter is: do the HEMT devices work during exposure to x-rays and, moreover, is a simultaneous measurement of both surface potential and x-ray photons possible? This question can be simply answered by evaluating figure 6.4. While the exposure to x-rays shifts the characteristic curve of the device, the overall behavior is preserved. Since the sensitivity to the surface potential is determined by the slope of the curve, which does not change with irradiation, there is no alteration of the sensing characteristics. The shift of the curve is caused by the radiation response of the GaN buffer layer which has been investigated in detail in chapter 3. Also saturation is observed in the measurement since the line shift decreases with increasing dose rate. For surface potential measurements, this shift must be corrected. Nevertheless, figure 6.4 shows that a potential measurement during illumination is possible since the sensitivity is preserved.

In addition to these findings, figure 6.4 also reveals a nearly independent detection of x-ray photons related to the gate voltage V_G. The curves show an almost parallel progression and therefore the radiation response ΔI_{SD} is constant for any external gate potential. This fact allows combined measurements regarding x-ray dosimetry and physiological parameters: **The surface potential does not influence the radiation sensitivity and vice versa.**

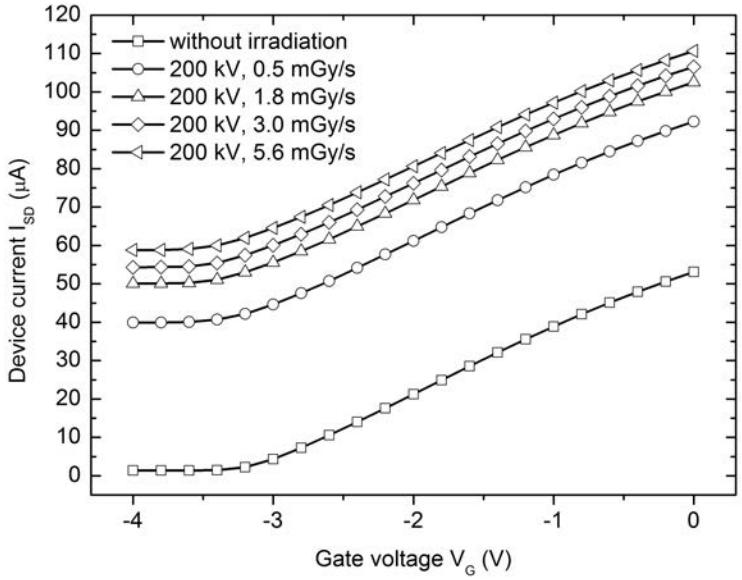

Figure 6.4: Device characterization at different air kerma rates. The exposure of the device to an external radiation field results in a shift of the source-drain current I_{SD}.

In figure 6.5, combinations of both parameter alterations are plotted, including a change of the pH from 4 to 10 and exposure to x-ray radiation. The transistor was characterized at pH 4 and pH 10, before, during, and after x-ray irradiation with a dose rate of 2.9 mGy/s at 150 kV. The GaN buffer layer shows a lower radiation response compared to the irradiations shown in figure 6.5 since a larger electrochemical cell was used for these experiments. The liquid column on top of the sensor, with a height of about 5 cm, leads to attenuation due to x-ray absorption. Therefore, a lower response is expected.

A titration experiment during a continuous x-ray irradiation was carried out to test the findings of this chapter in an experiment simulating real conditions. Again, two computer controlled pumps were utilized to pump 0.5 ml NaOH or HCl diluted with buffer into the electrochemical cell. The pH value of the solution was recorded with an external pH-meter (pH-Meter 780, Deutsche Metrohm, Filderstadt, Germany). In contrast to the pH titration in the previous chapter, the surface potential change of the HEMT during a continuous irradiation with 150 kV x-rays at an air kerma rate of 1.4 mGy/s was recorded. Again, the device current I_{SD} was kept at a constant level by a computer regulation of the gate voltage V_G, which compensates the surface potential of the device. Intention of this method is to provide a direct readout of surface potential changes, beside the reduction of internal temperature effects. The experiment yields a pH sensitivity of 57 mV/pH during x-ray irradiation, shown in figure 6.6. The inset illustrates a section of the measured gate voltage V_G at different pH-values, titrated in 3 min intervals.

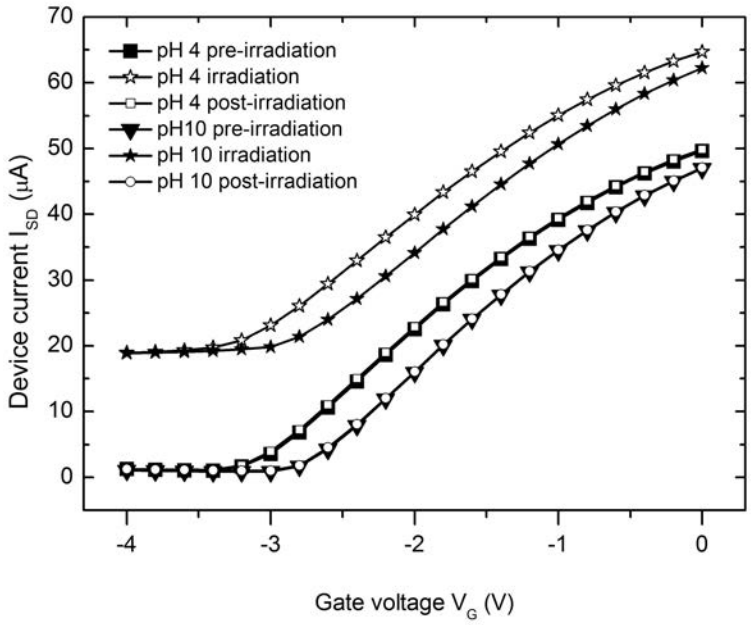

Figure 6.5: Characteristic curves of a GaN-device in solution before, during, and after irradiation with a dose-rate of 2.9 mGy/s at pH 4 and pH 10. The plots show a combination of both the change of pH and the change of the external x-ray field. To achieve equilibrium, V_G was first cycled between 0 V and -4 V five times. The plotted data were then obtained by averaging of five consecutive cycles per data series.

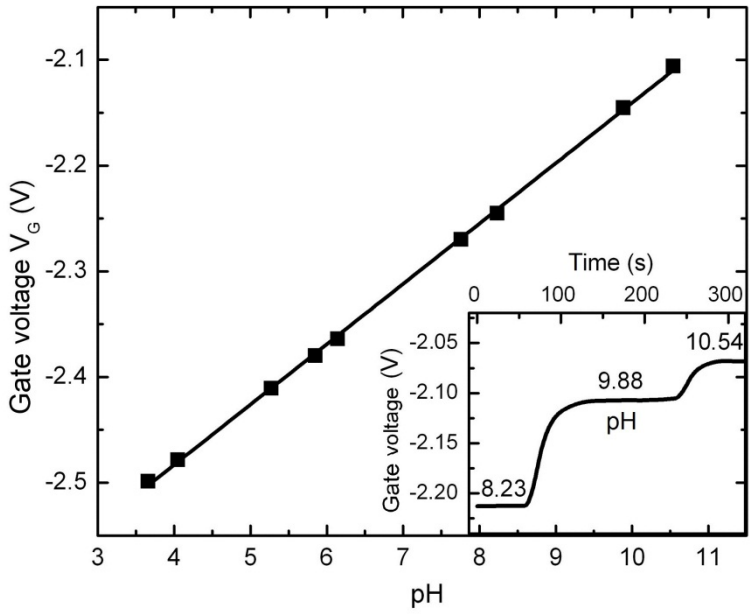

Figure 6.6: Titration during a continuous irradiation with a dose-rate of 1.4 mGy/s. The slope of the linear pH response yields a transistor sensitivity of 57 mV/pH. The inset illustrates a section of the measured gate voltage V_G at different titrated pH-values. Continuous irradiation was performed with 150 kV x-rays.

While all previous experiments in this chapter were carried out with transistors with active channel widths of 400 µm, figure 6.7 shows a characterization of a device with a narrow channel. The output characteristic of a HEMT device with a 30 µm wide channel (wafer TG400, see chapter 2.1 for details) is measured, with and without irradiation. A strong alteration of the output characteristic is possible since band bending mechanisms at the borders of the HEMT area play a comparatively large role for devices with such small mesa structures. The result of the measurements is illustrated in figure 6.7. Although the cutoff voltage V_{cutoff} is different from the larger structures the overall output characteristic is preserved. The device also shows responsivity to the surface potential and figure 6.7 reveals the expected response to radiation with 150 kV x-rays at an air kerma rate of 3.3 mGy/s. The residual current below V_{cutoff} for the irradiated sample is a consequence of excited states due to x-ray interactions and observed for all samples, independent of channel width. The curvature near the zero gate potential is an artificial measurement effect due to fast changes of V_G from -9 V to 0 V.

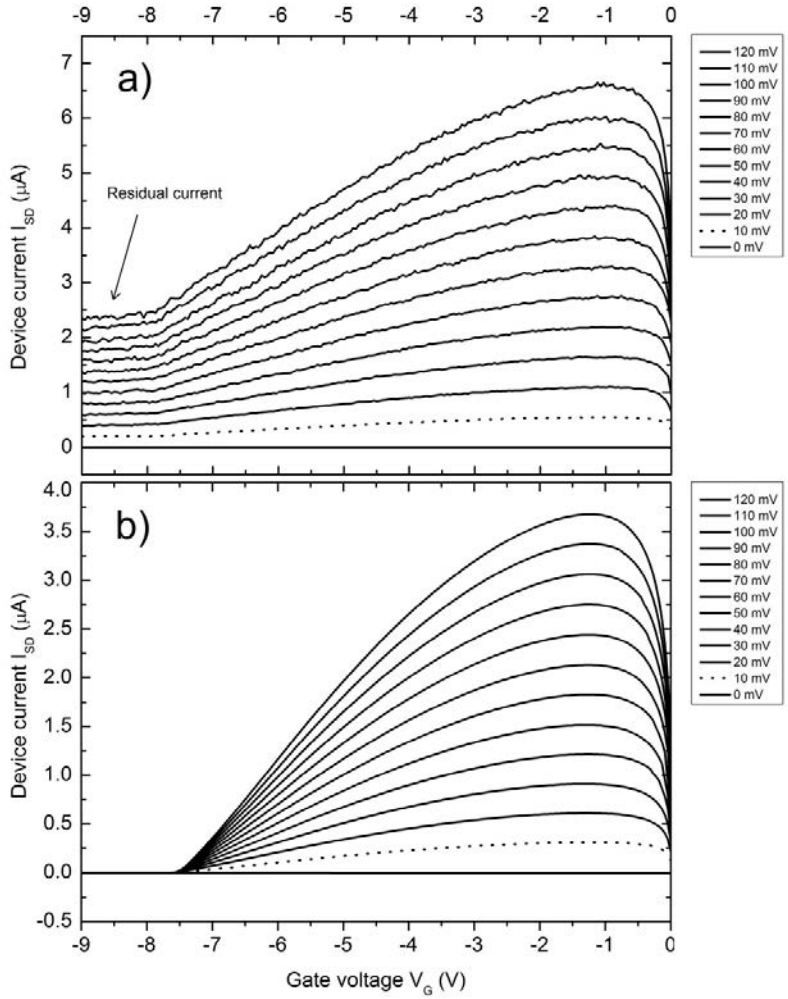

Figure 6.7: Characterization of a HEMT device with a 30 µm channel and 30 µm contacts. **(a)** shows the measurement during a continuous irradiation with 150 kV x-rays at a dose rate of 3.3 mGy/s and **(b)** without x-ray radiation. The low threshold voltage (~ -7.5 V) is a result of a different wafer structure (wafer TG400).

In conclusion, GaN HEMT devices, configured as ISFETs operating in electrolytes, retain their pH sensitivity during x-ray irradiation in a stable and reproducible manner. Moreover, the findings suggest that the fundamental device characteristics could be utilized for separating the irradiation signal from the pH response without compromising the operational stability of the device. The reproducible enhancement of the source-drain current with x-ray dose rate further provides an internal calibration for the received photon flux under aqueous solutions and establishes that such devices are well suited for combined hard radiation and ion-sensitive measurements in a range of harsh environments. They are thus ideally suited for future integrated radiation dosimetry and bio-sensing medical applications.

6.1.3 Transconductance

The transconductance is a parameter which is used to describe a typical characteristic of an electronic device such as an amplifier. Transconductance g is the ratio of the current change ΔI at the output of a device to the voltage change ΔV at its input. Therefore, the transconductance is defined by following equation and has the unit siemens (S), which is the reciprocal of the unit ohms (Ω).

$$g = \frac{\Delta I_{output}}{\Delta U_{input}} \quad \left(S = \frac{1}{\Omega}\right) \tag{6.1}$$

The transconductance of the HEMT devices can be simply derived by calculating the first derivative of the control characteristic I_{SD} over V_G.

$$g = \frac{\Delta I_{SD}}{\Delta V_G} = \frac{\mathrm{d}I_{SD}}{\mathrm{d}V_G} \tag{6.2}$$

The aim of calculating the transconductance for HEMT devices is to show that a change of the control characteristic during an exposure to radiation does not describe the mechanism completely. Due to x-ray irradiation, there are small variations in curve progression of the control characteristic, I_{SD} over V_G, and shifted curves are not aligned perfectly parallel. These variations are so small that they are not noticeable in the I_{SD} over V_G plots (see figure 6.4) but have an effect when evaluating the transconductance. Since measurements of surface potentials usually occur in the mV-regime, these small variations which affect the entire control characteristic are negligible. Perfectly parallel curves would result in an equal transconductance, which is not the case for transconductance curves of a GaN HEMT during an exposure to different dose rates. Figure 6.8 shows a change of the surface pH which shifts the sensitivity maximum of the device and therefore the transconductance. The sensitivity maximum is defined in equation 6.3.

$$\frac{d^2 I_{SD}}{dV_G^2} = 0 \Rightarrow g = extr. \tag{6.3}$$

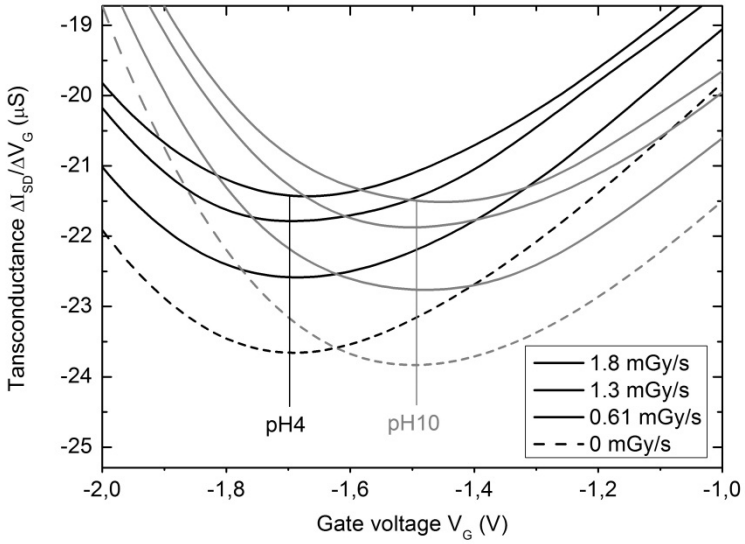

Figure 6.8: Transconductance of a HEMT device. While the pH shifts the gate voltage V_G, a change of the kerma rate results in a shift of the transconductance maximum. Therefore, the device response ΔI_{SD} to radiation is not completely constant with the gate potential V_G. For normal operation this behavior is negligible.

The alteration of the transconductance is a source of error when combining surface potential measurements with radiation experiments. However, for normal operation the error is negligible. On the other hand, the alteration of the transconductance provides the possibility to perform combined surface potential and radiation measurements which are independent from each other. As discussed in the previous chapters, a combined measurement of the surface potential and radiation dose is possible but, since only a single measurand (I_{SD} or V_G) is recorded with the HEMT devices, one parameter must either be held at a constant value or needs to be known. The evaluation of the transconductance over V_G provides two parameters: the shift of the extremum of g in the X-direction, which represents a pH change, and the shift of the extremum of g in the Y-direction, which represents a change of radiation intensity. Therefore, simultaneous measurements of both parameters become possible. In other words: The evaluation of the transconductance extremum provides two-dimensional information which is necessary to resolve two parameters simultaneously.

These experiments have shown that the HEMT devices are well suited for multi-parameter measurements regarding radiation responses and surface potentials. The sensors could be used for combined measurements and, especially for biological irradiation experiments, the devices are suitable for use in a broad range of applications.

6.2 Backscattering effects of GaN

As discussed in the introduction section, the interaction of x-rays with matter is dominated by the photoelectric effect in the applied energy range. In this process, energy is absorbed from the x-ray photons which results in an emission of electrons. When released electrons possess higher energy than the electron affinity of the material they are able to leave the material. The so called production of free secondary electrons due to ionizing radiation is a well-known process and increases dramatically with the atomic number Z of the scattering material, which is higher for gallium (Z=31) than for silicon (Z=14) in glass. The cross section of the photoelectric effect σ_{Ph} depends on the atomic number Z and the photon energy E, whereas n is about 4 for photon energies in the 100 kV regime [Rus2007].

$$\sigma_{Ph} \propto \frac{Z^n}{E^3} \tag{6.4}$$

The additional dose caused by absorption of secondary electrons produced in surrounding materials adds to the dose which is directly absorbed in a sample. Since in this work GaN-HEMTs are characterized for possible measurements of physiological parameters and biosensor applications in combination with radiation experiments, a determination of dose enhancement on the sensor surface is of high interest. Experiments and calculations in this chapter reveals that the dose rate on the sensor surface is at least doubled compared to glass surface substrates.

6.2.1 Dose enhancement

Since there are no dosimeters available which are able to measure backscattering effects very close to material surfaces (µm range) the induction of DNA double strand breaks (DSBs) to eukaryotic cells is utilized for dosimetry purposes. 53PB1, human p53 binding protein, localizes at the DSBs and is labeled with a fluorescence antibody (Alexa Fluor 488, Invitrogen, Germany). The number of double strand breaks and therefore the fluorescence intensity is linear with the absorbed dose in the investigated regime [Asa2009]. Fluorescence evaluation of the foci provides information on the initially applied dose. Instead of using the evaluation of double strand breaks for estimating health effects, bio-dosimetry with cells can provide a sophisticated tool for material characterization. Single cells have a volume of about several picoliter and therefore cells can be used for dosimetry purposes with a spatial resolution unmatched by technical devices. By comparing reference and sham irradiations of cell cultures with irradiated cells in the region of interest, a highly sensitive determination of local doses is possible. The findings in this section are backed up with Monte Carlo calculations, presented in chapter 6.2.2.

A measurement of the air kerma does not provide any information of the absorbed dose by cells cultivated on the semiconductor surface. Compton scattering and the photo effect produce secondary electrons when x-ray photons traverse the material. These electrons deposit energy to the cell nuclei and are responsible for an increase in absorbed dose. By

immunostaining of DNA double strand breaks one could receive information about the absorbed energy. The shown experiments reveal the huge potential of using cells as biological radiation dosimeters by determining the local dose on high electron mobility transistors (HEMTs) based on gallium nitride.

L-929 fibroblasts were cultivated on glass and on gallium nitride to show the backscattering increase due to surface effects. Therefore, both GaN and glass surfaces are treated with fibronectin coating to promote cell growth. Irradiation, as well as staining, was performed simultaneously on gallium nitride and glass. Cells were irradiated on two different kinds of GaN wafers; a single Fe compensated GaN layer (wafer 07-535) and a HEMT structure (wafer TG401). Irradiated samples were covered with 7 mm of cell media during a 75 kV irradiation and kept at 37 °C. Results are given in figure 6.9. Although all samples were exposed to an air kerma of 100 mGy, cells on the GaN surface show about twice as many initial foci (30 min repair time) as cells on the glass surface. Sham irradiations showed that this is not a toxic effect from the surface material. In fact, the semiconductor layer structure advances internal reflection and back-scattering processes. By keeping time intervals (2h, 6h, 24h) between cell irradiation and cell fixation, DNA repair mechanisms are able to repair DNA breaks and consequently reduce the average number of foci. Therefore every data point in figure 6.9 represents a sample with 100+ fixed cells at certain repair times since staining of the DNA requires fixation of the cells. The inset in figure 6.9 shows the linear relationship of double strand breaks determined by experiment. The error bars are derived by an error propagation of the standard deviation of the linear regression and the standard deviation of the foci distribution for each data point.

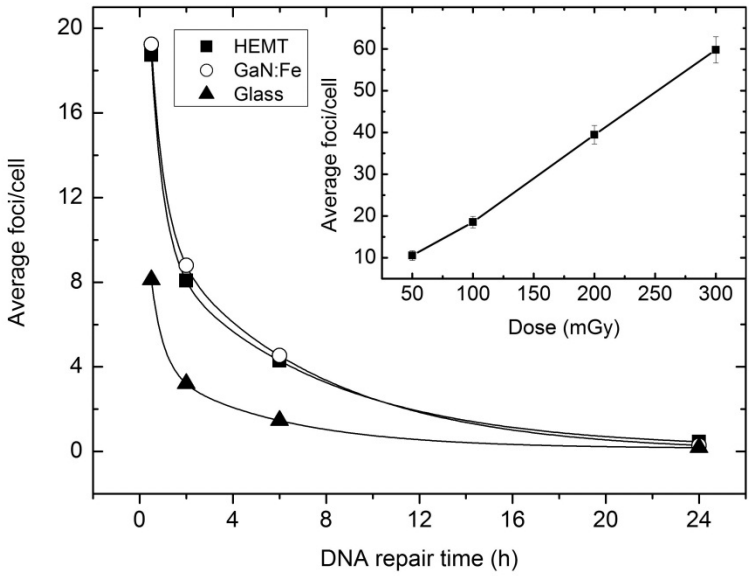

Figure 6.9: Average number of DNA double strand breaks per single cell. DNA repair time is the interval between irradiation and fixation of the cells. Due to an enhancement of secondary electrons on the GaN substrates, the initial DNA damage is higher compared to irradiated cells on glass. The inset shows the well-known linear dose-damage curve for DNA double strand breaks produces by x-rays. Each data point in the graph represents an individual experiment since staining of the DNA requires fixation of the cells.

To reveal a possible energy dependence of the dose enhancement due to back-scattered electrons, the experiment was iterated at with an x-ray acceleration voltage of 150 kV, resulting in an equal total dose of 100 mGy. The change in double-strand breaks due to the change in photon energy is negligible (not shown here) and the results appear similar to the results shown in figure 6.9. The relative increase of DNA double strand breaks from cells on a GaN surface compared to cells on a glass surface for both the 75 kV irradiation and the 150 kV irradiation is given in figure 6.10. The plots show a relative damage increase by a factor of 2-3 for cells on the GaN surface, independent of the DNA repair time. It is noticeable that the initial number of foci, after a staining time of 30 min, converges in an enhancement factor of about 2.4. For repair times > 30 min, the impact of DNA repair mechanisms becomes important and the curves diverges. Nevertheless, the enhancement factor remains between 2 and 3 for all repair intervals, which shows that temporal DNA repair is carried out relative to the initial damage.

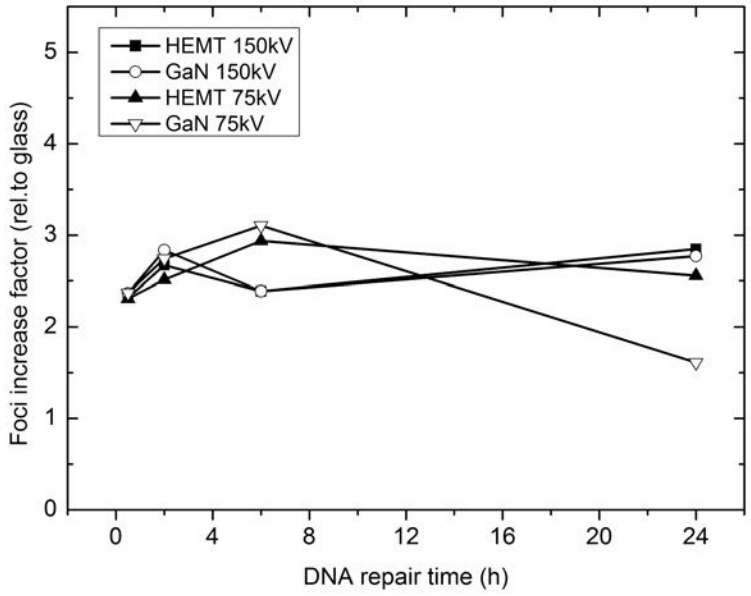

Figure 6.10: Relative increase of DNA double strand breaks of irradiated cell on GaN substrates compared to those cultivated on glassware. The data is obtained by staining of DNA breaks with antibody 53BP1.

A linear dose-DNA-damage relation in the investigated dose regime and an exponential decay of foci by DNA repair have both been published [Asa2009, Neu2012] and were also found for experiments presented in this chapter. By taking basic knowledge of DNA repair into account, the experiments presented here reveal a large dose enhancement on the sensor surface due to backscattered electrons. This is an important finding when using the devices in radiation experiments, especially in possible biosensing applications. In this chapter, the cells are used as a dosimetry tool. The biocompatibility of the devices will be evaluated in chapter 6.3.

6.2.2 Monte Carlo calculation

To verify the findings from the previous section, Monte Carlo calculations were carried out for estimation of the dose enhancement on GaN surfaces. Since experiments in chapter 6.2.1 were performed with a medical x-ray source the photons have a wide energy distribution. The photon spectrum of the x-ray source was first calculated to enable a comparison of the experiment and the simulation. Figure 6.11 shows the results for 75 kV and 150 kV x-rays from a tungsten anode with a 4.2 mm Al and a 0.1 mm Cu filtration, as used in the cell irradiation experiments. The calculations of the spectra are provided by Helmut Schlattl (group for External Dosimetry, Helmholtz Zentrum München).

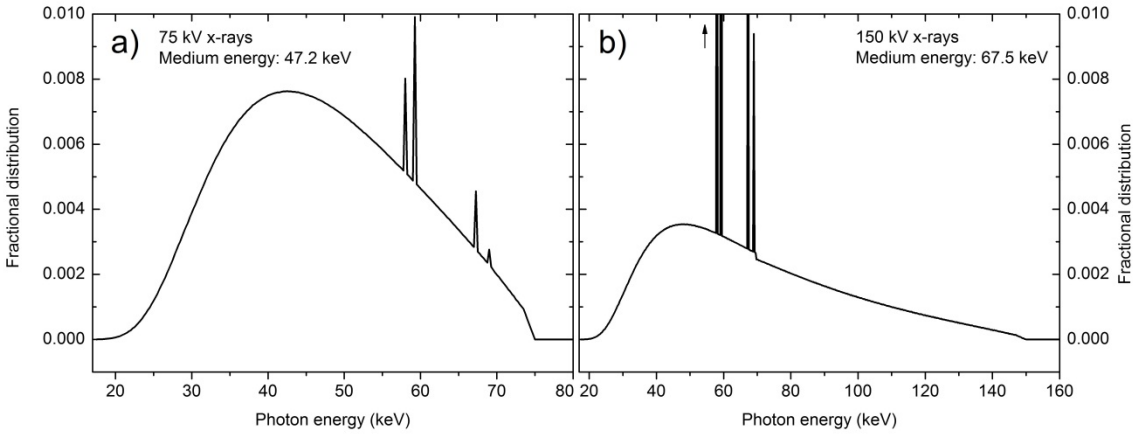

Figure 6.11: Calculated x-ray spectra produced by an x-ray tube with a tungsten anode and a 4.2 mm Al + 0.1 mm Cu pre-filtration operated at an acceleration voltage of 75 kV **(a)** and 150 kV **(b)**. The data were provided by the medical physics group for External Dosimetry at the Helmholtz Zentrum München.

The plots give the relative distribution of photons, emitted from the tungsten anode, and are normalized in such a way that the integral yields 1. It is observed that for 75 kV x-rays the intensity of the continuous Bremsstrahlung spectrum is dominant while for 150 kV x-rays high intensities due to electron shell transitions have a much larger relative contribution to the overall spectrum. The arrow in figure 6.11 indicates an extrapolation of the spectrum across the plot axis.

The energy distribution of the photons is used to calculate the relative increase in absorbed energy by Monte Carlo calculations. The calculations are provided by Christian Pioch (work group for Individual Dosimetry, Helmholtz Zentrum München) and carried out with GEANT4 v.9.3 and the standard EM-physics. The geometrical configuration of the irradiated samples is shown in figure 6.12: a 3.5 µm thick GaN layer on a 330 µm sapphire substrate is fixed on a conventional microscope slide with a thickness of 1 mm. The absorbed energy enhancement due to scattered secondary electrons for 150 kV x-rays is normalized to the average absorbed energy in water. Figure 6.12 shows the resulting calculated relative energy distribution. The

calculation clearly reveals a qualitative increase of the absorbed energy in the microscope glass slide compared to the absorbed energy in the fluid. Furthermore, an enhancement in the sapphire is distinguishable, while the GaN layer with the atomic number of Z = 31 causes locally absorbed energy enhancements up to factor 15.

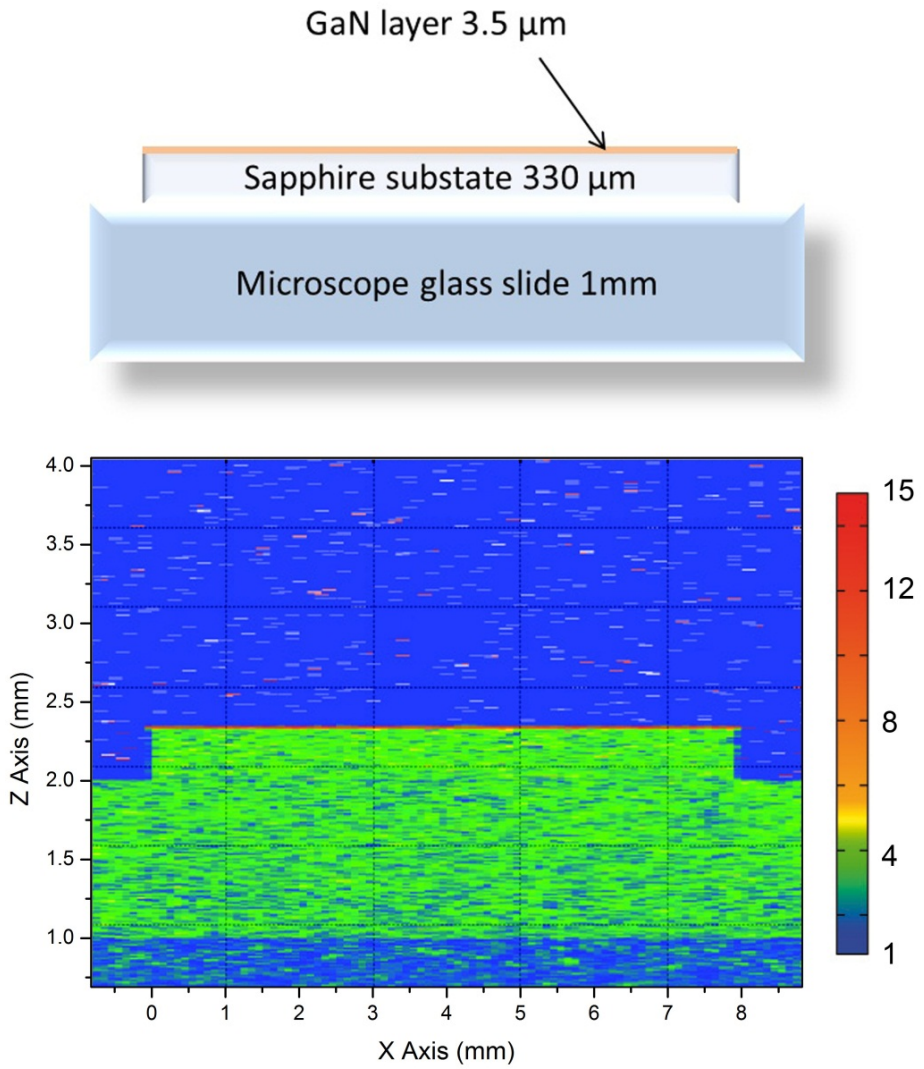

Figure 6.12: The upper part shows a schematic layout of the material arrangement for an irradiation of a GaN layer. The GaN layer is grown on a 330 µm thick sapphire substrate, which is fixed on a microscope glass slide. The lower figure shows the calculated distribution of the absorbed energy of the arrangement normalized the average absorbed energy in water.

The scoring volume defines the cubic content in which the energy transfer, and therefore, the absorbed dose are investigated. The increase in absorbed dose due to the GaN material is calculated in a 10 µm thick scoring volume on the surface. The volume represents a confluent

monolayer of cells and since living cells mainly consists of water, the density of the scoring volume is estimated by that of water. The relative dose enhancement is normalized to a calculation without a GaN sample; for a scoring volume directly on the glassware. This configuration is equivalent to the cell irradiations on the glass substrates. Figure 6.13 gives the relative dose increase in a 10 µm thick scoring volume as a function of the GaN layer thickness. For d = 0, the values are calculated for the irradiation on the glass slide without a GaN sample and without a sapphire substrate. For all other values, the given GaN layer thickness on a 330 µm sapphire substrate is calculated, although results have shown that the influence of the sapphire layer is negligible. The calculations also reveal that there is almost no difference for the 75 kV and the 150 kV irradiations. For a GaN layer thickness of 3.5 µm, as used in the irradiation experiments (wafer 07-535), the relative increase is 5.52 for 75 kV x-rays and 5.36 for 150 kV x-rays.

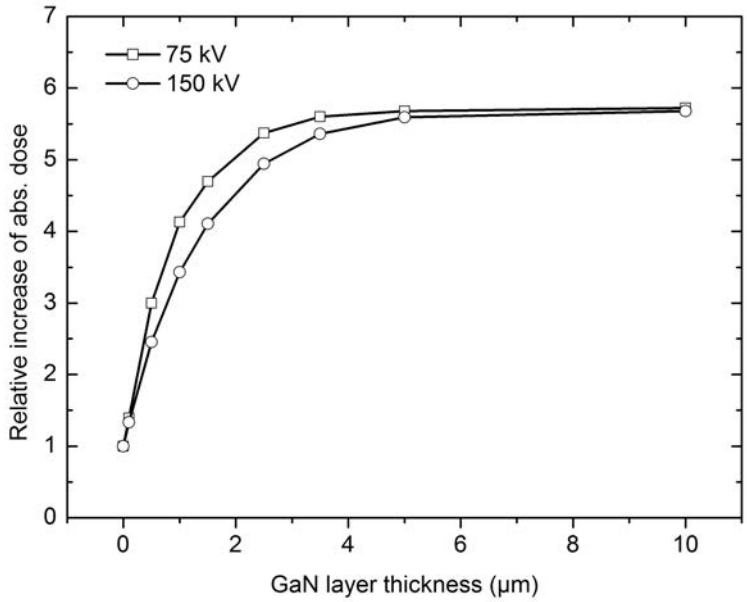

Figure 6.13: Monte Carlo calculation of dose enhancement in 10 µm thick scoring volume on top of a GaN layer as a function of the GaN layer thickness. The calculations are normalized to the zero GaN thickness calculation which corresponds to a scoring volume on a 1 mm thick glass slide. All other values are calculated for a GaN layer on a 330 µm thick sapphire substrate, in turn fixed on a 1 mm thick glass slide.

The dose enhancement factors found in the theoretical calculations are about twice as high as the dose enhancement found in the experiments. This discrepancy can be explained by several reasons, although it is important to emphasize that dealing with biological systems often contains uncertainties and the factor of 2 is not poor for such comparisons between experiment and theory which are presented above. For determination of the scoring volume an exact knowledge of the outer shape of a cell nucleus is necessary. Calculations have shown that a large fraction of energy is deposited within the sub-µm range on the sensor surface. It is unclear how large the gap between a cell nucleus and the sensor surface is and, probably most important, how large the fraction of absorbed energy is which is employed to produce DNA

breaks. Also the shielding effects of a cell membrane are unknown in these dimensions. Nevertheless, all these uncertainties support the assumption that the real deposited energy in the DNA strand is lower than determined in the calculations, as found in the experimental part of this section.

Nevertheless, although there are many unknown factors, the Monte Carlo calculations verify the experiments presented in chapter 6.2.1 and predict even higher damage. The aim of these experiments and calculations is not only to evaluate the GaN devices for possible irradiation experiments but also point out the huge discrepancy between measured air kerma doses and real absorbed doses by cells. Many publications focus on irradiation experiments of biological material but the experimental details are often insufficient. Usually, the air kerma is measured to quantify radiation damage but the impact of the substrate is often neglected. These experiments demonstrate the huge impact of secondary electrons for irradiation experiments and points out the need for a common standard regarding irradiation damage quantification and dosimetry for biological material.

6.3 GaN based biosensors

The coupling of semiconductor devices with biological material has drawn increasing interest for the analysis of intra- and extracellular signal fluxes. In recent years, advanced test platforms, such as lab-on-a-chip devices, have been developed for time resolved measurements of physiological parameters *in vitro*. While these sensors permit a variety of physical and chemical parameters to be recorded online, the biocompatibility of the sensing materials must be established. There is a pressing need for highly sensitive devices capable of detecting fast transient signals in aqueous environments, over a wide range of pH values at low voltages. In addition to microelectrode arrays, field effect transistors (FETs) have also been implemented for *in vitro* recording of physiological signals. As shown in previous publications, AlGaN/GaN high electron mobility transistors have entered a wide variety of sensing applications [Ste2003a, Ste2003b, Ste2005, Hof2010, Hof2011]. By adding a thin capping layer, which covers the chemically less stable AlGaN layer and results in GaN/AlGaN/GaN heterostructures, these devices can be rendered highly chemically inert and, thus, suitable for operation as solution gated devices that are sensitive to surface potential- and pH-changes [Ste2003a]. Furthermore, it has been determined that these devices are non-toxic to cells [Ste2003b, Cim2007]. These characteristics have enabled the successful use of GaN-based heterostructures for biosensing [Ste2003b, Ste2005, Est2008].

In order to use sensors for *in vitro* and *in vivo* detection of alterations in cell signaling processes, it is not only necessary to test the biocompatibility of the semiconductor substrates, but also to investigate the long-term biofunctionality of these surfaces. To this end, we have performed an investigation of cell proliferation and growth dynamics on differently treated gallium nitride surfaces and compared these results to glass surfaces that are often used as standard seeding environments. Since the results of this biocompatibility study proved promising, we carried out an assessment of the biofunctionality of GaN. Compared to morphological investigations or analysis of cell-survival curves, measurements of changes in cell repair provide advanced indicators for disturbed cell homeostasis. Here, DNA repair dynamics following application of external noxa to cells cultivated on GaN surfaces were used as a retrospective detection tool for cell alterations. Since DNA suffers damage from free radicals and reactive oxygen species generated by ionizing radiation [Col1995], the cell signaling was stimulated by x-rays. Organisms must trigger a series of events to promote repair of x-ray induced DNA damage in order to survive and restore chromosomal integrity [Ayl2004]. Therefore, it is possible to investigate the alterations of these events arising from material-cell interactions by recording DNA repair dynamics of cells which are in direct contact with a foreign surface. By comparing cell repair mechanisms after the impact of external noxa on biocompatible reference materials, it is possible to exclude interactions with the substrate material or determine effects that are not detectable with morphological evaluation methods. DNA repair mechanisms occurring after radiation damage are well characterized [War1990] and are therefore suitable for investigations on bio-functionality.

Since GaN devices operated as ISFETs have found use in several biosensing applications and investigations in this work revealed their usefulness for radiation experiments, a detailed characterization of the devices regarding biocompatibility and biofunctionality has been

carried out, with the main focus on irradiation experiments. The results are presented in the following sections.

6.3.1 Biocompatibility

In order to investigate the bio-functionality of GaN surfaces it is first necessary to verify the degree of biocompatibility of the material. To this end, GaN surfaces coated with fibronectin, which is well known to provide superb properties for cell growth, were compared to oxygen terminated GaN surfaces, as well as amino-terminated molecular layers covalently bound to GaN. Silanized surfaces are known to provide higher biocompatibility on similar surfaces [Mah2011] and could provide enhancements for biosensing applications. Cell adhesion and morphology were investigated by optical microscopy, which showed that confluent layers typically formed within one day. To gain the highest contrast for comparison, we therefore show the results from within the first 24 h.

Cell cultivations were performed on GaN surfaces that had been cleaned to ensure that they were sterile and had comparable surface terminations. The final concentrations of L-929 fibroblasts were between 250 and 550 cells/mm^2 on all surfaces. Optical micrographs were obtained at intervals of 4 h, 6 h, and 24 h following cell seeding, as presented in Figure 6.14. The cell proliferation and growth dynamics were compared on n-type Si doped substrates and n-type Mg compensated substrates. For both types of GaN substrates, oxygen terminated, fibronectin coated, and APS functionalized surfaces were evaluated. As shown in Fig. 6.14, the cells began to adhere to the surface and show their typical spindle like outer shape within the first 4 h. In fact, on fibronectin coated GaN surfaces, cell adhesion was observable only 1 h after cell seeding (data not shown). After 6 hours of cell growth, visible variations in cell morphology can still be observed. However, after 24 hours there was a well-defined confluent monolayer of cells observed on all surfaces. The APS functionalized GaN, which provides a fully synthetic, non-buffering, and biocompatible sensor coating [How2010], showed no significant degradation or enhancement compared to untreated surfaces; the cells exhibited their typical spindle-like shape after 4 h. This indicates that APS-cell interactions are dominated by surface morphology and that biochemical effects play a minor role compared to fibronectin coatings, which have a thickness a few nm [Gue2000]. This conclusion is supported by the finding that only minor surface roughness changes are caused by the organosilane molecules, as determined by AFM measurements on the modified GaN surfaces. Nevertheless, silanized surfaces can be an advantage for specific sensing applications, in which the layer provides the possibility for attachment of complex biomolecules, such as DNA [Ber2006] or proteins [Sch2008, Klo2007, Moh2011], to the surface. Ten consecutive experiments showed a high reproducibility for all samples without any noticeable variations in either cell proliferation or growth dynamics. Therefore, while it is possible to enhance the early stage biocompatibility of the surfaces with proteins such as fibronectin, there are only slight variations in cell adherence after a cell growth time of 24 h.

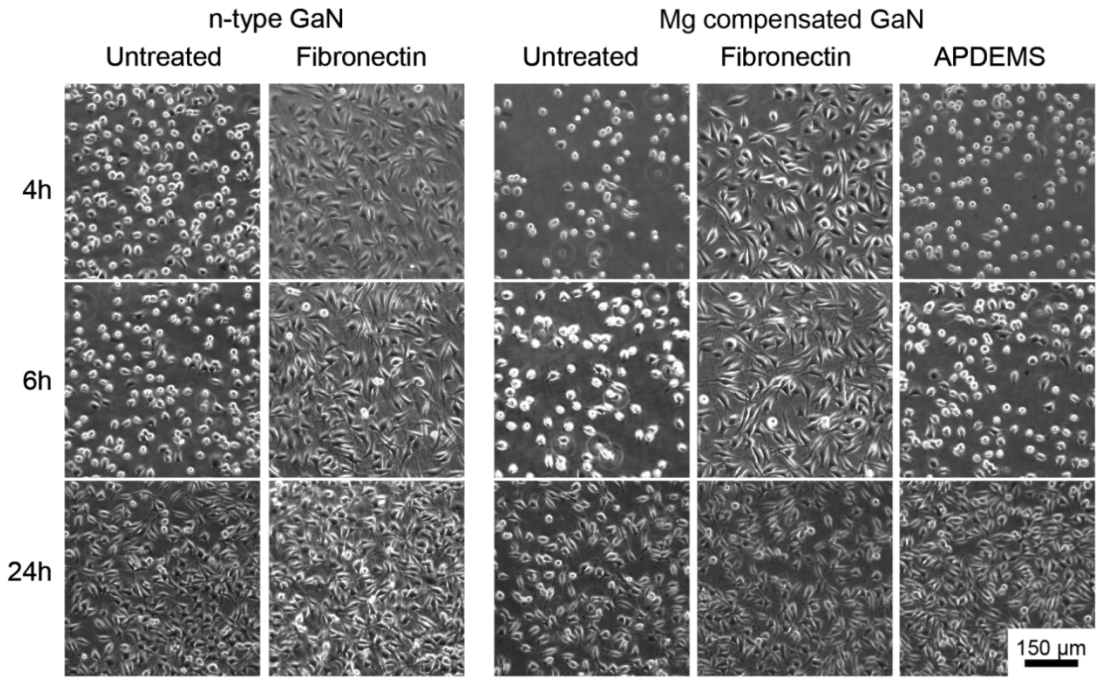

Figure 6.14: Optical comparison of cell proliferation and growth dynamics. The pictures show the difference between untreated, fibronectin coated and APS functionalized GaN surfaces for 4 h, 6 h and 24 h after cell seeding on the surfaces. Although the cells showed their typical spindle-like shape on fibronectin coated GaN after only 1 hour, all of the samples achieved the same state within 4 hours. While, after 6 hours of cell growth there are still visible variations in cell morphology, a perfect, nearly confluent, monolayer for all samples was achieved within 24 h. The images were taken at the same positions on the samples and the results were found to be highly reproducible.

When evaluating the biocompatibility of a hard inorganic interface, it is necessary to consider the termination, roughness, and chemical reactivity. Glassware, such as crystallization beakers and optical glass slides, is often used for cell seeding and is widely considered to be biocompatible. For this reason, we attempted a comparison between GaN and glass systems. Since both substrates are considered to be chemically inert and share similarly oxygen terminated surfaces, the cell proliferation and growth dynamics are expected to be, in broad terms, similar to one another if the surface roughness values are also similar. Although AFM measurements show that the rms surface roughness values of both n-type GaN and high quality glassware are approximately 1 nm in a 10×10 μm^2 area, the surface topography is significantly different, as shown in Figure 6.15. The topography difference between the microscope glass slides and GaN was so large that the oxygen terminated GaN was reproducibly better than the fibronectin coated glass slides. Therefore, we conclude that structural differences, rather than the inherent chemical properties of the two materials, were dominant and further comparison of cell growth and proliferation is not presented here.

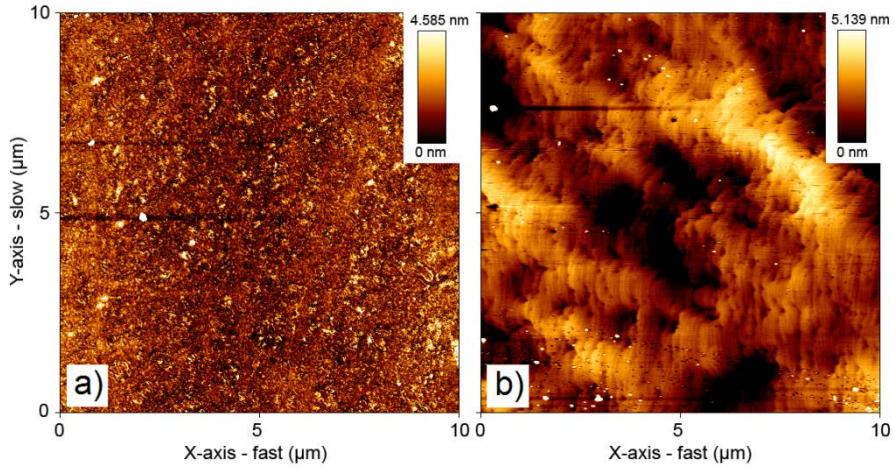

Figure 6.15: AFM images of 10 × 10 µm^2 areas on (**a**) a microscope slide glass surface and (**b**) an n-type GaN surface. The rms surface roughness of glass is 1.04 nm and the rms surface roughness of GaN is 1.17 nm in the investigated area.

6.3.2 Biofunctionality

Cellular DNA repair dynamics from x-ray induced radiation damage were obtained for cells grown on fibronectin coated gallium nitride in order to determine possible material-cell interactions. DNA repair dynamics of fibroblasts are well characterized [Rot2003] and a comparison of results from the GaN surface to reference measurements made on glass substrates, as well as previously published data, allows the testing of cell functionality. Alterations in cell repair dynamics would be an indicator for surface-cell interactions.

Cells grown on fibronectin coated GaN surfaces were irradiated with x-rays with different air kerma doses after 24 h of cell growth, and were fixed at certain repair times. DNA repair foci and cell nuclei were stained and z-stack images were recorded from the samples with a laser scanning microscope. Each stack consists of 40 cross sections through the cells, with a separation distance between successive images of 0.3 µm normal to the substrate surface. Stained DNA double strand break repair foci (green) and cell nuclei (blue) on GaN surfaces for pre- and post- 250 mGy air kerma dose irradiated samples are presented in figure 6.16 (a) and (b), respectively. A three-color staining of fixed cells on the gallium nitride surface is shown in figure 6.16 (c). The cell membrane was labeled with DiO (green), F-actin with Rhodamine Phalloidin (red), and cell nuclei with Hoechst 33342 (blue). The cell shapes and nuclei are clearly observed and show that the cells have excellent morphology. Due to the chemical tolerance and physical stability of the material, it is possible to accomplish the staining process directly on the gallium nitride surface. Moreover, the material can also be used as a substrate in confocal and laser scanning microscopy due to its transparency in the visible range, thus providing the possibility to combine electrochemical measurements with retrospective optical analysis by immunostaining.

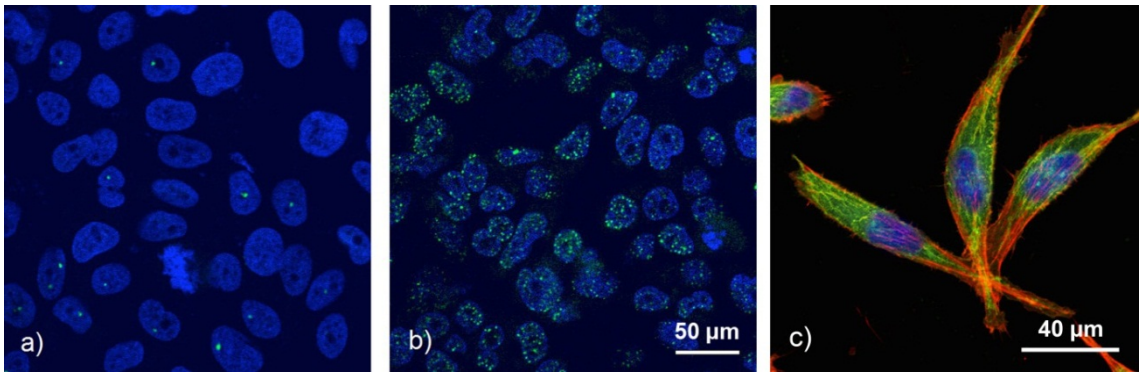

Figure 6.16: Stained DNA double strand break repair foci (green) and cell nuclei (blue) on GaN surfaces for (**a**) pre- and (**b**) post- 250 mGy air kerma irradiated samples. (**c**) Three-color staining of fixed cells showing that the cells have excellent morphology and exemplifying that the staining process can be made directly on the surfaces of the samples.

Air kerma dose (mGy)	Foci/cell (Counts) After 30 min	Foci/cell (Counts) After 2 h	Foci/cell (Counts) After 6 h	Foci/cell (Counts) After 24 h	Fitted τ value (d)
0	0.65	0.76	0.94	0.93	
10	2.49	1.56	1.31	1.02	4.06
50	7.14	5.75	2.93	2.66	7.46
100	8.52	6.69	4.48	3.10	9.44
250	16.94	11.93	9.88	5.39	11.73

Table 6.1: The average number of foci per single cell as a function of repair time for different air kerma radiation doses. The fitted τ values give the mean lifetime (1/e) from the fits of the exponential decays of the foci counts.

The numerical results of DNA repair dynamics on GaN surfaces are presented in table 6.1 and are plotted in figure 6.17 (a). Each data point represents the average of counted foci from over 200 evaluated cells. Error bars are calculated with the standard deviation of the linear regression of the dose response curve in figure 6.17 (d). Since the repair protein 53PB1 requires a certain time to accumulate at the double strand breaks, the initial data points were recorded after a delay time of 30 minutes had elapsed [And2001]. For each repair time, a sham irradiated sample, with 0 mGy irradiation, was produced in order to provide a reference for the background foci. In Figure 6.17, these background foci were subtracted and only the radiation-induced numbers are given. In comparison to the literature [Rot2003], the obtained results show that repair mechanisms are not influenced by the sensor surfaces in any significant way. After 24 h of repair time, 60% of the double strand breaks were repaired, independent of the irradiation dose. This indicates an unrestricted vitality of the cells since effective DNA repair is preserved. Furthermore, figure 6.17 (c), which is a linear-logarithmic plot of (a), reveals a single exponential decay of the repair foci, thus indicating a complete repair time of approximately 100 h. Figure 6.17 (d) gives the dose-response curve of evaluated foci. Since the total offsets of the curves are due to systematic errors in dose measurements, the offset is corrected in such a way that the fits of the curves cross the point of origin.

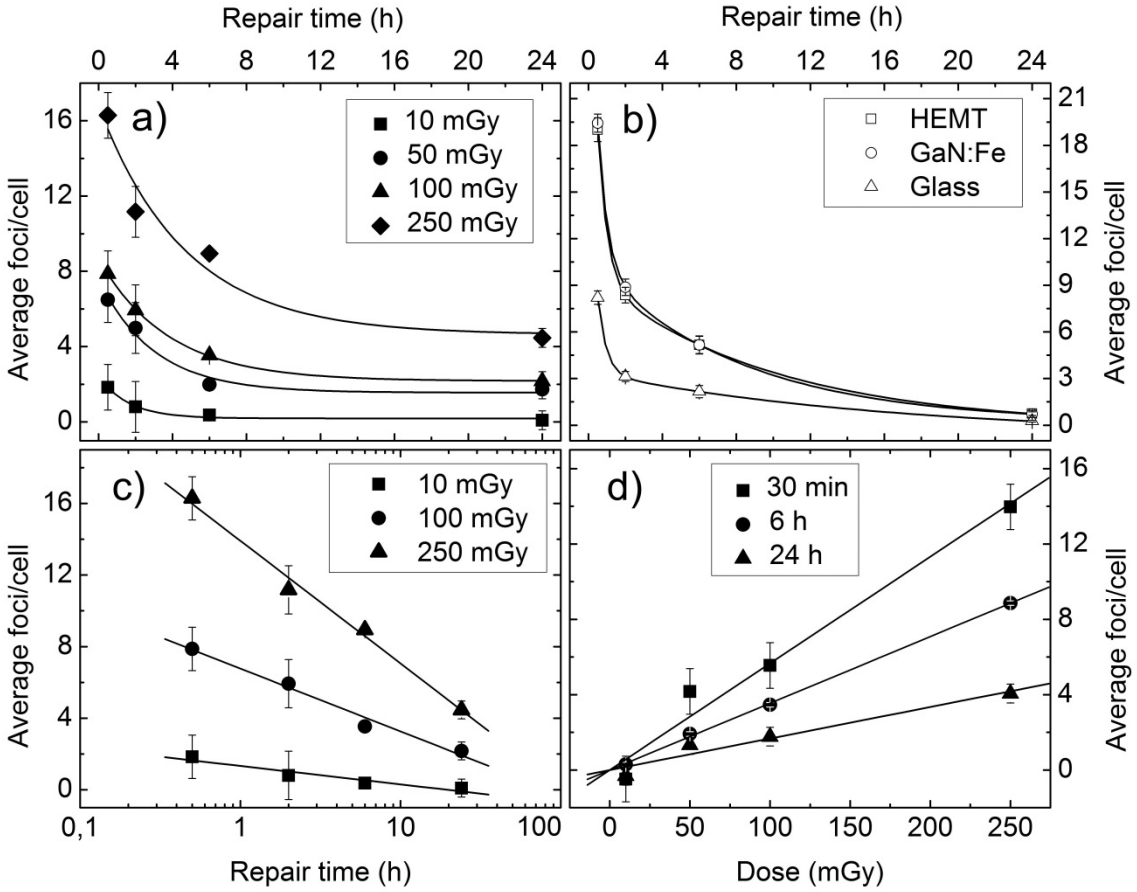

Figure 6.17: Repair dynamics of irradiated cells on a GaN and glass surfaces. (**a**) shows the exponential decay of foci counts as a function of repair time for cells seeded on a fibronectin coated GaN surface for different air kerma. (**b**) relative repair dynamic of irradiated cells (100 mGy air kerma, 150 kV x-rays) on fibronectin coated surfaces in fluid. Although cells on the GaN surface were exposed to a higher dose due to environmental x-ray interaction, differences in remaining cell damage after 24 h are negligible. (**c**) is a linear-logarithmical plot of the data from (**a**) and shows that these data have a single exponential decay. (**d**) shows the dose-response curve for the data from (**a**).

In addition, the repair dynamics between cells cultivated on GaN and glass slides, both coated with fibronectin, were compared. The samples were irradiated and stained simultaneously and every data point represents counted foci from 100 evaluated cells. In contrast to the results in figure 6.17 (a), the samples were irradiated in fluid, which leads to an increase of absorbed dose due to an additional production of secondary electrons, as can be seen in figure 6.17 (b). This also has the effect of producing a secondary exponential component in the data, which is true for both the glass and GaN. The error bars represent the standard error of the mean (SEM), since a linear regression of the curve is not applicable. We note that the error bars in figure 6.17 (b) are smaller since the SEM is calculated for each point and the model of the linear dose-response relationship is not considered for the plot. While both samples were exposed to an air kerma of 100 mGy, cells on the GaN surface showed more initial foci than the cells on the glass surface. Sham irradiations showed that this is not a toxic effect from the

material. Rather, the semiconductor layer structure advances internal reflection and back-scattering processes. The production of secondary electrons is well-known to increase with the atomic number Z of the scattering material, which is higher for gallium (Z=31) than for silicon (Z=14). Nevertheless, cells on both GaN and glass samples show a similar repair dynamic. After a repair time of 24 h, cells on the GaN sample showed 2.36 foci/cell and cells on the glass substrate 1.66 foci/cell. Considering a background of approximately 0.8 foci/cell, nearly all DNA damage is repaired and there is no significant difference in cell damage. The fitted τ_s value of the slow component of the second order exponential decay for cells on the HEMT sample is τ_s = 9.74 d and therefore comparable to the 100 mGy irradiation in figure 8.4 (a). From these experiments, we found no negative effects of GaN on cell repair dynamics.

7 Conclusion

The utilization of x-ray based techniques has been become common practice in medical procedures. New techniques require novel devices for dosimetry. In this work a device configuration based on GaN materials is demonstrated, which shows high potential for such applications. The sensors are able to overcome the previously published drawback of using GaN for dosimetry due to its limited energy absorption by utilizing very high amplification factors. The key concept is to operate the devices not as conventional semiconductor radiation detectors, which typically collect electron-hole pairs inside a space charge region, but as photoconductors with ohmic electrical contacts which allow a continuous current flow through the device. X-ray radiation alters the conductive volume of the GaN material which, in turn, alters the resistance of the device. Since alteration of the conductive area has a much higher impact on the device resistance than the production of charge carriers by x-rays [Gar1998], amplification factors in the range of 10^5 are achieved. Such large amplification factors compensate for the limited energy absorption in the small volumes of the devices. Small absorbed energies are sufficient to produce significant signals. An additional AlGaN/GaN hetero-junction forms a 2DEG which enables a further increase of amplification factors and operates at very low photon intensities (< 10^7 photons/s).

In this work, GaN thin films and GaN HEMT heterostructures were developed and evaluated regarding radiation detection and dosimetry for the first time. Compared to ionization chambers, which are considered the “gold standard” in radiation dosimetry, these GaN devices have volumes which are several orders of magnitude smaller but responses that are as good or better than ionization chambers. Here, the most important findings of this work regarding use of GaN materials for x-ray detection are summarized.

The GaN buffer layers were tested in an air kerma rate regime of 1 µGy/s – 10 mGy/s, which covers the medical diagnostic range. The devices show a linear response in terms of kerma rate up to ~0.2 mGy/s. Above this value, the device response saturates but, with an adequate calibration, measurements in the non-linear regime are also possible. The investigated kerma rate interval was primarily limited by the available irradiation equipment and is not an intrinsic limit of the devices. Therefore, it is estimated that the GaN sensors work in a much wider kerma rate range than evaluated in this work. Experiments have revealed that the device response is independent of the x-ray energy in the non-linear regime, while the signal shows an energy dependence in the linear range. It is assumed that the insensitivity to x-ray energy in the saturating regime is caused by two competing effects: the change in absorption and saturation effects in the production of electron-hole pairs.

The most significant drawback of radiation measurements with GaN buffer layers are long term transients that occur when the kerma rate is changed. While these transition times are relatively short for small kerma rate alterations, drift times of several seconds arise for switching the radiation completely on and off. In the low kerma rate regime (< 0.2 mGy/s) these drift times can last minutes or even hours. An exponential relation has been found between kerma rate and transient times. Since the sensor signal is constant with the kerma rate, the time integral of the signal yields a value which is proportional to the absorbed dose. The transient times cause an additional error for dose evaluation since they lead to deviations between the measured signal and the real kerma rate. Nevertheless, measurements have

shown that this error is only significant for short measurements (few seconds) without a pre-irradiation. For longer irradiations, or when applying a pre-irradiation pulse to bring the device in an excited state, the error becomes negligible.

Experiments revealed that the buffer response of GaN films is independent of the angle of incidence of the x-ray photons up to 60 degrees relative to the surface normal. Above an angle of 60 degrees only a slight angular dependence is observed. This behavior can be explained by geometrical considerations and is a result of the thin detection volume of the sensors.

Experiments also revealed a huge impact on sensing characteristics due to the geometry of the electrical contact pads. Although the devices profit of short distances between the electrodes, an IDT structure showed no stable response. A HEMT layer is not necessary for the measurements with the GaN devices and is also not disruptive. Only completely unstructured HEMT layers cause side effects which lead to unstable radiation signals. The presence of a HEMT layer scales the absolute radiation signal of the buffer layer but preserves the qualitative radiation response. The evaluation of these measurements revealed an interesting effect, which has an unclear origin: the absolute response of a sample with a 30 µm HEMT channel showed a smaller absolute response than a sample with a 500 µm channel and a sample without a HEMT layer. There is a configuration with a HEMT width d of $0 < d < 500$ µm which produce a minimum radiation response, likely due to lateral depletion effects. For a detailed evaluation of these effects, further work is necessary.

Due to the presence of a 2DEG channel, which is sensitive to electrical potentials, the GaN-HEMT devices could be operated as ion sensitive field effect transistors (ISFETs). This configuration allows a measurement of physiological parameters such as the pH or potentials. Experiments have shown that the HEMT devices retain their ion sensitivity during a continuous exposure to radiation and, moreover, the findings suggest that the fundamental device characteristics could be utilized for separating the irradiation signal from the pH response without compromising the operational stability of the device. The reproducible increase of the source-drain current with x-ray dose rate further provides an internal calibration for the received photon flux under aqueous solutions and establishes that such devices are well suited for combined hard radiation and ion-sensitive measurements in a range of harsh environments.

The experiments at the BESSY II synchrotron, which provided an x-ray microbeam, established the possibility to separate the radiation response of the 2DEG of a HEMT from the GaN buffer response. As mentioned above, the influence of the HEMT response is negligible for photoconductive GaN measurements since the buffer responses superimpose on the signal produced by the HEMT. However, investigation of the device response at very low photon intensities revealed a HEMT signal at intensities for which the buffer layer does not produce a signal. This allows measurements with a dose rate reduction of several orders of magnitude, which could be highly beneficial for future devices regarding patient or material diagnostics. Another advantage for measurements with the 2DEG channel is a huge decrease in the transient times. On/off drift times for switched radiation were not observed with the used measurement equipment (< 20 ms).

Proton irradiation with a tandem accelerator revealed a device response to charged radiation particles, which is not produced in the bulk GaN buffer layer but in the HEMT structure. Again,

this is the first time GaN-HEMT structures were utilized for high energy proton detection. The response characteristics were comparable to those produced with the x-ray microbeam in the 2DEG layer. Therefore it was determined that the measurement principle is based on the same physical mechanisms: amplification of the photo-current response due to an internal photovoltaic effect within the HEMT structure.

To bridge the gap between measurements of radiation doses and biosensor applications, the material is evaluated regarding backscattering effects of electrons. Breaks in DNA double strands are utilized to determine the dose enhancement on the sensor surface. Experiments yield a dose enhancement within a factor of 2-3 while Monte Carlo calculations predict a dose enhancement factor of 5-6. Although there is a difference between experiment and theory these evaluations demonstrate the substantial impact of the sensor material regarding dose enhancement. This dose increase not only plays an important role when using the devices for biosensing purposes but also for measurements with any kind of material located close to the surface.

Biocompatibility and biofunctionality studies were successfully performed on gallium nitride, which is easily adaptable to other semiconductor materials. Excellent cell growth on the sensor surfaces is observed, both with and without additional coatings, and stable and reproducible growth dynamics were achieved. Silanized surfaces with aminopropylsilane are known to provide higher biocompatibility on similar surfaces and could provide enhancements for future biosensing applications such as, for example, recognition of cellular messengers. However, surface roughness remains the primary issue for biocompatibility at these chain lengths. While DNA repair is only one out of many mechanisms involved in cell homeostasis, the temporal evaluation of DNA repair foci provides an advanced and sophisticated method for testing biofunctionality, which allows for an in depth complementary technique to qualitative analysis and morphological examinations. Here, no negative effect regarding cell functionality due to surface-cell interaction effects are found, and also no difference between GaN in comparison to glass surfaces was observed. This was an expected result and shows that this technique can be used to evaluate cell functionality due to surface-cell interaction effects, which is something cell proliferation and growth dynamics is incapable of since it is so dependent on the surface roughness. Moreover, GaN based sensors have very promising biocompatible and biofunctional properties, making them excellent candidates for highly sensitive biofunctional-sensing applications.

Appendix

A. List of materials

Lab and measurement devices

Model 2400 Series SourceMeter	*Keithley Instruments Inc.* *Cleveland, Ohio 44139, U.S.*
Model 2000 Series Multimeter	*Keithley Instruments Inc.* *Cleveland, Ohio 44139, U.S.*
Model 2700 Series Multimeter/Switch System	*Keithley Instruments Inc.* *Cleveland, Ohio 44139, U.S.*
GBIP Interface Board KPCI-488LP IEEE-488.2	*Keithley Instruments Inc.* *Cleveland, Ohio 44139, U.S.*
National Instruments NI PCI-6229 DAQ	*National Instruments* *Austin, TX 78759, U.S.*
National Instruments NI USB-6229 BNC DAQ	*National Instruments* *Austin, TX 78759, U.S.*
National Instruments GBIP-USB-HS GBIP USB Controller	*National Instruments* *Austin, TX 78759, U.S.*
pH-Meter CyberScan 500	*Eutech Instruments Europe* *3860 AGNijkerk, Netherlands*
pH-Meter Metrohm 780	*Deutsche Metrohm* *70794 Filderstadt, Germany*
VoltaLab PGZ100 Potentiostat	*Radiometer Analytical SAS* *69627 Villeurbanne, France*
Autolab PGSTAT128N Potentiostat	*Deutsche Metrohm* *70794 Filderstadt, Germany*
Leybold-Heraeus L560 evaporation system	*Oerlikon Leybold Vacuum* *50968 Cologne, Germany*
Mask-aligner MJB3	*Suss MicroTec* *85748 Garching, Germany*
100-E plasma etcher	*PVA TePla* *35435 Wettenberg, Germany*

Microscopy / AFM

Laser scanning microscope LSM 510	*Carl Zeiss AG* *73447 Oberkochen, Germany*
Light optical microscope Axiovert 40 C	*Carl Zeiss AG* *73447 Oberkochen, Germany*
Light optical microscope Axio Observer. Z1	*Carl Zeiss AG* *73447 Oberkochen, Germany*
Camera Exwave Had digital SSC-DC58AP	*Sony AG* *Tokyo, Japan*
Firewire camera Pixelink PL-A662	*Pixelink* *Ottawa, ON K1G 6C2, Canada*
Atomic Force Microscope NanoWizard I	*JPK Instruments AG* *12435 Berlin, Germany*
Cantilever NSC15/AlBS	*MicroMasch* *12618 Tallinn, Estonia*

X-ray irradiation

X-ray machine Stabilipan TR300f	*Siemens AG* *80333 München, Germany*
X-ray machine MG 320	*Philips Industrial x-rays* *22335 Hamburg, Germany*
Dose area product meter Diamentor M4	*PTW* *79115 Freiburg, Germany*
UNIDOS dosemeter	*PTW* *79115 Freiburg, Germany*
IQ4 electrometer	*PTW* *79115 Freiburg, Germany*
TM 786 ionization chamber	*PTW* *79115 Freiburg, Germany*
TM 23361 ionization chamber	*PTW* *79115 Freiburg, Germany*

Reagents

RPMI 1640 medium	*Biochrom AG* *12247 Berlin, Germany*
FBS Superior	*Biochrom AG* *12247 Berlin, Germany*

Penicillin/Streptomycin	*Biochrom AG* *12247 Berlin, Germany*
PBS – DULBECCO	*Biochrom AG* *12247 Berlin, Germany*
Trypsin (1:250) 0,25% (w/v) in PBS	*Biochrom AG* *12247 Berlin, Germany*
Trypsin/EDTA Solution 0,05%/0,02% in PBS	*Biochrom AG* *12247 Berlin, Germany*
Fibronectin, 0,1% Solution from Bovine Plasma	*Sigma-Aldrich Biochemie* *21147 Hamburg, Germany*
Hank's balanced salt solution 1X	*Biochrom AG* *12247 Berlin, Germany*
Calbiochem Glutaraldehyde 25% Aqueous Solution	*EMD Chemicals, Inc.* *Gibbstown, NJ 08027, U.S.*
Paraformaldehyde	*Sigma-Aldrich Biochemie* *21147 Hamburg, Germany*
Triton X-100	*Merck KGaA* *64293 Darmstadt, Germany*
Albumin from bovine serum, Cohn V fraction	*Sigma-Aldrich Biochemie* *21147 Hamburg, Germany*
Vectashield H-1000	*Vector Laboratories, Inc.* *Burlingame, CA 94010, U.S.*
70% Ethanol Sorte 642	*Kottkamp Alkoholvertrieb* *26123 Oldenburg, Germany*
Photoresist S1818	*Rohm and Haas* *Philadelphia PA, U.S.*
Developer Microposit 351	*Shipley Company* *Marlborough MA, U.S.*

Antibodies and Dyes

Anti-53BP1 (Rabbit Polyclnal)	*ABR-Affinity BioReagents* *Golden, CO 80403, U.S.*
Alexa Flour 488 goat anit-rabbit lgG (H+L)	*Invitrogen GmbH* *76131 Karlsruhe, Germany*
Hoechst 33342 trihydrochloride	*Invitrogen GmbH* *76131 Karlsruhe, Germany*
Rhodamine phalloidin	*Invitrogen GmbH* *76131 Karlsruhe, Germany*

Vybrant DiO cell labelling solution	*Invitrogen GmbH* *76131 Karlsruhe, Germany*

Software

LabView 8.6	*National Instruments* *Austin, TX 78759, U.S.*
Origin Pro 8	*OriginLab Corporation* *Northamton, MA01060, U.S.*
Zeiss LSM Image Browser 4.2.0.121	*Carl Zeiss Microimaging* *73447 Oberkochen, Germany*
NOVA Control software for Autolab	*Deutsche Metrohm* *70794 Filderstadt, Germany*
Volta Master 4 Control software for VoltaLab	*Radiometer Analytical SAS* *69627 Villeurbanne, France*
QCapture Pro 6.0	*QImaging* *Surrey BC, Canada V3S 6K3*
AxioVision	*Carl Zeiss Microimaging* *73447 Oberkochen, Germany*
SRIM-2011	*James F. Ziegler* *Annapolis MD, U.S.*

B. List of abbreviations

Abbreviations

2DEG	2-dimensional electron gas
AFM	Atomic force microscope
BESSY	Berliner Elektronenspeicherring-Gesellschaft für Synchrotronstrahlung
BSF	Backscatter factor
CE	Counter electrode
CT	Computer tomography
DAQ	Data acquisition system
DNA	Deoxyribonucleic acid
DSB	Double strand break
FET	Field-effect transistor
FWHM	Full width at half maximum
HEMT	High electron mobility transistor
IAEA	International Atomic Energy Agency
ICRP	International Commission on Radiological Protection
ICRU	International Commission on Radiation Units and Measurements
IDT	Interdigital transducer
ISFET	Ion sensitive field effect transistor
ISO	International Organization for Standardization
LP	Line pair
MBE	Molecular beam epitaxy
MOSFET	Metal oxide semiconductor field effect transistor
MOVPE	Metalorganic vapor phase epitaxy
NPLC	Number of power line cycles
PMT	Photo-multiplier tube
PTB	Physikalisch-Technische Bundesanstalt
KERMA	Kinetc energy released per unit mass
RE	Reference electrode
RIE	Reactive ion etch
ROI	Region of interest
SEM	Standard error of the mean
SNAKE	Superconducting nanoprobe for applied nuclear physics experiments
SRIM	Stopping and Range of Ions in Matter
StrlSchV	Strahlenschutzverordnung
TLD	Thermoluminescent Dosimeter
UV	Ultraviolet
WE	Work electrode
WHO	World Health Organization

Elements and compounds

Ag	Silver
AgCl	Silver chloride
Al	Aluminium
AlGaN	Aluminium gallium nitride
AlN	Aluminium nitride
Au	Gold
Cu	Copper
Fe	Iron
GaAs	Gallium arsenide
GaN	Gallium nitride
NaI	Sodium iodide
Pb	Lead
Pt	Platinum
SiC	Silicon carbide
Ti	Titanium
ZnS	Zinc sulfide

Chemical reagents

APS	Amino-propylsilane
APDEMS	Amino-propyldiethoxymethylsilane
BCl_3	Boron chloride
BSA	Bovine serum albumin
Cl_2	Chlorine
CO_2	Carbon dioxide
H_2O_2	Hydrogen peroxide
H_2SO_4	Sulfuric acid
HBSS	Hank`s balanced salt solution
HCl	Hydrochloric acid
HEPES	(4-(2-hydroxyethyl)-1-piperazineethanesulfonic acid
HCl	Sodium hydroxide
NaCl	Sodium chloride
NaOH	Sodium hydroxide
PBS	Phosphate buffered saline

C. SNAKE sample holder construction plans

Sample holder upper part

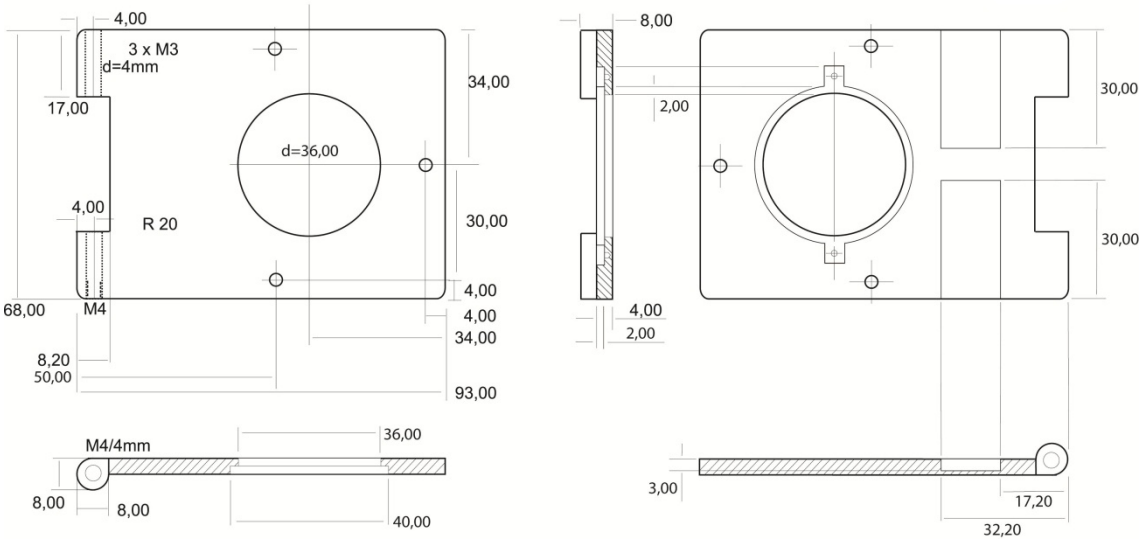

PVC inset (GaN/HEMT carrier)

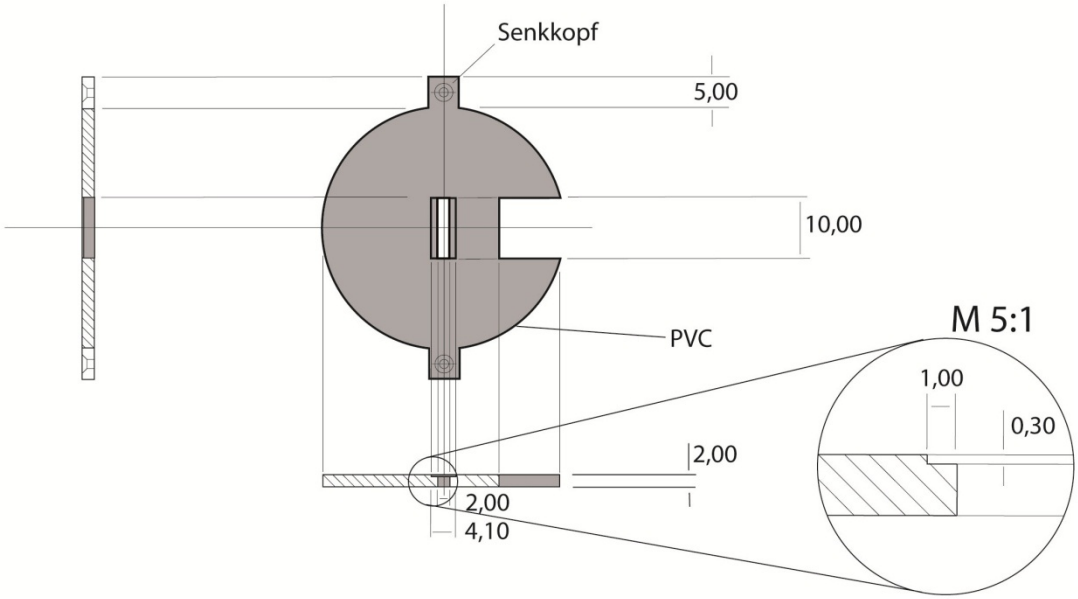

Sample holder lower part

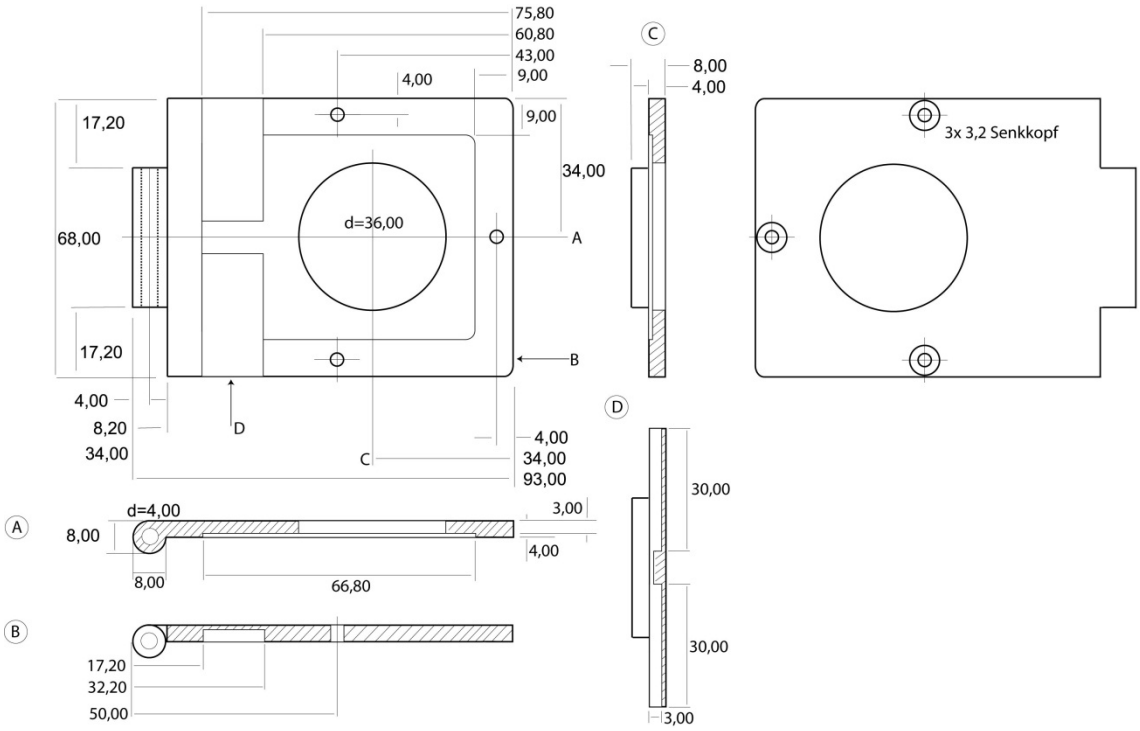

D. Measurement accuracy of Keithley 2400 SourceMeters

Summary of the measurement capabilities of a Keithley 2400 SourceMeter. The table gives all source and measurement ranges used in this work.

Mode	Range	Resolution	Accuracy ±(%rdg + ΔM)
Source	200 mV	5 µV	0.02% + 600 µV
Source	2 V	50 µV	0.02% + 600 µV
Source	20 V	500 µV	0.02% + 2.4 mV
Source	200 V	5 mV	0.02% + 24 mV
Measurement	1 µA	10 pA	0.029% + 300 pA
Measurement	10 µA	100 pA	0.027% + 700 pA
Measurement	100 µA	1 nA	0.025% + 6 nA
Measurement	1 mA	10 nA	0.027% + 60 nA

References

[Amb1999]
O. Ambacher, J. Smart, J. R. Shealy, N. G. Weimann, K. Chu, M. Murphy, W. J. Schaff, L. F. Eastman, R. Dimitrov, L. Wittmer, M. Stutzmann, W. Rieger, J. Hilsenbeck. Two-dimensional electon gases induced by spontaneous and piezoelectric polarization charges in N- and Ga-face AlGaN/GaN heterostructures. Journal of Applied Physics **85** (1999) 3222-3233

[Amb2000]
O. Ambacher, B. Foutz, J. Smart, J. R. Shealy, N. G. Weimann, K. Chu, M. Murphy, A. J. Sierakowski, W. J. Schaff, L. F. Eastman, L. F. Dimitrov, A. Mitchell, M. Stutzman. Two dimensional electron gases induced by spontaneous and piezoelectric polarization in undoped and doped AlGaN/GaN heterostructures. Journal of Applied Physics **87** (2000) 334-344

[And2001]
L. Anderson, C. Henderson, Y. Adachi. Phosphorylation and rapid relocalization of 53BP1 to nuclear foci upon DNA damage. Molecular and Cellular Biology **21** (2001) 1719–1729

[Asa2009]
A. Asaithamby, D. J. Chen. Cellular response to DNA double-strand-breaks after low-dose gamma-irradiation. Nucleic Acids Research **37** (2009) 3912-3923

[Ayl2004]
Y. Aylon, M. Kupiec. DSB repair: the yeast paradigm. DNA Repair **3** (2004) 797-815

[Bau2005]
B. Baur, G. Steinhoff, J. Hernando, O. Purrucker, M. Tanaka, B. Nickel, M. Stutzmann, M. Eickhoff. Chemical functionalization of GaN and AlN surfaces. Applied Physics Letters **87** (2005) 263901

[Bau2011]
B. A. K. Baur. Functionalization of group III-nitrides for biosensing applictions. Selected Topics of Semiconductor Physics and Technology, Vol. **128** (2011)

[Bed2007]
A. S. Beddar. Plastic scintillation dosimetry and its application to radiotherapy. Radiation Measurements **41** (2007) 124-133

[Bel1983]
E. Belau, R. Klanner, G. Lutz, E. Neugebauer, H. J. Seebrunner, A. Wylie, T. Böhringer, L. Hubbeling, P. Weilhammer, J. Kremmer, U. Kötz, M. Riebesell. Charge collection in silicon strip detectors. Nuclear Instruments and Methods in Physics Research **214** (1983) 253-260

[Ber1997]
F. Bernardini, V. Fiorentini, D. Vanderbilt. Spontaneous polarization and piezoelectric constants of III-V nitrides. Physical Review B **56** (1997) 10024-10027

[Ber2003]
G. Bertuccio, R. Casiraghi. Study of silicon carbide for x-ray detection and spectroscopy. IEEE Transactions on Nuclear Science **50** (2003) 175-185

[Ber2006]
D. Berdat, A. Marin, F. Herrera, M. A. M. Gijs. DNA biosensor using fluorescence microscopy and impedance spectroscopy. Sensors and Actuators B **118** (2006) 53-59

[Bet2010]
G. T. Betzel, S. P. Lansley, F. Baluti, L. Reinisch, J. Meyer. Operating parameters of CVD diamond detectors for radiation dosimetry. Nuclear Instruments and Methods A **614** (2010) 130-136

[BfS2010]
Bundesamt für Strahlenschutz. Umweltradioaktivität und Strahlenbelastung. Jahresbericht 2009 (2010)

[Boh2007]
C. F. Bohren, D. R. Huffman. References, in Absorption and Scattering of Light by Small Particles. Wiley-VCH Verlag GmbH, Weinheim, Germany (2007)

[Bor2010]
H. Bornefalk, M. Danielsson. Photon-counting spectral computed tomography using silicon strip detectors: a feasibility study. Physics in Medicine and Biology **55** (2010) 1999

[But2003]
M. J. Butson, P. K. N. Yu, T. Cheung , P. Metcalfe. Radiochromic film for medical radiation dosimetry. Materials Science and Engineering R **41** (2003) 61-120

[Cha2008]
V. Chakrapani, C. Pendyala, K. Kash, A. B. Anderson, M. K. Sunkara, J. C. Angus. Electrochemical Pinning of the Fermi Level: Mediation of Photoluminescence from Gallium Nitride and Zinc Oxide. Journal of the American Chemical Society **130** (2008) 12944–12952

[Cim2007]
I. Cimalla, F. Will, K. Tonisch, M. Niebelschütz, V. Cimalla, V. Lebedev, G. Kittler, M. Himmerlich, S. Krischok, J. A. Schaefer, M. Gebinoga, A. Schober, T. Friedrich, O. Ambacher. AlGaN/GaN biosensor—effect of device processing steps on the surface properties and biocompatibility. Sensors and Actuators B **123** (2007) 740–748

[Cla1962]
L. Clark, C. Lyons. Electrode Systems for Continuous Monitoring in Cardiovascular Surgery. Annals of the New York Academy of Sciences **102** (1962) 29-45

[Col1995]
A. R. Collins, M. Ai-guo, S. J. Duthie. The kinetics of repair of oxidative DNA damage (strand breaks and oxidised pyrimidines) in human cells. Mutatation Research **336** (1995) 69-77

[Deg1998]
C. Deger, E. Born, H. Angerer, O. Ambacher, M. Stutzmann, J. Hornsteiner, E. Riha, G. Fischerauer. Sound velocity of $Al_xGa_{1-x}N$ thin films obtained by surface acoustic-wave measurements. Applied Physics Letters **72** (1998) 2400

[Dim2000]
R. Dimitrov. Herstellung und Characterisierung von AlGaN/GaN-Transistoren. Selected Topics of Semiconductor Physics and Technology, Vol. **28** (2000)

[Dub2008]
J. Y. Duboz, M. Laügt, D. Schenk, B. Beaumont, J. L. Reverchon, A. D. Wieck, T. Zimmerling. GaN for x-ray detection. Applied Physics Letters **92** (2008) 263501

[Dub2009]
J. Y. Duboz, B. Beaumont, J. L. Reverchon, A. D. Wieck. Anomalous photoresponse of GaN x-ray Schottky detectors. Journal of Applied Physics **105** (2009) 114512

[Eas2002]
L. F. Eastman, V. Tilak, V. Kaper, J. Smart, R. Thompson, B. Green, J. R. Shealy, T. Prunty. Progress in High-Power, High Frequency AlGaN/GaN HEMTs. Physica Status Solidi (a) **194** (2002) 433-438

[Ehr2005]
C. Ehringfeld, S. Schmid, K. Poljanc, C. Kirisits, H. Aiginger, D. Georg. Application of commercial MOSFET detectors for in vivo dosimetry in the therapeutic x-ray range from 80 kV to 250 kV. Physics in Medicine and Biology **50** (2005) 289-303

[Est2008]
E. Estephan, C. Larroque, F. J. G. Cuisinier, Z. Bálint, C. Gergely. Tailoring GaN semiconductor surfaces with biomolecules. Journal of Physical Chemistry B **112** (2008) 8799–8805

[Fu2011]
K. Fu, G. Yu, C. Yao, G. Wang, M. Lu, G. Zhang. X-ray detectors based of Fe doped GaN photoconductors. Physica Status Solidi RRL **5** (2011) 187-189

[Gar1998]
J. A. Garrido, E. Monroy, I. Izpura, E. Muñoz. Photoconductive gain modeling of GaN photodetectors. Semiconductor Science and Technology **13** (1998) 563-568

[Gar2000]
J. A. Garrido, B. E. Foutz, J. A. Smart, J. R. Shealy, M. J. Murphy, W. J. Schaff, L. F. Eastman, E. Muñoz. Low-frequency noise and mobility fluctuations in AlGaN/GaN heterostructure field-effect transistors. Applied Physics Letters **76** (2000) 3442

[Gro1990]
B. Grosswendt. Dependence of the photon backscatter factor for water on source-to-phantom distance and irradiation field size. Physics in Medicine and Biology **35** (1990) 1233-1245

[Gue2000]
L. Guemouri, J. Ogier, Z. Zekhnini, J. J. Ramsden. The architecture of fibronectin at surfaces. Journal of Chemical Physics **113** (2000) 8183-8186

[Hen1993]
B. L. Henke, E. M. Gullikson, J. C. Davis. X-ray interactions: photoabsorption, scattering, transmission, and reflection at E=50-30000 eV, Z=1-92, Atomic Data and Nuclear Data Tables, Vol. **54** (1993) 181-342

[Hof2010]
M. Hofstetter, J. Howgate, I. D. Sharp, M. Funk, M. Stutzmann, H. G. Paretzke, S. Thalhammer. Real-time x-ray response of biocompatible solution gate AlGaN/GaN high electron mobility transistor devices. Applied Physics Letters **96** (2010) 092110

[Hof2011]
M. Hofstetter, J. Howgate, I. D. Sharp, M. Stutzmann, S. Thalhammer. Development and evaluation of gallium nitride-based thin films for x-ray dosimetry. Physics in Medicine and Biology **56** (2011) 3215-3231

[Hon2008]
S. K. Hong, H. K. Cho. Structural Defects in GaN and ZnO, in Oxide and Nitride Semiconductors: Processing, Properties and Applications. Springer Berlin Heidelberg, Germany (2008)

[How2010]
J. Howgate, S. J. Schoell, M. Hoeb, W. Steins, B. Baur, S. Hertrich, B. Nickel, I. D. Sharp, M. Stutzmann, M. Eickhoff. Photocatalytic cleavage of self-assembled organic monolayers by UV-induced charge transfer from GaN substrates. Advanced Materials **22** (2010) 2632-2636

[How2012]
J. D. Howgate, M. Hofstetter, S. J. Schoell, M. Schmid, S. Schäfer, I. Zizak, V. Hable, C. Greubel, G. Dollinger, S. Thalhammer, M. Stutzmann, I. D. Sharp. Ultrahigh gain AlGaN/GaN high energy radiation detectors. Physica Status Solidi (a); accepted (2012)

[Hub2004]
J. H. Hubbell, S. M. Seltzer. Tables of X-Ray Mass Attenuation Coefficients and Mass Energy-Absorption Coefficients from 1 keV to 20 MeV for Elements *Z* = 1 to 92 and 48 Additional Substances of Dosimetric Interest. NIST Standard Reference Database **126** [Online] http://physics.nist.gov/xaamdi (last update 2004)

[ICRU1989]
ICRU Report No. 44: Tissue Substitutes in Radiation Dosimetry and Measurement. International Comission on Radiation Units and Measurements (1989)

[ICRP1990]
ICRP Publication 60: Recommendations of the International Commission on Radiological Protection. Annals of the ICRP, Volume **21** (1990) 1-3

[Klo2007]
F. R. Kloss, M. Najam-Ul-Haq, M. Rainer, R. Gassner, G. Lepperdinger, C. W. Huck, G. Bonn, F. Klauser, X. Liu, N. Memmel, E. Bertel, J. A. Garrido, D. Steinmüller-Nethl. Nanocrystalline diamond - An excellent platform for life science applications. Journal of Nanoscience and Nanotechnology **7** (2007) 4581-4587

[Lau1996]
S. Lauxtermann, W. Bronner, J. Ludwig, K. Runge. Radiation detection using integrated GaAs HEMT electronics. Nuclear Instruments and Methods in Physics Research A **379** (1996) 247-251

[Ley2003]
L. B. Leybovich, A. Sethi, D. Nesrin. Comparison of ionization chambers of various volumes for IMRT absolute dose verification. Medical Physics **30** (2003) 119-23

[Lin2004]
A. Link. Zweidimensionale Elektronen- und Löchergase in GaN/AlGaN Heterostrukturen. Selected Topics of Semiconductor Physics and Technology, Vol. **66** (2004)

[Luo2001]
B. Luo, J. W. Johnson, F. Ren, K. K. Allums, C. R. Abernathy, S. J. Pearton, R. Dwivedi, T. N. Fogarty, R. Wilkins, A. M. Dabiran, A. M. Wowchack, C. J. Polley, P. P. Chow, A. G. Baca. dc and rf performance of proton-irradiated AlGaN/GaN high electron mobility transistors. Applied Physics Letters **79** (2001) 2196-2198

[Luo2002]
B. Luo, J. W. Johnson, F. Ren, K. K. Allums, C. R. Abernathy, S. J. Pearton, R. Dwivedi, T. N. Fogarty, R. Wilkins, A. M. Dabiran, A. M. Wowchack, C. J. Polley, P. P. Chow, A. G. Baca. High-energy proton irradiation effects on AlGaN/GaN High-Electron Mobility Transistors. Journal of Electronic Materials **31** (2002) 437-441

[Mah2011]
M. Mahmoodi, L. Ghazanfari. Fundamentals of biomedical applications of biomorphic SiC, in Properties and Applications of Silicon Carbide. InTech, Rijeka (2011) 297-344.

[Mun1997]
E. Muñoz, E. Monroy, J. A. Garrido, I. Izpura, F. J. Sánchez, M. A. Sánchez-García, E. Calleja, B. Beaumont, P. Gibart. Photoconductor gain mechanisms in GaN ultraviolet detectors. Applied Physics Letters **71** (1997) 870-872

[Mur1999]
M. J. Murphy, K. Chu, H. Wu, W. Yeo, W. J. Schaff, O. Ambacher, L. F. Eastman, T. J. Eustis, J. Silcox, R. Dimitrov, M. Stutzmann. High-frequency AlGaN/GaN polarization-induced high electron mobility transistors grown by plasma-assisted molecular-beam epitaxy. Applied Physics Letters **75** (1999) 3653-3655

[Neu2002]
R. Neuberger, G. Müller, M. Eickhoff, O. Ambacher, M. Stutzmann. Observation of ion-induced changes in the channel current of high electron mobility AlGaN/GaN transistors (HEMT). Materials Science and Engineering B **93** (2002) 143-146

[Neu2012]
T. Neumaier, J. Swenson, C. Pham, A. Polyzos, A. T. Lo, P. Yang, J. Dyball, A. Asaithamby, D. J. Chen, M. J. Bissel, S. Thalhammer, S. V. Costes. Evidence for formation of DNA repair centers and dose-response nonlinearity in human cells. Journal of the American Chemical Society **109** (20012) 443-448

[Pee1999]
D. J. Peet, M. D. Pryor. Evaluation of a MOSFET radiation sensor for the measurement of entrance surface dose in diagnostic radiology. British Journal of Radiology **72** (1999) 562-568

[Pod2006]
E. B. Podgoršak. Interactions of photons with matter, in Radiation Physics for Medical Physicists, Springer Berlin Heidelberg, Germany (2006)

[Pod2010]
A. Podolska, M. Kocan, A. M. Garces Cabezas, T. D. Wilson, G. A. Umana-Membreno, B. D. Nener, G. Parish, S. Keller, U. K. Mishra. Ion versus pH sensitivity of ungated AlGaN/GaN heterostructure-based devices. Applied Physics Letters **97** (2010) 012108

[Rei2000]
W. M. Reichert, A. A. Sharkawy. Handbook of Biomaterials Evaluation: Scientific, Technical, and Clinical Testing of Implant Materials. Vol. 28, Taylor and Francis, Philadelphia (2000)

[Ric1996]
R. G. Richards. The effect of surface roughness on fibroblast adhesion *in vitro*. Injury **23** (1996) 38-43

[Ros2006]
A. B. Rosenfeld, D. Cutajar, M. L. F. Lerch, G. Takacs, I. M. Cornelius, M. Yudelev, M. Zaider. Miniature semiconductor detctors for *in vivo* dosimetry. Radiation Protection Dosimetry **120** (2006) 48-55

[Rot2003]
K. Rothkamm, M. Löbrich. Evidence for a lack of DNA double-strand break repair in human cells exposed to very low x-ray doses. Proceedings of the National Academy of Sciences USA **100** (2003) 5057–5062

[Rön1898]
W. C. Röntgen. Über eine neue Art von Strahlen. Annalen der Physik, Volume **300** (1898) 1-11

[Rus2007]
R. K. Hobbie, B. J. Roth. Interaction of photons and charged particles with matter, in Intermediate Physics for Medicine and Biology, 4th edition. Springer New York (2007)

[Sch2008]
S. J. Schoell, M. Hoeb, I. D. Sharp, W. Steins, M. Eickhoff, M. Stutzmann, M. S. Brandt. Functionalization of 6H-SiC surfaces with organosilanes. Applied Physics Letters **92** (2008) 153301

[Sel2003]
P. J. Sellin. Recent advances in compound semiconductor radiation detectors. Nuclear Instruments and Methods in Physics Research A **513** (2003) 332-339

[Ste2003a]
G. Steinhoff, M. Hermann, W. J. Schaff, L. F. Eastman, M. Stutzmann, M. Eickhoff. pH response of GaN surfaces and its application for pH-sensitive field-effect transistors. Applied Physics Letters **83** (2003) 177-179

[Ste2003b]
G. Steinhoff, O. Purrucker, M. Tanaka, M. Stutzmann, M. Eickhoff. $Al_xGa_{1-x}N$-A New Material System for Biosensors. Advanced Functional Materials **13** (2003) 841-846

[Ste2005]
G. Steinhoff, B. Baur, G. Wrobel, S. Ingebrandt, A. Offenhäusser, A. Dadgar, A. Krost, M. Stutzmann, M. Eickhoff. Recording of cell action potentials with AlGaN/GaN field-effect transistors, Applied Physics Letters **86** (2005) 033901

[Ste2008]
G. Steinhoff. Group III-nitrides for bio- and electrochemical sensors. Selected Topics of Semiconductor Physics and Technology, Vol. **94** (2008)

[StrlSchV2011]
Strahlenschutzverordnung from 20th Juli 2001 (BGBl. I S. 1714; 2002 I S. 1459), with last change on 4th Oktober 2011 (BGBl. I S. 2000)

[Tsu1981]
K. Tsubouchi, K. Sugai, N. Mikoshiba. AlN Material Constants Evaluation and SAW Properties on AlN/Al2O3 and AlN/Si. IEEE Ultrasonics Symposium (1981) 375-380

[Vat1993]
S. Vatnitsky, H. Järvinen. Application of a natural diamond detector for the measurement of relative dose distributions in radiotherapy. Physics in Medicine and Biology **38** (1993) 173-184

[War1990]
J. F. Ward. The yield of DNA double-strand breaks produced intracellularly by ionizing radiation: A review. International Journal of Radiation Biology **57** (1990) 1141-1150

[Wri1997]
A. F. Wright. Elastic properties of zinc-blende and wurtzite AlN, GaN, and InN. Journal of Applied Physics **82** (1997) 2833

[Yu2007]
J. Yu, S. K. Jha, L. Xiao, Q. Liu, P. Wang, C. Surya, M. Yang. AlGaN/GaN heterostructures for non-invasive cell electrophysiological measurements. Biosensors and Bioelectronics **23** (2007) 513-519

[Zor2001]
A. Zoroddu, F. Bernardini, P. Ruggerone, V. Fiorentini. First-principles prediction of structure, energetics, formation enthalpy, elastic constants, polarization, and piezoelectric constants of AlN, GaN, and InN: Comparison of local and gradient-corrected density-functional theory. Physical Review B **64** (2001) 045208

List of Publications

Parts of this dissertation have been previously published in scientific journals.

Publications

Real-time x-ray response of biocompatible solution gate AlGaN/GaN high electron mobility transistor devices. M. Hofstetter, J. Howgate, I. D. Sharp, M. Funk, M. Stutzmann, H. G. Paretzke, S. Thalhammer. Applied Physics Letters **96** (2010) 092110

Semiconductor Biosensors. S. Thalhammer, M. Hofstetter, J. Howgate, M. Stutzmann. Patent Pub. No. WO/2010/142773, International Application No. PCT/EP2010/058183 (2010)

Development and evaluation of gallium nitride-based thin films for x-ray dosimetry. M. Hofstetter, J. Howgate, I. D. Sharp, M. Stutzmann, S. Thalhammer. Physics in Medicine and Biology **56** (2011) 3215-3231

Strahleneffekte: Dosimeter oder Biosensor? M. Hofstetter, J. Howgate, I. D. Sharp, M. Stutzmann, S. Thalhammer. Labor&more **4.11** (2011) 52-54

Ultrahigh gain AlGaN/GaN high energy radiation detectors. J. D. Howgate, M. Hofstetter, S. J. Schoell, M. Schmid2, S. Schäfer, I. Zizak, V. Hable, C. Greubel, G. Dollinger, S. Thalhammer, M. Stutzmann, I. D. Sharp. Physica Status Solidi A, doi: 10.1002/pssa.201228097

In-vitro bio-functionality of gallium nitride sensors for radiation biophysics. M. Hofstetter, J. Howgate, M. Schmid, S. Schoell, M. Sachsenhauser, D. Adigüzel, M. Stutzmann, I. D. Sharp, S. Thalhammer. Biochemical and Biophysical Research Communications **424** (2012) 348-353

Abstracts

Semiconductor based Biosensors and Lab-on-Chip systems: Applications in radiation biology. Bilateral Workshop on Nanoscale Systems (NIM and Global COE-University of Tokyo). M. Hofstetter, A.-L. Idzko, T. Neumaier, M. Stutzmann, A. Wixforth, G. Scarpa, D. Adigüzel, G. Lieckfeld, H. G. Paretzke, S. Thalhammer (Jul 2008)

Semiconductor based biosensors: Applications in radiation biology. Nanosystems and Sensors (NIM, CENS, SFB486). M. Hofstetter, M. Stutzmann, H. G. Paretzke, S. Thalhammer (Mar 2009)

Semiconductor based biosensors: Applications in radiation biology. European Biophysics Journal 38 (Suppl 1). M. Hofstetter, M. Stutzmann, H. G. Paretzke, S. Thalhammer (Jul 2009)

Real-time x-ray response of AlGaN/GaN-HEMT devices. Verhandl. DPG (IV) 45. M. Hofstetter, J. Howgate, I. D. Sharp, M. Stutzmann, H. G. Paretzke, S. Thalhammer (Mar 2010)

AlGaN/GaN semiconductor biosensors for applications in radiation biophysics. 4th annual Symposium on Nanobiotechnology. M. Hofstetter, J. Howgate, I. D. Sharp, M. Stutzmann, S. Thalhammer (Oct 2010)

AlGaN/GaN semiconductor biosensors for applications in radiation biophysics. Heinz Nixdorf Symposium: m3-microelectronic meets medicine. M. Hofstetter, J. Howgate, I. D. Sharp, M. Stutzmann, S. Thalhammer (Oct 2010)

Presentations

p.p. PD Dr. Guiseppe Scarpa, TUM, invited talk
Biocompatibility Studies of Solution-Processable Organic Thin-Film Transistors for Sensing Applications. IEEE International Conference on Nano/Molecular Medicine and Engineering, Tainan, Taiwan (Oct 2009)

Real-time x-ray response of AlGaN/GaN-HEMT devices. DPG Spring Meeting of the Condensed Matter Section, Regensburg, Germany (Mar 2010)

Real-time x-ray response of bio-compatible solution gate AlGaN/GaN high electron mobility transistor devices. NCRS Seminar, Munich, Germany (Apr 2010)

Development and evaluation of GaN based thin films for x-ray dosimetry. DRS Seminar, Munich, Germany (Jan 2012)

Acknowledgements

Sehr herzlich möchte ich mich bei meinem Betreuer und Doktorvater PD Dr. Stefan Thalhammer bedanken, der mich schon zur Durchführung der Diplomarbeit in seiner Arbeitsgruppe aufgenommen hat und seither jederzeit zur Seite stand. Es hat mich mit unzähligen Diskussionen, Ratschlägen und Denkanstößen die letzten Jahre begleitet und mir ermöglicht, dieses Thema in der vorliegenden Form zu bearbeiten und diese Arbeit fertig zu stellen. Vielen Dank dafür. Ich hoffe dass die die zukünftige Arbeit genau so viel Spaß macht wie bisher.

Prof. Wolfgang Brütting (Experimentalphyik IV, Universität Augsburg) danke ich für die Übernahme des Zweitgutachtens.

Ganz besonderer Dank gilt John Howgate, der mich während meiner Diplomarbeit nicht nur in die Labore des WSI eingewiesen, sondern auch in das Gebiet der Halbleiter eingeführt hat. Anschließend und während meiner gesamten Doktorarbeit wurde ich von ihm jederzeit bei Experimenten, Planung der Versuche, Diskussion der Ergebnisse und Veröffentlichungen tatkräftig unterstützt. In dieser Zeit ist hierbei eine äußerst ergebnisreiche Zusammenarbeit entstanden, die neben der Erzeugung unzähliger Messdaten außerdem äußerst viel Spaß gemacht hat.

Weiterhin möchte ich mich sehr herzlich bei Dr. Ian Sharp bedanken, der gestützt durch das NIM-Graduiertenprogramm ebenfalls die Betreuung meiner Arbeit übernommen hat. Obwohl er während meiner Doktorarbeit einen Forschungsauftrag in Berkeley übernahm, erhielt ich stets Rat und Unterstützung von ihm, gerade auf dem Gebiet der Halbleiter und der Planung der Experimente. Zudem möchte ich mich sehr für das Korrekturlesen dieser Arbeit bedanken.

Finanziell wurde diese Arbeit von der Nanosystems Initiative München (NIM) unterstützt. In diesem Zusammenhang möchte ich mich sehr bei Prof. Martin Stutzmann für die freundliche Zusammenarbeit innerhalb der NIM Kollaboration bedanken. Durch die Benutzung der Labore und Einrichtungen am Walter Schottky Institut wurde diese Arbeit erst möglich. Außerdem bedanke ich mich für die sorgfältigen Korrekturen der gemeinsamen Veröffentlichungen.

Prof. Günther Dollinger, Dr. Volker Hable, Christoph Greubel und Dr. Anna Friedl möchte ich für die überaus freundliche Zusammenarbeit am Tandembeschleuniger in Garching danken.

Für die Unterstützung und Zusammenarbeit am BESSY Elektronenspeicherring in Berlin bedanke ich mich bei Dr. Ivo Zizak.

Ebenfalls für die freundliche Zusammenarbeit möchte ich mich bei Christian Pioch und Prof. Werner Rühm bedanken. C. Pioch hat mit seinen Monte Carlo Simulationen in erheblichem Umfang zum Verständnis der Rückstreuungsexperimente in dieser Arbeit beigetragen. Vielen Dank dafür.

Vielen Dank an Norbert Menzel, Gerolf Lieckfeld und Helmut Niedermeier für die technische Unterstützung. Dies betrifft sowohl jegliche Hilfestellungen in den Werkstätten als auch die Einweisung in die Röntgenanlage am ISS.

Denis Adigüzel danke ich für die Unterstützung mit den Bestellungen sowie für die Hilfe mit den AFM Aufnahmen.

Weiterhin möchte ich den ganzen Diplom, Master- und Bachelorstudenten danken, die ihre Arbeit über die GaN-Halbleitersensoren in unserer Arbeitsgruppe durchgeführt haben. Viele der Ergebnisse, die sich in dieser Arbeit finden, sind mit ihrer Hilfe zustande gekommen. Zu den (inzwischen ehemaligen) Studenten zählen: Maren Funk, Terry Richard Heidmann, Robin Materlik, Sabine Konzack, Martin Schmid, Christian Huber und Andreas Albrecht.

Für die Hilfestellung bei der APS Oberflächenfunktionalisierung möchte ich meinen Dank Sebastian Schoell und Matthias Sachsenhausen vom WSI aussprechen.

Bei Dr. Matthias Greiter und Florian Wagner möchte ich mich in die Einführung des IAEA/WHO Dosimetrie Labors am Helmholtz Zentrum München sowie der weiteren Unterstützung dort bedanken.

Helmut Schlattl danke ich für die Berechnung der Röntgenspektren für die Stabilipan Röntgenanlage im Keller des ISS.

Ein herzliches Dankeschön auch an alle weiteren (und ehemaligen) Mitarbeiter der Arbeitsgruppe Strahlenbiophyik des ISS und der Arbeitsgruppe E25 des WSI die mich bei meiner Arbeit unterstützt haben. Dazu zählen: Anna-Lena Idzko, Wolfgang Heidenreich, Klaus Wittmaack, Elisangela Linares, Daria Grönlinger, Heike Schittl, Andreas Schmid, Susanne Schäfer und Claudia Paulus.

Ein ganz besonderer Dank gilt natürlich meiner Familie und meinen Freunden, allen voran meinem Vater, der mich all die Jahre nicht nur finanziell unterstützt hat. Außerdem möchte ich meiner Freundin Sabine für die Unterstützung danken.

Ich hoffe dass die zukünftige Arbeit genau so viel Spaß macht, wie die letzten Jahre.

Danke

Curriculum vitae

Markus Hofstetter

Geburtsdatum	14.10.1978
Geburtsort	Landshut
Nationalität	deutsch
Familienstand	ledig

Sep 1985 – Aug 1989	Grundschule Taufkirchen/Vils
Sep 1989 – Aug 1991	Gymnasium Dorfen
Sep 1991 – Aug 1996	Realschule Taufkirchen/Vils Abschluss: Mittlere Reife
Sep 1996 – Feb 2000	Ausbildung bei der Lufthansa Technik AG Abschluss: Industrieelekroniker
Feb 2000 – Apr 2000	Fluggeräteelekroniker bei der Lufthansa Technik AG
Mai 2000 – Mär 2001	Zivildienst bei Malteser Erding
Apr 2001 – Aug 2001	Fluggeräteelekroniker bei der Lufthansa Technik AG
Sep 2001 – Aug 2003	Berufsoberschule Landshut Abschluss: Fachgebundene Hochschulreife
Okt 2003 – Nov 2008	Technische Universität München Abschluss: Diplom-Physiker
Dez 2008 – Jul 2009	wiss. Mitarbeiter am Helmholtz Zentrum München
Aug 2009 – Jun 2012	Doktorarbeit an der Universität Augsburg Gastvertrag am Helmholtz Zentrum München